Calibrating Astronomical Spectrographs with Frequency Combs

Tobias Wilken

Dissertation
an der Fakultät der Physik
der Ludwig–Maximilians–Universität
München

vorgelegt von
Tobias Wilken
aus Bad Harzburg

München, den 10. 11. 2010

Zusammenfassung

Im Rahmen dieser Arbeit wurde ein Frequenzkamm entwickelt, um astronomische Spektrographen besser kalibrieren zu können.

Im Jahr 1999 hat die Entwicklung des Frequenzkamms den Bereich der Präzisionsspektroskopie revolutioniert. Mit seiner Hilfe wurde die Messung von Übergängen in atomaren Systemen mit zuvor unerreichter Genauigkeit möglich, was 2005 mit dem Nobelpreis für Theodor W. Hänsch und John Hall gewürdigt wurde.

In dieser Zeit wurde am 3.6 m Teleskop in La Silla, Chile der HARPS Spektrograph in Betrieb genommen. Er besitzt bis heute die höchste Sensitivität um die Beschleunigung kosmischer Objekte zu detektieren. Diese wird aus einer Änderung der Rotverschiebung des Lichts geschlossen. Die Präzision, mit der Frequenzänderungen gemessen werden können, ist momentan begrenzt durch die Kalibrationsquellen. Für die Entdeckung erdähnlicher Planeten über ihren Rückstoß oder gar die direkte Beobachtung der beschleunigten Ausdehnung unseres Universums ist diese Genauigkeit jedoch unzureichend. Nur durch den Einsatz neuartiger Kalibrationsquellen kann eine ausreichende Sensitivität auf Änderungen der Rotverschiebung erreicht werden.

Daher wurde in 2005 eine Zusammenarbeit zwischen der Europäischen Südsternwarte (ESO) und dem Max-Planck-Institut für Quantenoptik (MPQ) initiiert um einen Frequenzkamm zu entwickeln, der für die nächste Generation von Spektrographen als Kalibrationsquelle dienen kann. In dieser Arbeit wurde ein Yb-Faserlaser entworfen und erstmals zu einem Frequenzkamm inklusive Detektion und Stabilisierung der Offset-Frequenz weiterentwickelt. Um die einzelnen Kalibrationslinien des Kamms mit einem astronomischen Spektrographen auflösen zu können, musste der Modenabstand erhöht werden. Dazu wurden Fabry-Pérot Resonatoren als schmalbandige Filter entwickelt. Schließlich musste der spektrale Bereich des Spektrographen von $400-700$ nm abgedeckt werden, was durch spektrale Verbreiterung in speziell entwickelten, mikrostrukturierten Fasern erreicht wurde.

Mehrere Entwicklungsstufen dieses Systems wurden an einem Spektrographen auf Teneriffa und an HARPS getestet. Dabei konnte jeweils gezeigt werden, dass der Frequenzkamm die erwarteten Spezifikationen erfüllt und traditionelle Kalibrationsquellen in ihrer Sensitivität auf Frequenzabweichungen übertrifft. Frequenzänderungen von 200 kHz konnten detektiert werden, was einer Sensitivität auf Geschwindigkeitsänderungen von kosmischen Objekten von 10 cm/s entspricht. Ca. 30% des spektralen Bereiches des HARPS Spektrometers konnten abgedeckt werden und mit verbesserter spektraler Verbreiterung ist das Erreichen des gesamten Bereichs mit der nächsten Entwicklungsstufe realistisch.

Durch den Einsatz eines solchen, verbreiterten Frequenzkamms an Spektrographen der nächsten Generation werden Geschwindigkeitsänderungen eines kosmischen Objekts von nur 1 cm/s detektierbar. Dies wird die Durchführung der ambitionierten Beobachtugen ermöglichen, die in der Astronomie innerhalb der nächsten Jahrzehnte geplant sind.

Abstract

This thesis reports on the development of a frequency comb to improve the calibration of astronomical spectrographs.

In 1999, the invention of the frequency comb initiated a revolution in the field of precision spectroscopy. It enabled measurement of transitions in atomic and molecular systems with unprecedented accuracy, and in recognition of this achievement, the Nobel Prize was later awarded to T. W. Hänsch and John Hall in 2005.

During this time the HARPS spectrograph was commissioned for the 3.6 m telescope in La Silla, Chile. Today, it still has the highest sensitivity for detecting the acceleration of cosmic objects, which is determined from the light's change in redshift. Currently, the precision with which frequency shifts can be determined is limited by the calibration sources. This level of precision is insufficient for detecting extrasolar planets via their recoil or the direct observation of the acceleration of the universe's expansion, however. Hence, new types of calibration sources are needed to enable measurements with an increased sensitivity to redshift variations.

To address this need, a cooperation between the European Southern Observatory (ESO) and the Max-Planck-Institute of Quantum Optics (MPQ) was initiated in 2005 to develop a frequency comb as a calibration source of next generation spectrographs. In this work, a new frequency comb system based on a Yb-fiber laser has been developed. The spacing of the comb modes has to be increased for astronomical spectrographs to be able to separate them. Thus, Fabry-Pérot cavities were designed to act as a narrow-band filter. Moreover, the comb's spectral bandwidth has to encompass the range of $400 - 700$ nm. This was achieved by spectral broadening in specially designed microstructured fibers.

Several versions of the system have been tested at a spectrograph on Tenerife and at HARPS. These tests were able to demonstrate that the comb performs as expected and exceeds the traditional calibration sources in their sensitivity to frequency variations. A frequency shift of only 200 kHz could be detected, which corresponds to a 10 cm/s sensitivity to changes of the velocity of a cosmic object. About 30% of HARPS' spectral bandwidth could be covered, which gives rise to optimism that it will soon be possible to cover the entire spectral range by improving the spectral broadening.

Employing such a broadened frequency comb at a next generation spectrograph will allow for the detection of a variation of a cosmic object's velocity of only 1 cm/s. This will enable the ambitious observations that astronomers envision to be possible within the next decades.

Contents

Chapter 1

Introduction

Did the universe have a beginning and will it have an end? Is our Earth unique? Are we alone in the universe? Questions like these have fascinated mankind ever since we tilted our heads to gaze at a clear night sky. Philosphers tended to have two schools of thought: "There cannot be more worlds than one" (Aristotle, 384 - 322 BC) or "there are infinite worlds both like and unlike this world of ours" (Epicurus, 341 - 270 BC). Only by methodical observations of the other planets in our solar system could an empirically founded answer be given. These observations led to the evolution from philosophy to modern science. The first steps in this direction were made in the 15th century by Copernicus, "who stopped the Sun and moved the Earth" [1] by proposing a heliocentric cosmos. A few decades later, Galilei used one of the first telescopes to accurately measure the movements of celestial objects, which, among other discoveries, made him indisputably one of the fathers of modern science.

Today, after a breath taking development of physics and astronomy, our knowledge about the universe and its content is enormous, but some of the most fundamental questions are still open for debate. Over time, the Sun has been put in a outer arm of the Milky Way, which is now called a galaxy, and known to contain several hundred billion stars both alike and unlike our Sun. Our galaxy is only one of billions in the observable universe, which probably is again only part of the whole thing, as during an inflation period in the early universe, most of its content vanished behind an event horizon. A background radiation of about $2\,\mathrm{mm}$ wavelength, with a black-body spectrum corresponding to a temperature of about $3\,\mathrm{K}$, permeates the universe and is the earliest signature of the observable history of the universe.

In 1929, Hubble found that most of the distant galaxies are redshifted with a linear dependency on the distance [2], i.e. they are moving away from us and the farther they are, the faster they are moving. As a consequence, at some time in the past, all matter was concentrated at one point, from which the universe started. This event is called the Big Bang and answers the question about the beginning of the universe.

The fate of the universe, however, remains an unsolved mystery. Until Hubble made his discovery, common belief was that the universe is stable and its size unchanging. Einstein even introduced an artificial parameter, the cosmological constant, in his theory of general relativity to save this assumption [3]. Later, he revoked that constant as "his biggest blunder", since an expanding universe is in no need of a force acting as negative gravity to compensate the positive gravity of matter.

Further observations and theoretical calculations eventually lead to the conclusion that this condemnation might have been too early. In the 1990s, independent observations of type Ia supernovae [4, 5], the cosmic microwave background [6] and the large scale galaxy distribution [7] supported the re-introduction of the cosmological constant with a total energy Ω_Λ twice that of all normal matter. The nature of the cosmological constant, however, remains a complete mystery. It has a repulsive effect and accounts for two thirds of the energy density in the universe, which leads to the conclusion that it must be distributed extremely smoothly as there is no observable effect on gravitationally bound objects like galaxy clusters.

Quantum vacuum was proposed as an explanation. The virtual pairs of particles that make up quantum vacuum have a negative pressure and hence are very repulsive. If they also had a non-zero energy density, this would exactly have the desired effect. Unfortunately, the attempt to predict the energy density of quantum vacuum is disenchanting. The smallest estimates are a factor of 10^{55} too large, so theorists believe that there is probably an underlying symmetry, leading to an exact cancellation of the vacuum energy. A different explanation for this "dark energy" is in urgent need.

Assuming that $\Omega_\Lambda = 0.72$ and the validity of general relativity leads to the prediction of a presently accelerating expansion of the universe. Directly monitoring the change in redshift of distant cosmic objects would then provide a model independent measure of the expansion history of the universe. This measurement was already proposed in the 1950s [8] (when the expansion was still assumed to decelerate): "However, for the test to be useful, it would seem that a precision redshift catalog must be stored away for the order of 10^7 years before an answer can be found because the decelerations are so small by terrestrial standards." At that time, measuring redshift changes on the order of $10\,\mathrm{km/s}$ (see section 2.1 for nomenclature) was conceivable. In this work, a tool for the calibration of spectrographs on the cm/s-scale is presented, which shall enable the direct detection of an accelerating expansion of the universe within a decade using next generation telescopes.

With these telescopes, the question for the uniqueness of Earth can safely be answered too, by detecting an Earth-like planet orbiting a Sun-like star. For as long as stars have been understood as distant suns, the idea of extra-solar planets (or exoplanets) harboring extraterrestrial life has been discussed. Detecting an exoplanet, however, is far from easy, since by definition it is emitting no light from thermonuclear fusion [9] but instead reflecting only a tiny amount of its host star's light. The back-action of a planet on the star, be it on its position, velocity, light

curve or other property, is also only very small. Due to this difficulty, proof of the existence of exoplanets was not found until the 1990s [10, 11].

Various methods have been developed and successfully applied to find new exoplanets [12] and recently, using adaptive optics it even became possible to directly observe planets in orbit around various stars [13]. Still, with all these methods, it is currently not possible to detect a twin to the Earth. The most successful method to find exoplanets, is measuring the planet's impact on the star's motion via an induced Doppler shift [14]. With this technique, planets that impress a Doppler shift of only 70 cm/s onto their host stars [16] can be safely detected. In comparison, the Earth induces a shift of only 9 cm/s onto our Sun over a period of one year. A spectrograph with a sensitivity and calibration on the cm/s-level should thus be capable of finally proving the existence of extra-solar Earth-like planets.

Once a planet is detected which in principle supports the development of life, the question whether these planets are inhabited and, if so, by intelligent life, would certainly be the next to tackle. Under which circumstances a planet can support life and how we could possibly detect signs of it has already been and continues to be vividly discussed [17]. These observations will take place in an even farther future, but this work will make them less fictitious and hypothetical than they have been thus far.

Naturally, astronomy always benefited from the cutting-edge technologies of optics or even lead to their development. Galilei pointed his telescope at the sky only one year after its invention, Fraunhofer used his spectroscope to observe the Sun, and nowadays the invention of adaptive optics [18] and the application of lasers as guide stars [19] helped to overcome atmospheric distortions, which until then were limiting ground based angular resolution.

When astronomers realized that the state-of-the-art spectrographs were limited by their calibration source [20], they had to look for a completely new technique. In 2005, the European Southern Observatory (ESO) and the Max-Planck-Institute of Quantum Optics (MPQ) established a cooperation to investigate the possibility of using a specifically designed frequency comb to calibrate next generation spectrographs. First, a theoretical study was performed to prove the potential of frequency combs [21]. Since 2007 efforts have been ongoing to construct a comb that fulfills the requirements to calibrate an astronomical spectrograph.

A frequency comb is a light source, emitting many narrow lines, whose frequency differences lie in the radio frequency domain and are exactly equal throughout its whole, comb-like spectrum. Such a device is extremely helpful in laser spectroscopy, as it facilitates mapping the optical frequencies (oscillating at several hundred THz) to the radio frequency domain via the detection of heterodyne beatnotes.

This principle was already realized in the late 1970s, when a picosecond laser was used to bridge a frequency gap of several GHz in the optical regime to measure some fine and hyperfine splitting in atomic sodium [22]. Nonetheless, the full

impact of this idea was not accessible until in the 1990s during which the Kerr-lens mode-locked titanium-sapphire (Ti:Sa) [23] laser was developed and highly nonlinear, microstructured fibers were invented [24]. The interplay of these two enabled the construction of a femtosecond laser with an octave-spanning spectrum which facilitated the detection of the zero-point frequency offset of the comb-like spectrum. By referencing this offset and the mode spacing (which is the repetition rate of the pulses) to a local oscillator (e.g. an atomic clock), every single mode of the spectrum becomes fixed in its phase and frequency. The result is a laser that delivers about one million frequency markers throughout its spectrum, each of them possessing the long-term stability and accuracy of the reference.

The development of the first frequency comb was mainly a head-to-head race between the group of T. W. Hänsch at MPQ and J. L. Hall at the National Institute of Standards and Technology that culminated in both being awarded with the Nobel Prize in 2005. The interesting and partially thrilling history can be read in the book edited by Ye and Cundiff [25]. Soon after the first demonstration [26, 27], the first precision frequency measurements on various atomic systems were performed (e.g. in hydrogen [28], ytterbium [29], mercury [30] or calcium [30, 31]), each improving the previous accuracy by more than one or two orders of magnitude.

Today, a variety of fields apart from laser spectroscopy benefit from the invention of the frequency comb. The most prominent examples are the development of atomic clocks, based on optical transitions [32, 33], the generation and control of attosecond pulses [34], the generation of ultra-low noise microwave frequencies [35], absolute length measurements [36], the generation of high harmonics and extreme ultra-violet light [37], the dissemination of frequency standards [38], timing applications [39], ultra-fast asynchronous optical sampling [40], direct frequency comb spectroscopy [41], ultra-fast Fourier transform spectroscopy [42] and starting with this work also the high-accuracy calibration of spectrographs, in particular for astronomical applications [44, 45].

During this work, a frequency comb system was built to meet the requirements for calibrating astronomical spectrographs. The main challenge is to cover the desired spectral range of ~ 400 to $700\,\mathrm{nm}$ with a mode spacing of $\sim 15\,\mathrm{GHz}$. Such a high mode spacing is needed, since spectrographs, designed for highest sensitivity to variations in the radial velocity of a cosmic object, typically have a resolution of $\sim 5\,\mathrm{GHz}$. Since there is no suitable frequency comb generator operating at above $10\,\mathrm{GHz}$, Fabry-Pérot cavities are used to increase the mode separation.

A femtosecond fiber oscillator was chosen to be the generator of the frequency comb, as fiber lasers are proven to run reliably over many years without maintenance. Permanent operability at a telescope is an additional but critical requirement for a spectrograph calibrator. Ytterbium-doped fibers are the preferred gain material because they have two advantages over other dopants. First, the central emission wavelength of $1030\,\mathrm{nm}$, when frequency doubled to $515\,\mathrm{nm}$, fits nicely (in frequency)

with the center of the desired wavelength range. Second, and more important, signal amplification to high average powers is relatively easy with Yb-doped fibers, due to their high gain and especially low quantum defect between pump and signal wavelength which leads a high efficiency.

At the beginning of this work, a frequency comb based on a Yb-fiber laser had never been demonstrated before, and the whole system had to be developed from scratch. First, an oscillator has been built and characterized [43] and subsequently a f-$2f$ interferometer for the detection and stabilization of the offset frequency. Afterwards, developing suitable fiber amplifiers for high output powers combined with a large bandwidth has been a major effort. In parallel, Fabry-Pérot cavities for increasing the mode spacing have been investigated. A pulse compressor needed to be developed to achieve minimum pulse widths for maximum conversion efficiency in the second harmonic stage after the filter cavities. Finally, highly nonlinear fibers have been tested to obtain spectral broadening at the full mode separation. The latest result is a frequency comb with 14-18 GHz mode separation, a central wavelength of 532 nm and a spectral width of more than 100 nm (at 20 dB below peak).

During the period of this work, the system could be tested three times at a real astronomical spectrograph. The first time in 2008, a proof-of-principle experiment was carried out at the Vacuum Tower Telescope (VTT) on Tenerife with a commercial erbium-fiber laser and a single filter stage [44]. In 2009 and 2010 the frequency doubled Yb-fiber comb was tested at the High Accuracy Radial velocity Planet Searcher (HARPS) at La Silla observatory in Chile [45]. A repeatability of the calibration of 10 cm/s could be demonstrated, by using little more than one out of 72 echelle orders of the spectrograph [46]. This outperforms the capabilities of the previously used calibration with spectral lamps, which need to average over all available orders to achieve a repeatability of ~ 20 cm/s. Irregularities in the pixel-to-frequency map have been detected and accounted for in the absolute frequency calibration for the first time, leading to an absolute calibration uncertainty of only 2.4 m/s. With a fine sampling of this calibration curve, intrapixel variations can be characterized and locally, an absolute frequency uncertainty of about 1.0 m/s is achieved.

Besides me, several other people have been or are still actively working on the "Astrocomb" project. Diana Höfling helped build and characterize the first Yb-fiber oscillators and amplifiers [43]. Since 2007, Tilo Steinmetz has been working as a post-doc on the project and is mainly occupied with the Fabry-Pérot cavities. Phillip Vilar-Welter worked on increasing the repetition rate of the oscillators to > 500 GHz [47]. During 2010, Simon Herr has been testing harmonically mode-locked oscillators as a comb generator in his diploma thesis [48]. Rafael Probst started in 2010 as a new PhD-student on the project.

1.1   A guide through this work

A reasonable assumption about the readership of this work is that they can be classified into readers with either an astronomical or a quantum optical background or neither. For those, who are not using it to look up some specific detail, a guide is given on how this work might be approached.

A less knowledgeable reader can go through this work from start to finish, following the logical course without encountering unexplained facts or techniques. It will, however, keep him in suspense, as the interesting results are presented towards the end. A more result-oriented approach would be to start with chapter 5, in which the central topic "calibration of high precision astronomical spectrographs" is presented. Cross-references to chapter 2 (where the frequency comb's suitability as a calibration source is motivated) and chapter 3 (where the technical details of the comb are presented) are given therein. Chapter 4 can be read to find out about the first milestone, achieved in this project, a proof-of-principle calibration test at a solar spectrograph. Those who are interested in the ideas people in the past had of the future are welcome to read the outlook given in chapter 6.

Chapter 2

High precision spectroscopy in astronomy

2.1 Basic concepts

Before presenting the exciting projects in astronomy, that serve as the motivation for this work, a short introduction to important concepts within the frame of calibrating astronomical spectrographs will be given.

Radial velocity In many areas of astronomical spectroscopy, the velocity of a cosmic object or its change are the quantity of interest. It can be deduced from the observed redshift of the detected light. On Earth, the frequency f_{obs} of an observed spectral feature can be measured and compared with its natural frequency f_0, measured in a frame of reference at rest. The redshift is then defined as

$$z = \frac{f_0 - f_{obs}}{f_{obs}}. \tag{2.1}$$

If the object has a peculiar motion relative to the Earth, the component in the direction of the line of sight is its radial velocity v. For objects with non-relativistic velocities — an appropriate assumption for stars within our galaxy — the redshift is the first order Doppler shift $z = v/c$. In the case that the redshift derives from the expansion of the universe and thus of space itself, the relation is $z = (1/a(t) - 1)$, with $a(t)$ being the scale factor of the universe (see section 2.2.3).

The change of an object's frequency shift is best given in units of the radial velocity, since this is independent of the emission frequency of the spectral feature. At a wavelength of $500\,\mathrm{nm}$ ($f = 600\,\mathrm{THz}$), a change in radial velocity of $\delta v = 1\,\mathrm{m/s}$ corresponds to

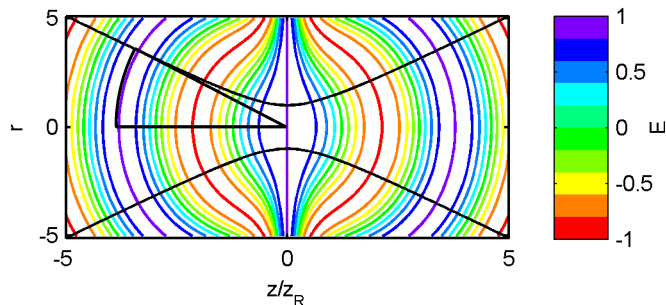$$\delta f = \frac{f}{c}\,\delta v \approx 2\mathrm{MHz}. \tag{2.2}$$

Figure 2.1: *Phase fronts (colored) and $1/e$-radius (black) of the electric field $E(r,z)$ of a Gaussian beam with a Rayleigh length z_R two times the inverse wave number. The segment of the circle illustrates that the distance between two wave fronts — and thus the wavelength — is different on axis and for example along the $1/e$-radius.*

In this work, a frequency shift is given in the unit, that fits the context best. When dealing with mode spacings or detunings these are given in units of [Hz], while calibration related properties such as repeatability or accuracy are given in [m/s].

Wavelength versus frequency In optics, it is commonly assumed that the wavelength λ and frequency f of light are uniquely coupled via the (frequency-dependent) speed of light c. When defining the wavelength as the distance between two consecutive phase fronts along the propagation direction of the wave, however, the simple relation $c \equiv \lambda f$ is only true for special waveforms such as a plane wave or a spherical wave. For general waveforms, this equality is not fulfilled at all positions in space, i.e.

$$\lambda \not\equiv \frac{c}{f}. \tag{2.3}$$

Already for Gaussian beams the relation between frequency and wavelength is dependent on the position, as depicted in figure 2.1.

The frequency of light is well-defined via the photon energy and will not change as long as nonlinear processes can be avoided. The wavelength, however, will be changed by any traversed component due to wavefront distortions. Now, a spectrograph is a device that compares the wavelength of light with its own characteristic length scale, the groove density. If the wavelengths of two light sources (e.g. starlight and calibration light) are to be compared via the spectrograph, both waveforms must coincide or else the respective diffraction pattern will differ, which leads to a measurement error. While this effect can be neglected in most applications, in this work, sensitivity to relative variations of less than 10^{-10} is aimed for. In this case, wave front distortions become relevant and can have a measurable effect as shown in section 5.4.
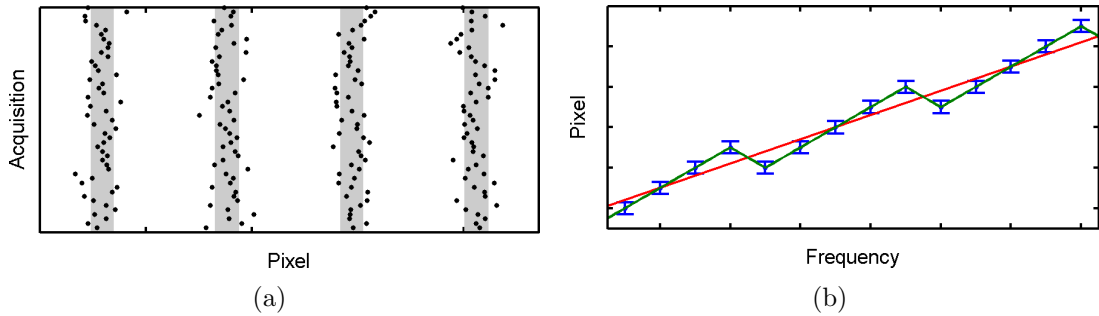
Figure 2.2: *Quantitative characteristics of a spectrograph calibration. (a) The standard deviation (shaded area) of subsequent measurements of the same calibration line determines the calibration repeatability. (b) The deviation of a model (red) of the frequency-to-pixel distribution from the measured positions (blue) determines the calibration's absolute frequency accuracy. Not only must the repeatability of the calibration be high to deduce an accurate model but the model must also be suitable and the sampling sufficiently high. Otherwise, one might have a model that fits the data well (green) but might still be inaccurate at the discontinuities.*

Repeatability and absolute frequency calibration The quality of the calibration of a spectrograph is characterized quantitatively by two parameters: its repeatability and the accuracy of the derived calibration curve. Both concepts are illustrated in figure 2.2.

The repeatability is defined as the "closeness of the agreement between the results of successive measurements of the same measurand carried out under the same conditions of measurement" [49]. It is quantified by the standard deviation of successive measurements of the same calibration line with the spectrograph. The repeatability of the calibration determines the limiting uncertainty for measuring radial velocity variations of cosmic objects. Essential in the definition of repeatability are *the same conditions of measurement*, which include using the same spectrograph at the same ambient conditions and an invariant calibration source. The absolute frequencies of the calibration lines might even be unknown as long as they don't change with time. Long-term drifts of the instrument are of no importance, since they can be tracked by repeated calibration. Short-term drifts between subsequent acquisitions, however, would decrease the instrument's sensitivity to accelerations of the cosmic object and must be excluded.

With long observation periods spanning several decades, however, it becomes increasingly important to also have an absolute frequency calibration to enable the comparison of data from different telescopes and/or spectrographs. To determine the absolute frequency of an unknown line with the spectrograph, a mapping between line frequencies and their measured position on the CCD must be established, the so-called calibration curve. The uncertainty of the calibration curve and thus of the absolute frequency measurement is given by its deviation from the true cal-

ibration curve. The latter can be probed when knowing the exact frequency of a calibration line and measuring its position on the CCD. To obtain a high accuracy, the calibration lines' frequencies must therefore have a low uncertainty. In addition, it is necessary to choose an appropriate model for the calibration curve and to have a sufficiently dense sampling so that essential features are not missed.

2.2   Science cases

2.2.1   Temporal variation of fundamental constants

The Standard Model of particle physics knows 28 fundamental constants: The coupling constants of the four fundamental interactions, the masses of two bosonic particles (the W-boson and the hypothetical "Higgs"-boson), and 22 fermionic fundamental particles (three leptons, three neutrinos, six quarks, four parameters for quark-flavor mixing and six for lepton-flavor mixing) [50]. There have been many attempts to predict the values of these constants but so far each of them has failed. Existing theories cannot be used to calculate these constants; instead, experiments must be carried out to determine them.

Up to now, there is also no understanding why these constants are indeed invariant over time. The Standard Model does not exclude this possibility, and generalized theories, as e.g. the theory of superstrings [51, 52], even predict temporal variations. In particular, the fine structure constant α, the scale factor Λ_c of quantum chromodynamics (QCD) and the coupling constant g_w of the weak interaction would be prone to variability [50]. If a variation of one of those fundamental constants could be measured, new laws of physics that predict these variations could be tested. This could eventually pave the way towards a unified theory, combining gravity with the Standard Model.

The idea of time-dependent fundamental constants is not new. Already in 1937, Dirac postulated his "large number hypothesis", [53] in which the fact that α is a small, dimensionless number led him to the idea that various fundamental parameters might scale with the age of the universe, and thus their ratio would be a small number too. In particular, he proposed that the ratio of the electric to the gravitational force between electron and proton is proportional to the age of the universe, which would result in a temporally decreasing constant of gravity with $\dot{G}/G \approx 10^{-10}/yr$. Since then, such a large shift of G has been ruled out by observations [54].

Recently, the fine structure constant $\alpha = e^2/\hbar c$, which determines the strength of the electromagnetic interaction, has become a major quantity of interest regarding its potential temporal variation. Already in the 1950s, astronomers looked for a potentially different fine-structure constant in distant galaxies [55, 56], but to no avail. In 1999, observations with the HIRES spectrograph at the Keck observatory were published, which indicated that α indeed had a different value in the early

epoch of the universe [57]. Additional observations and refined analysis, covering a window of $\sim 23\%$ to 87% of the age of the universe led to the conclusion, that at the time the light was absorbed by intergalactic dust ($\sim 10^{10}$ years ago), α was smaller than today by roughly $\frac{\Delta\alpha}{\alpha} \approx (-6 \pm 2) \times 10^{-6}$. Assuming a linear drift of α, these astronomical observations would imply a change of a few parts in 10^{-16} per year.

An interesting coincidence is that just as the first hint towards a temporally varying fine structure constant being observed, the first frequency comb was realized. Soon thereafter, laboratory measurements could be performed to test for a variation of α on the 10^{-15}-level over a few-year time scale [58, 59, 60]. To date, the lowest limit on a drift of α over short time scales is determined by a comparison between two optical atomic clocks, performed at the National Institute of Standards and Technology [61]. This limit is consistent with zero:

$$\frac{\dot{\alpha}}{\alpha} = (-1.6 \pm 2.3) \times 10^{-17}/\text{yr}. \qquad (2.4)$$

It is, however, not necessary that the assumption of a linear variation is fulfilled over cosmological time scales and models have been proposed, leading e.g. to a damped, oscillatory behavior of α [62].

A good overview of methods on how to extract a variation of fundamental constants from astronomical observations is given by Kanekar [63]. Their basic concept is quite simple. Different electronic transitions in atoms or molecules originate from different physical mechanisms, and their scaling laws depend on the fundamental constants in a different way. The fine-structure doublet, for example, scales with α, while comparing rotational with vibrational transitions in molecules is sensitive to the electron-to-proton mass ratio μ [64]. The ratio of the line frequencies, originating from two different mechanisms, as observed with the telescope is compared with laboratory measurements on Earth. This will measure the difference between the fundamental constants here and now and those at the time and location where the lines were generated. A suitable source of these lines are clouds of intergalactic dust in the line of sight of distant quasars [65]. The quasars serve as a white light source, illuminating the dust clouds that impress absorption lines onto the spectrum. Absorption lines of (cold) clouds have advantages over emission lines from (hot) stars or galaxies as they are typically much narrower and have a good signal-to-noise ratio at large distances. Furthermore, several clouds can make different and separable contributions to the spectrum of one quasar. Although it will not be discussed further in this work I spent part of my time at the MPQ working on frequency combs for different experiments in the laser spectroscopy group. One result obtained during this time was an improved laboratory value for one of these transitions, namely the 3s-3p doublet in $^{24}\text{Mg}^+$ and $^{26}\text{Mg}^+$ [66].

The alkali doublet method [67] uses exactly the comparison between two lines, with the fractional separation of the doublet wavelengths being proportional to α^2. An improved version is the many-multiplet method [68], which not only compares

two lines with each other but also averages over many transitions in different atomic species. The sensitivity to changes of $\Delta\alpha/\alpha$ is improved by an order of magnitude over the alkali doublet method, but comes at the price of higher susceptibility to systematic errors [63]. Both methods require the determination of large frequency differences with high accuracy. This is an example, where an absolute frequency calibration of cosmic signals with a high accuracy is mandatory. To achieve an uncertainty in $\Delta\alpha/\alpha$ of 1×10^{-7}, an absolute calibration of better than $5\,\mathrm{MHz}$ is necessary [69].

The present results are not undisputed due to unclear systematic uncertainties and contradicting findings have been published on whether there is a significant detectable change of α or not [70, 71, 72]. The debate is still ongoing and observations with a better resolution are imperative to definitively answer this question. Next generation spectrographs will be needed to perform this task [73] in order to have sufficient light-collecting power to observe a larger number of quasars. The absolute frequency calibration of the spectrograph should be on the m/s-level or better to allow for a high significance of the results.

2.2.2   Detection of extra-solar planets

The first planet outside our own solar system was detected in 1992 [10]. It exists, however, in a somewhat exotic environment, since the host star around which it is orbiting is a pulsar, i.e. the remnant of a supernova. Its formation process and ambient conditions are in no way comparable to our solar system. Soon thereafter, the first extrasolar planet (or exoplanet) was found around a main sequence star, namely 51 Pegasi [11]. This was the start of a very successful hunt, leading to more than 450 detected planets as of summer 2010 [74].

The vast majority of these planets was found with the radial velocity method (see fig. 2.3). A planet orbiting a star will induce a wobbling motion of the star around their common center of gravity. Within our frame of reference, the frequency of the light emitted by the star is thus modulated due to the Doppler effect. The period of the modulation is given by the planet's orbital period P, and the modulation depth is dependent on the mass ratio of star and planet $M_P/M_\star$. Additionally, if the inclination i of the orbital plane with respect to the line of sight is smaller than $90°$, then the Doppler shift of the light emitted towards the Earth is reduced. The maximum radial velocity shift can be expressed as

$$\delta v = \left(\frac{2\pi G}{P}\right)^{1/3} \frac{M_P \sin i}{(M_P + M_\star)^{2/3}} \frac{1}{(1 - e^2)^{1/2}}, \tag{2.5}$$

with e being the eccentricity of the orbit and G the constant of gravity. The mass of the host star must be determined independently from a different measurement, and the eccentricity can be fitted with a non-sinusoidal modulation of the radial velocity curve. A lower limit of the planet's mass can then be inferred from the amplitude
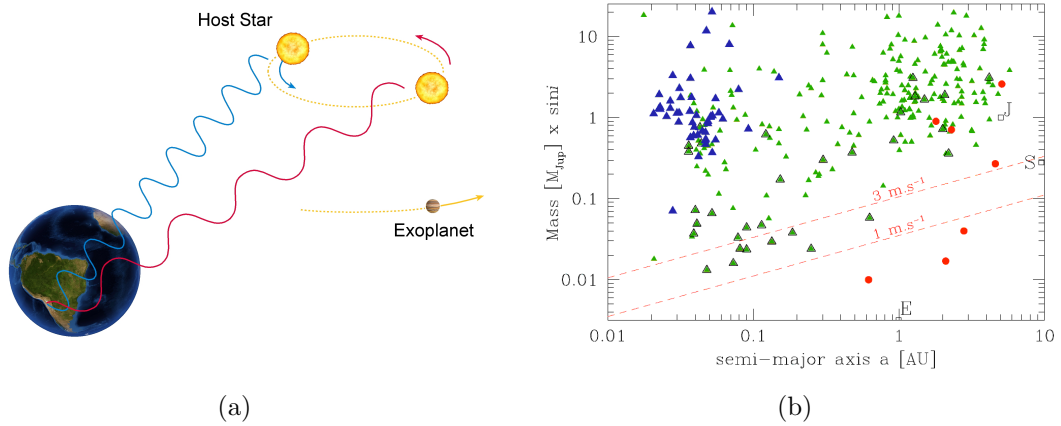
Figure 2.3: *(a) Detecting an extrasolar planet with the radial velocity method. See text for explanations. © ESO 2007 (b) Mass-separation diagram of the 300 exoplanets, detected until 2009. The green triangles refer to exoplanets found by radial velocities. The blue triangles refer to transiting exoplanets. The red circles refer to exoplanets found by microlensing. The bold triangles correspond to exoplanets discovered by the spectrograph HARPS. Lines of radial-velocity semi-amplitude of 1 and 3 m/s have been added by assuming a 1 solar-mass star. The values for Earth (E), Saturn (S) and Jupiter (J) are plotted for comparison. Adopted from [15] by courtesy of F. Bouchy.*

of the variation of the star's radial velocity. The inclination angle, however, must be determined independently, which is a drawback of this method.

There are a few different, alternative methods that also lead to the detection of planets around solar-type stars. If, for example, the orbital plane coincides very well with the line of sight, the planet will eventually cross in front of the star and a dip in the luminosity curve can be observed [75]. Alternatively, if the host star is passing in front of another more distant star, gravitational lensing will lead to a well-known, symmetric light-curve profile. Any disturbance can reveal the presence of a planet orbiting the foreground star [76]. Finally, planets can be detected by direct imaging, i.e. detecting a dim light source orbiting the host star [13]. For a more detailed review of these and other — yet unsuccessful — methods, see [12].

Most planets detected so far either orbit their host star in relatively small distances (termed "hot Jupiters") or the stars themselves are rather small. The reason for this is: even the HARPS spectrograph — despite having the highest sensitivity for radial velocity changes of all instruments presently available — can until now only be calibrated with a repeatability of about 24 cm/s, limited by the calibration source [16]. The Earth, however, induces a recoil of only 9 cm/s semi-amplitude on the Sun. Detecting a similar, extra-solar system thus requires a spectrograph with a calibration capable of measuring a 6 cm/s shift, when demanding a 3σ significance.

2.2.3　Accelerated expansion of the universe

A clue to answer one of the biggest mysteries in modern physics — the composition and, linked to it, the fate of our universe — can be found in directly observing the temporal evolution of the redshift z of distant cosmic objects. If light is emitted at times t_s and $t_s + \Delta t_s$ from a distant, comoving object, it will be detected on Earth at times t_0 and $t_0 + \Delta t_0$, which are connected by [77]

$$\int_{t_s}^{t_0} \frac{\mathrm{d}t}{a(t)} = \int_{t_s+\Delta t_s}^{t_0+\Delta t_0} \frac{\mathrm{d}t}{a(t)}. \tag{2.6}$$

$a(t) = (1 + z(t))^{-1}$ is the scale factor of the universe, normalized to unity at zero redshift when the age of the universe is t_0. The change in redshift of the source as a function of time is then given by [78]

$$\dot{z} = H(0)(1 + z) + H(z). \tag{2.7}$$

The variation of the redshift of a distant, cosmic object without peculiar motion is thus caused by the acceleration or deceleration of the universe, i.e. by the variation of the Hubble parameter $H = \dot{a}(t)/a(t)$.

Assuming a homogeneous, isotropic mass distribution, general relativity will lead to a specific metric. Inserting this so-called Robertson-Walker metric in the field equations of the theory will lead to the simplified Friedman equations [79]. In the case of general relativity, it reads

$$H(z) = H_0 \left[\Omega_R a^{-4} + \Omega_M a^{-3} + (1 - \Omega)a^{-2} + \Omega_\Lambda a^{3(1+\omega_\Lambda)} \right]^{1/2}, \tag{2.8}$$

where Ω_M, Ω_R and Ω_Λ are the energy densities of matter, radiation and a cosmological constant Λ in terms of the critical density. $\Omega = \Omega_R + \Omega_M + \Omega_\Lambda$ is the total energy density, which equals the critical density in a flat universe. The energy density attributed to a non-zero cosmological constant is termed "dark energy" and is assumed to fulfill an equation of state that relates its pressure p_Λ to its energy density ρ_Λ by $\omega_\Lambda = p_\Lambda/(\rho_\Lambda c^2)$. In the case that dark energy is vacuum energy, $\omega_\Lambda = -1$ [80]. The radiation energy density can be neglected, as $\Omega_R \ll \Omega$.

The resulting variation of the redshift during a period Δt_0 can then be written as [81]

$$\delta v = -H_0 \Delta t_0 c \left[\Omega_M (1 + z_s) + (1 - \Omega) + \Omega_\Lambda (1 + z_s)^{-2} \right]^{1/2}. \tag{2.9}$$

Meanwhile, astronomical observations of type Ia supernovae [4, 5], the cosmic microwave background [6] and the large scale galaxy distribution [7] agree very well with each other and independently confirm a spatially flat universe with one third of its total energy being matter ($\Omega_M \approx 1/3$) and the rest consisting of dark energy ($\Omega_\Lambda = 2/3$). According to these parameters, the expansion of the universe is presently accelerating.
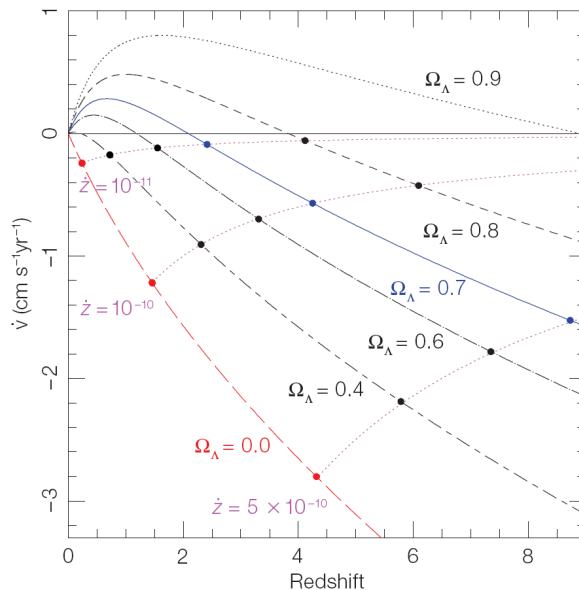
Figure 2.4*: Evolution of the change in radial velocity $\dot{v}$ as a function of redshift. The cosmological parameters have been fixed to $\Omega = 1, H_0 = 70\,km/(s\,Mpc)$ and different values of Ω_Λ have been considered. The $\Omega_\Lambda = 0.7, \Omega_M = 0.3$ cosmology is shown with a blue solid line, and the Einstein-de Sitter model ($\Omega_\Lambda = 0, \Omega_M = 1$) is plotted with a red long-dashed line. The filled circles connected by dotted lines show loci of constant $\dot{z}$, in units of yr^{-1}. Adopted from [20].*

In 1962, the direct observation of the acceleration of the universe's expansion (which actually was thought to be a deceleration at that time), via measuring the variation of the redshift of distant objects, was proposed [8] but considered impossible to perform. This method qualitatively differs from those mentioned above in a key feature — it measures the *dynamics* of the expansion [82]. Additionally, deriving the expansion history is independent from theories such as general relativity. In contrast, all the other observations are *geometrical* measurements, i.e. they map out space, its curvature and its evolution and need a theory of gravity to extract the expansion history of the universe. Observing accelerating expansion in real time would instead provide a truly independent method of measuring the cosmological evolution.

Of course, suitable objects must be found that reliably trace the Hubble flow, i.e. whose redshift variations are not dominated by peculiar motion and acceleration. Additionally, the sources should be bright, despite being so far away (objects with $z \gtrsim 4$ are mandatory), and the detected spectrum should have many and sharp features so that one is able to average over many lines from one object. As in the case of the search for a variation of fundamental constants, intergalactic clouds illuminated by distant quasars are such suitable objects. Intergalactic hydrogen,

which leads to absorption of the Lyman α line, is especially interesting, because it creates a very dense structure in the quasar spectrum. A simulated spectrum of this so-called "Lyα-forest" can be seen in figure 2.5. Various observations and simulations (see [83, 82] and references therein) have been performed and show that the peculiar motion of these clouds is truly negligible, making them a well-suited accelerometer.

With today's improved technology, the direct observation of an accelerating universe seems to become feasible in the near future. In figure 2.4, the expected redshift variation is plotted against the observed redshift for different cosmological models with a flat curvature. For an observation time of 10 years, the spectra should shift by 1 to 10 cm/s, depending on the redshift of the object. Next generation telescopes with a mirror diameter of more than 30 m, combined with highly efficient, high-resolution spectrographs will have enough light-collecting power to observe these quasars with a sufficient signal-to-noise ratio. In 2005 the COsmic Dynamics EXperiment (CODEX) was thus proposed [20], using five identical, high-precision spectrographs to measure the light collected by the future "European Extremely Large Telescope" (E-ELT). Obviously, this observation will only be feasible with a wavelength calibration that can resolve redshift variations of 1 cm/s with a repeatability over at least a decade. Especially for this observation, an absolute frequency calibration is beneficial to enable the comparison of data from different epochs taken with different spectrographs.

2.3   Present limits of spectroscopic observations

2.3.1   Technical challenges of a high precision spectrograph

As the three examples above have shown, high precision spectroscopy is an enabling technology for the ambitious observations that are planned in the near future. In laboratory spectroscopy there has always been the tendency to improve the resolution and accuracy of a measurement too. There have been two crucial inventions within the last 50 years that dramatically improved the measurement accuracies. The first of these has been the introduction of laser spectroscopy, with which the transition of interest with a narrow band light source can be exited. This allows e.g. for Doppler-free spectroscopy and therefore enables measurement of the natural linewidth of a transition. The second innovation was the shift from wavelength to frequency measurements. Measuring frequencies means directly counting the cycles of the light's electric field with reference to the cycles of an atomic standard of time. Wavelength measurements, in comparison, use spectrographs or interferometers and are sensitive to wavefront deformations of the light that is being analyzed.

For a spectroscopic measurement in astronomy, these lases spectroscopic techniques are obviously not applicable. It is neither possible to excite cosmic objects nor is it at present feasible to set up a heterodyne frequency measurement of starlight.

The latter is mainly prevented by the Earth's atmosphere through which the light must travel. When seen from outside of our atmosphere, a star is a nearly perfect point source with its light arriving in planar waves. Unfortunately, the turbulences of air above the telescope lead to strong deformations of the wavefronts. This effect is characterized by the "seeing" parameter which is defined as the FWHM diameter of the point-spread-function measured with the telescope in arcseconds. At a good observation site, one can have a seeing of 1"; at exceptional sites, such as in Hawaii it can be below 0.5" [84] or even at 0.3" if one were willing to put a telescope in the middle of Antarctica [85]. This can be compared with the theoretical angular resolution ϕ of a telescope at a wavelength λ and for a mirror diameter D, which is given by the Rayleigh criterion

$$\sin \phi = \frac{\lambda}{D}. \tag{2.10}$$

A diffraction limited 4 m class telescope would thus have a maximal resolution of ~ 0.025" — but fed with a ~ 1" multimodal input field there is virtually no chance of coupling the light efficiently to a singlemode fiber. This would be the prerequisite for setting up a heterodyne frequency measurement. If, on the other hand, an adaptive optics setup could be implemented to counteract atmospheric distortions or if the telescope were put into space, there could be a realistic chance to couple a significant amount of starlight into a singlemode fiber. Adaptive optics, however, is presently not available in the visible regime. Consequently, one has to cope with the image of a star being a 1" blob instead of a nicely diffraction limited spot when using ground based telescopes.

Performing a high precision spectroscopic measurement on distant cosmic objects requires a large effort in the construction of the spectrograph and detector. Assuming a spectrograph with a resolution of 5 GHz, sampled at 3 pixels per resolution element with 15 μm pixel size, a line shift of 1 cm/s (20 kHz at 500 nm wavelength) corresponds to a shift on the detector of 0.2 nm. This corresponds to the diameter of one silicon atom on the CCD! Any mechanical deformation will lead to a shifted spectrum, and thus, a very rigid construction in a temperature stabilized chamber is mandatory. Environmental changes in temperature, air pressure and humidity would affect the refractive index of air, and therefore, the spectrograph is best put in vacuum. All these measures should be taken to make a spectrograph passively as stable as possible but will of course not be sufficient to guarantee a repeatability of the line position on the sub-nm scale. Hence, any residual change of the instrument must be monitored via continuous calibration.

Since the image of the starlight in the focus of the telescope is blurred and unstable in position, the mechanical stability of the spectrograph is not the only prerequisite for a high precision measurement. One way of minimizing the effect of a variable image is coupling the light to the spectrograph via an optical fiber. Replacing a slit-coupled spectrograph with a fiber-coupled instrument was one major improvement towards high precision spectrographs, and it serves two purposes at

the same time. On the one hand, it facilitates decoupling the atmospheric blurring and telescope motion from the spectrograph's input aperture. On the other hand, calibration light can be fed to the same fiber, ensuring a very good spatial overlap with the starlight, which will reduce systematic shifts.

Still, care has to be taken to minimize a potential modal mismatch between signal and calibration light. As already explained, the starlight cannot be efficiently coupled into a singlemode fiber. Only a multimode fiber can collect most of the photons, arriving at the telescope's focal plane. The numerical aperture can then be designed to fit the telescope's focal ratio such that a good occupancy of the fiber's transversal mode is achieved. There is, however, a residual pointing sensitivity maintained. If, e.g. a star is not imaged onto the center of the fiber's input facet but to one side, the cylindrical symmetry of the fiber will lead to a good homogenization in azimuthal direction but light at the output will still show an asymmetric radial distribution. Maximizing the occupancy of the fiber modes is obviously the best solution to this problem. If all modes were occupied, there could be no remaining dependence on the input field distribution (provided that the fiber is long enough that radiative modes are sufficiently suppressed). Thus, means to scramble the modes are incorporated in the multimode fiber section. They can be dynamic, e.g. with a motor continuously bending the fiber [86], or static, by exchanging the fiber's near and far field in an assembly of additional optics [87]. When dealing with coherent light, there is the additional problem of speckles [88]. This is especially relevant when using a frequency comb for calibration and is explained in more detail in section 5.4.

2.3.2 Photon noise implications on spectrograph design

Aiming at a maximum sensitivity for Doppler shift variations is not the same as simply maximizing the spectral resolution of a spectrograph [89]. The quantity of interest is the photon noise limited uncertainty σ_v, which depends on the flux S, the spectral bandwidth $\Delta\lambda$ and the spectral resolution R. In the case where the stellar lines are unresolved, according to [90], the dependency is:

$$\frac{1}{\sigma_v} \propto S^{0.5}\Delta\lambda^{0.5}R^{1.5}. \tag{2.11}$$

For a single, Doppler broadened line, the photon noise is on the order of a few m/s. Even if the signal-to-noise ratio could be improved, it would still be impossible to determine the center of a single line or a blended feature of several GHz width with an uncertainty of $20\,\mathrm{kHz}$ (corresponding to $1\,\mathrm{cm/s}$). Hence, the only chance to achieve a sensitivity to shifts of this order is to average over many lines, resulting in the dependence of the photon noise on spectral bandwidth.

Increasing any of the parameters on the right-hand side of equation (2.11) will give a lower photon noise but on the other hand is directly connected to increasing
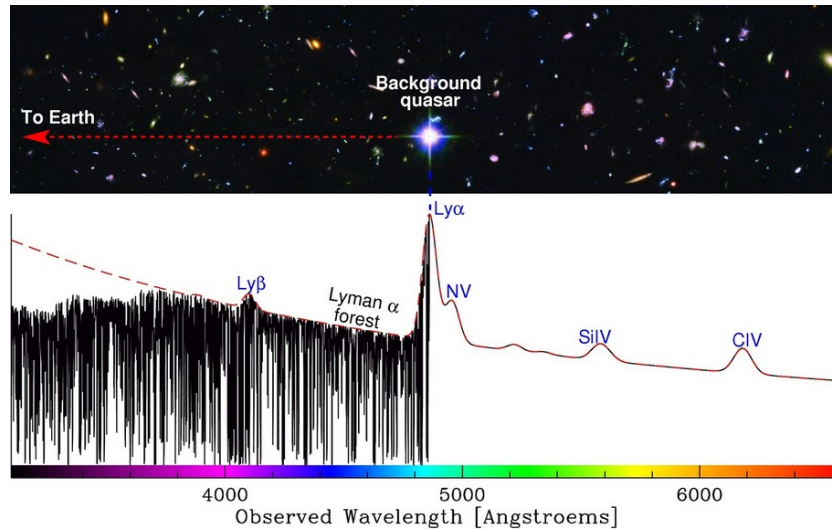
Figure 2.5: *Simulated spectrum of a high redshift quasar with $z = 3$. The Lyα emission line of the quasar is prominent at 486 nm and to shorter wavelengths Lyα absorption lines are impressed on the spectrum by hydrogen clouds in the line of sight to the quasar (Lyα-forest). Figure with courtesy of M. T. Murphy [91].*

the physical size of the instrument and/or telescope. In the design of a spectrograph several trade-offs must thus be made.

First, let's consider the wavelength range: In general, the features of the observed spectra are unresolved, leading to a complex, blended intensity profile. For main-sequence stars (interesting for the search of exoplanets) their modulation is weaker in the red and infrared region, resulting in a smaller signal-to-noise ratio in this wavelength range. When observing the Lyα-forest of intergalactic hydrogen clouds in the line of sight of a quasar (for observing the acceleration of the universe), a long-wavelength cut-off is given by the redshifted Lyα emission line of the quasar (see figure 2.5). For the most distant quasar presently known [92], the Lyα line is shifted to 903 nm, corresponding to $z = 6.43$. Most quasars, however, have their Lyα line shifted to below 800 nm. The first trade-off for the design of a spectrograph is therefore to limit the spectral bandwidth of the instrument to the visible and near-UV region and thereby sacrifice some spectral information at longer wavelengths.

The spectral resolution has the largest effect on the Doppler shift sensitivity, but it cannot be changed independently of other parameters. It is linked to the size of the echelle grating in terms of the collimated beam diameter h and the grating's blaze angle β, as well as to the diameter of the input slit or fiber. The latter depends on the telescope's diameter D and the field of view ϕ, accepted by the fiber such that the maximum spectral resolution R_{max} is given by [89]:

$$R_{max} = \frac{2h \tan \beta}{\phi D}. \tag{2.12}$$

With a given diameter of the telescope, one should use the largest grating available. Its blaze angle should also be as large as possible but of course not at the prize of overly reduced efficiency. The remaining parameter is the field of view which should be minimized. This can only be done at the immediate expense of slit efficiency and therefore flux. A compromise depending on the instrument and telescope being employed must thus be worked out.

There is essentially only one way to increase the flux: increase the size of the telescope. Presently, the best spectrograph for high precision radial velocity measurements is installed at a telescope with a 3.6 m primary mirror. Due to its excellent performance and high scientific output, ESO is planning to install conceptually similar but improved spectrographs at the existing, larger 8 m "Very Large Telescopes" (VLT) and also at the future 40 m class E-ELT. Only with a telescope of this size will the signal-to-noise ratio of distant quasars be high enough for a photon noise limited uncertainty below 1 cm/s per exposure.

2.3.3   State-of-the-art calibration sources

Reducing the photon noise of the starlight below the level necessary to detect the effects of interest is one condition to enable a spectroscopic measurement. On the other hand, a wavelength measurement is, as explained above, always determined by a comparison with a reference wavelength, i.e. calibration light. As a consequence, the calibration source needs to have sufficiently low photon noise, as well as no unmodelled systematic uncertainties.

The spectrograph can either be calibrated before and after the measurement or the calibration can be superimposed with the starlight. When calibrating the spectrograph at different points in time, one relies on the passive stability of the spectrograph and is unable to track drifts during the measurement. When superimposing a calibration with the starlight, one could either use absorption cells or add calibration light. Both methods decrease the available signal-to-noise ratio, either by reducing the number of photons arriving at the detector or decreasing the stellar flux to avoid saturating the detector when adding calibration light. A hybrid method that combines the advantage of undisturbed spectra with the sensitivity to instrumental drifts during an acquisition is the simultaneous calibration method [93]. The spectrograph is fed – preferably from two fibers – with calibration and starlight in two separate input apertures. Both inputs are imaged onto the detector with a small offset in the cross-dispersed direction, thereby using all photons of the signal while performing a calibration at the same time.

The classical source for a superimposed calibration is an absorption cell (e.g. filled with iodine). Molecular iodine is indeed the best compromise when choosing an absorptive calibration source for the visible wavelength regime [94]. Still, it has several disadvantages in addition to the fact that it consumes signal flux. Most importantly, the usable wavelength range covers only 500 to 620 nm where the line

density is high enough to provide a high calibration information. Hence, the entire blue part of the spectrum, where the stellar signal possesses the highest information density, cannot be calibrated. Furthermore, the line shapes are pressure and temperature dependent, and there might be spurious lines from traces of foreign gas, varying from cell to cell. In conclusion, a repeatability of about 1 m/s is at present the limit for this technique [95] and, together with the incomplete wavelength coverage, this makes it inapplicable for the measurements proposed above.

A natural source of absorption lines is the atmosphere, and these so-called telluric lines are inevitably imposed on any stellar spectrum. They are, however, not very dense, rather broad and even change with atmospheric conditions. The maximum achievable repeatability of 2 m/s [96] is clearly not competitive.

The best calibration method developed so far is the simultaneous calibration with a hollow-cathode lamp. A well-suited lamp combines a thorium cathode with argon buffer gas (Th-Ar). The emission lines used for calibration are the thorium lines. They are found in great numbers over the whole visible and near-infrared range. Thorium is also mono-isotopic without a hyperfine structure, which leads to narrow, highly symmetric line profiles. The argon lines, while often much stronger than the thorium lines are susceptible to pressure shifts and therefore cannot be used when aiming at highest calibration performance. Thorium lines, on the other hand, do not show this sensitivity and their spectrum shows a repeatability almost at the photon noise level [16]. For example, over a wavelength range from 380 to 680 nm, the photon noise limit amounts to ≈ 10 cm/s per exposure (when performing measurements with the HARPS spectrograph), while the calibration repeatability is 20 cm/s. Residual drifts of the spectrograph have already been removed in this measurement, and the deviation from the statistical uncertainty is caused by systematic uncertainties of the calibration. These uncertainties originate from a dependency of the thorium line positions on operating conditions of the spectral lamp.

This is to date the best repeatability with which an astronomical spectrograph can be calibrated. It is, however, not sufficient to perform the aforementioned observations, which are in need of a 1 cm/s calibration. Since the repeatability of the Th-Ar calibration cannot be improved and absorption cell techniques are also no alternative, a new calibration method must be employed for the next generation of spectrographs.

Recently, a passive, broadband Fabry-Pérot cavity illuminated by a white light lamp was proposed as a calibration source [97]. It can overcome several of the disadvantages of previous methods. First, there are no blended lines complicating the calibration. When using broadband mirrors in combination with a truly white light source, all lines have about equal intensity, and therefore, each line can be detected with minimum photon noise. The spacing between the mirrors can be chosen according to resolution of the spectrograph at which it is put to use. Hence, the line spacing can be tuned to have a minimum separation without blending, reaching the optimum in photon noise for any given detector. Covering the whole

visible spectrum with this calibration source readily gives a sub-cm/s photon noise limit. There are, however, concerns about the long term performance of such a cavity. Of course, it must be operated in a thermally stabilized environment and under vacuum. Despite this, one must still watch out for any residual expansion. If, for example, making the cavity from a glass with a first-order zero thermal expansion point (a temperature, where the thermal expansion and its first derivative are zero) and stabilizing it there, a residual linear drift of $\approx 5\,\mathrm{kHz}$ per day $(0.25\,\mathrm{cm/s/day})$ can still be observed, due to recrystallization effects of the glass [98]. While this is clearly no problem for a single acquisition or a short series, for observations over several years, the cavities must be monitored. To check the cavity drift on the cm/s level, either an elaborate optical wavelength standard or a frequency comb must be employed.

All preceding calculations for photon noise limited spectroscopic measurements referred to the detection of *variations* of the Doppler shift of a cosmic object. This is what most high precision spectroscopic observations are about. Determining the *absolute* redshift of a star or galaxy with an accuracy of 10^{-9} or better (sub-m/s level) is currently not mandatory for any observation. Nevertheless it would be desirable to be able to assign absolute frequencies, accurate at the cm/s level, to cosmic spectra, especially for long term projects as e.g. the observation of the universe's acceleration. This would facilitate comparing observations made with different spectrographs and/or telescopes.

The most accurate and complete characterization of thorium lines are found in the catalog by Palmer & Engleman [99]. The measurement was performed with a Fourier transform spectrometer and has an accuracy of 20 to 50 m/s. Determining absolute frequencies with a passive Fabry-Pérot cavity would also prove difficult, because due to group velocity dispersion of the mirrors or the intermediate medium, the line spacing is not equidistant. Thus obtaining an absolute frequency calibration below the m/s level does not seem to be feasible with the calibration sources presented above.

2.4 Frequency combs for spectrograph calibration

2.4.1 A frequency comb − the ideal calibrator

At the beginning of this chapter, it was argued that there is a need for a long-term stable calibration source for astronomical spectrographs, which have a photon noise of about or below one cm/s. A frequency comb, as generated by a femtosecond laser and designed to fit the characteristics of a spectrograph, turns out be an ideal solution. It can overcome all the problems inherent in previously existing methods. Its advantages can be summarized as follows:

- All lines are individually unresolved but resolved from each other:
  The linewidth of a frequency comb line is on the order of one MHz or less and therefore much narrower than the point-spread-function of the instrument (typically a few GHz). In section 3.6, a thorough analysis is performed to determine whether any residual asymmetry in the line shape could affect the calibration. The spacing between calibration lines can be designed by the use of filter cavities (see below) such that each line is well separated from the others on the detector.

- All lines are of about equal intensity:
  The output spectrum of a femtosecond laser has a relatively smooth shape without strong modulations from mode to mode (typically below 10 %). To cover the whole visible range, the spectrum must be broadened and this is typicallly done in a fiber with a high nonlinearity. This process induces intensity variations, also on the line-to-line scale. They are, however, still small in comparison to the variations of lines from spectral lamps or absorption cells, which amount up to several orders of magnitude.

- All lines are equidistant:
  It was demonstrated that all modes of a frequency comb are perfectly equidistant in frequency down to the 10^{-19} level [100]. Frequency conversion processes do not affect this property [101] either. Thus, once one line's frequency is known, there is no doubt about the frequency of any detected line throughout the whole covered range. For calibrating spectrographs, however, care must be taken to use the accurate mode frequencies for an equally accurate wavelength measurement.

- All line positions are linked to an atomic clock:
  The key advantage of a frequency comb, besides the potentially low photon noise, is its reference to an atomic clock. Each line is phase-coherently locked to this reference and is therefore as accurate and has the same long-term stability. With an inexpensive, off-the-shelf clock, this limit is already at the mm/s level (10^{-11} $\Delta v/c$). The reference to the definition of time enables on the one hand absolute frequency measurements and on the other hand ensures long-term comparability with data taken at other epochs and/or with other instruments.

- The mode spacing and line position is tunable:
  Although every frequency is fixed to a known reference, the lines might be intentionally tuned without losing the phase-lock. By doing this, it becomes feasible to scan the calibration source over every pixel of the detector and calibrate for pixel-to-pixel and even intrapixel sensitivity variations.

A frequency comb as calibration source has the potential to solve all scientifically important problems of the calibration, but comes at the prize of a more complex and expensive system, e.g. in comparison with spectral lamps or absorption cells. One should, however, consider that those two devices have been known and improved for decades, while the first frequency comb was realized only ten years ago. There has already been quite impressive progress in making such a system more robust, economic and turn-key, e.g. by using fiber-based lasers, amplifiers and interferometers. Alternative concepts of generating a frequency comb, e.g. by nonlinear parametric amplification in high-finesse microcavities [102, 103], might further simplify the setup in the future.

2.4.2   Concept of a frequency comb

In general, a frequency comb is a coherent light source with a spectrum consisting of a large number of modes whose phases, spacing and absolute position are stabilized to a reference clock. Many realizations of a comb are included in this definition, e.g. femtosecond laser-based combs [104], cascaded frequency-modulated cw-lasers [105] or combs generated by cascaded parametric amplification in microcavities [102, 103] or highly nonlinear fibers [106]. Today, the most common and versatile comb generator is a phase-stabilized femtosecond (fs) laser. In principle, any such laser can be used to generate a frequency comb that gives access to wavelengths ranging from the visible (using Ti:Sa lasers) over the near infrared (Yb:fiber, Cr:LiSaF, Er:fiber, Tm:fiber) to the mid infrared (Cr:ZnSe) and fundamental mode spacings ranging from several MHz to several GHz. Additionally, since fs pulses have high pulse energies, frequency conversion processes, such as sum and difference frequency generation, spectral broadening, high harmonic generation or even the generation of THz radiation, can efficiently be driven. This versatility enables the design of a comb that fulfills requirements of any individual spectrograph, whereas all alternative comb generators lack one or another important design parameter. For this reason, a fs laser frequency comb is the optimum choice for a calibration source, and its principles are explained in the following.

A comb of equally spaced frequencies is obviously a picture derived from the frequency domain. To understand its principle, it is, however, helpful to start with a time domain picture. A train of pulses emitted from a laser can be described by an electric field

$$E(t) = A(t) \; e^{-i2\pi f_c t} + \text{ c.c.} \tag{2.13}$$

$$A(t) = A(t - T), \tag{2.14}$$

with a carrier frequency f_c and a periodic envelope $A(t)$. The pulses are separated in time by the distance T, corresponding to a pulse repetition rate $f_r = 1/T$. In case the carrier frequency is not an exact multiple of the repetition rate, the pulses
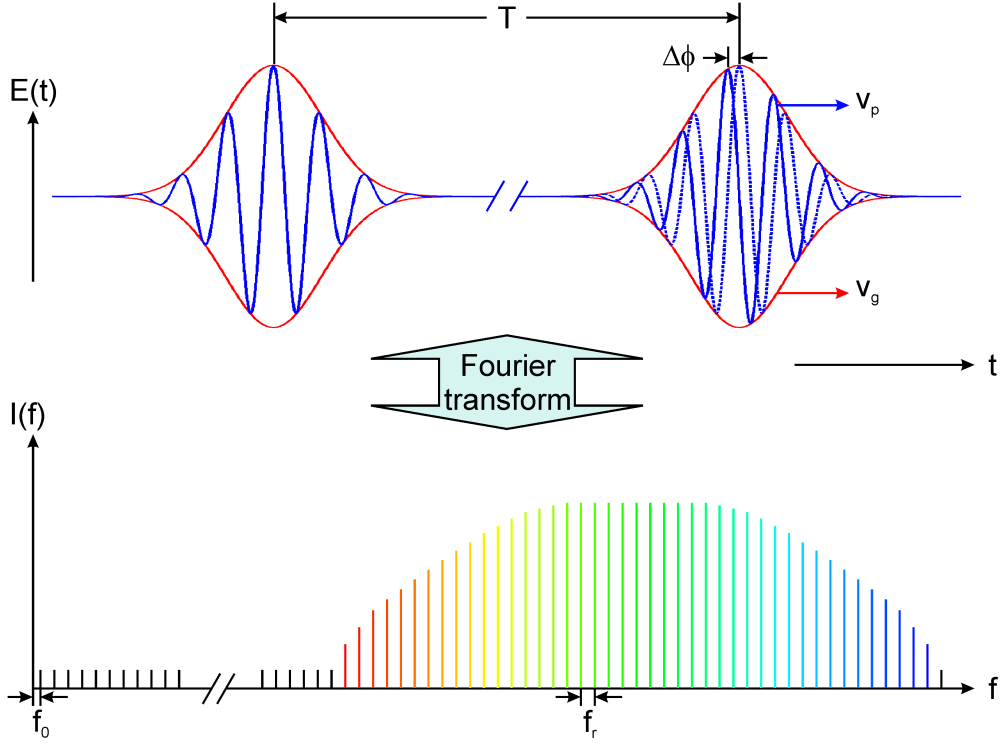
Figure 2.6: *Relationship between an equidistant pulse train and its comb-like spectrum. The pulse separation T translates into the repetition rate $f_r = 1/T$ and the carrier-envelope phase $\Delta\phi$ into the offset frequency $f_0 = (\Delta\phi/2\pi)/T$. Due to a difference between group velocity v_g and phase velocity v_p, the carrier wave slips with respect to the pulse envelope by $\Delta\phi$ from pulse to pulse.*

will not perfectly reproduce, but the carrier wave will instead slip by an amount of $\Delta\phi$ relative to the envelope function from pulse to pulse. Performing a Fourier transformation on such a train of pulses yields a comb-like spectrum, which is shown in the now classic illustration of figure 2.6. This can be easily understood, since any periodic function can be described as a discrete Fourier series with every Fourier component oscillating at a harmonic of the inverse repetition time

$$A(t) = \sum_{n'} A_{n'} e^{-in'2\pi f_r t} \qquad (2.15)$$

$$E(t) = \sum_{n'} A_{n'} e^{-i2\pi(n'f_r + f_c)t} + \text{ c.c.} \qquad (2.16)$$

Each frequency component is separated from the carrier frequency by an integer multiple of the pulses' repetition rate, and thus, the spacing between any two neighboring modes is exactly equal. It is, of course, mathematically possible not to take the carrier frequency in the 100 THz regime as reference for the summation, but to

choose an offset frequency $f_0 < f_r$ and integer summation indices $n \in \{0, 1, 2 \ldots\}$ such that

$$E(t) = \sum_n A_n e^{-i2\pi(nf_r + f_0)t} + \text{ c.c.} \tag{2.17}$$

The frequency f_n of any comb mode is thus determined only by the repetition rate f_r, the offset frequency f_0 and the individual mode number n, connected by the simple equation

$$f_n = nf_r + f_0. \tag{2.18}$$

Introducing the offset frequency is not just a theoretical construct; it has an important physical meaning as well. It is defined as the frequency difference by which the carrier frequency is not an exact multiple of the repetition frequency, which leads to the phase difference $\Delta\phi$ between two consecutive pulses. The offset frequency therefore fulfills the relation $f_0 = (\Delta\phi/2\pi)/T$ and gives the rate by which the carrier wave slips relative to the pulse envelope. For this reason, it is also termed carrier-envelope offset frequency. Another way of looking at it is that the carrier is propagating with the phase velocity v_p, but the envelope with the group velocity v_g. This leads to the phase slippage of the carrier wave with respect to the envelope during one round-trip within the laser cavity. It will become important to note, that being able to influence the difference between phase and group velocity enables control over the offset frequency.

The immense potential of equation (2.18) stems from the fact that two radio frequencies exactly determine the frequency of every single optical frequency contained in the comb's spectrum. Putting this notion to use implies that it is possible to measure an optical frequency $f_n > 100\,\text{THz}$ by counting two radio frequencies $f_0, f_r \lesssim 10\,\text{GHz}$, which is a well-developed technology and can be performed with very high precision.

In metrology a frequency comb encompasses not only generating a train of pulses with a comb-like spectrum but also stabilizing the phases of its two defining radio frequencies relative to a reference oscillator such as an atomic clock. This implies first that one can detect them and second that one has access to two parameters of the system that control them (preferably orthogonally). On the one hand, the stabilization serves to remove thermal and acoustic noise, as well as other environmental influences (air pressure, humidity etc.), on the comb's modes. On the other hand, once the stabilization is accomplished, the phase relation of every comb mode relative to the reference is fixed and maintained. Each mode's long-term stability (within the servo bandwidth of the stabilization) and accuracy is then given by the reference oscillator.

2.5 Requirements for a frequency comb as a spectrograph calibrator

Two major criteria must be fulfilled to enable the use of presently available frequency combs to calibrate astronomical spectrographs: the comb's spectrum must cover the spectral bandwidth of the instrument, and the comb's mode spacing must exceed the instrument's resolution. As there is no laser gain material that covers the desired spectral range from 400 to 800 nm, the spectrum of any comb generator must be broadened. This problem was already faced when the first frequency combs were developed, since an octave-spanning spectrum is highly beneficial to facilitate the detection of the offset frequency in a f-$2f$ interferometer (see section 3.4). The solution to this challenge is essentially the same in both cases. By injecting the light into a highly nonlinear medium, such as a specially designed photonic crystal fiber, the spectrum can be broadened as desired. The more interesting question is, however, how to achieve the required spacing of the comb modes. To answer this, the optimum mode spacing must first be determined.

2.5.1 The optimum mode spacing

It was stated above that each line should be well separated from another but individually unresolved. According to [107], the uncertainty σ_i of a single line's position on the CCD, which samples the FWHM of the point-spread-function with $n > 1$ pixels, is given by

$$\sigma_i = A\frac{\text{FWHM}}{\text{S/N} \times \sqrt{n}} \ , \tag{2.19}$$

with S/N being the peak signal-to-noise ratio per pixel across the line (usually obtained at the line center). The prefactor A depends on both the functional form of the line profile and the relationship between S/N and pixel intensity. In the case that photon noise dominates the detector noise and the line shape is Gaussian, simulations show that $A \approx 0.41$ [21].

Choosing reasonable numbers for a spectrograph's parameters gives an estimate of the expected repeatability that a calibration with a frequency comb could achieve. A typical CCD can have 2048 pixels and a maximum S/N of 500 per exposure. The FWHM of a line should be sampled by 3 pixels, and each line should be well separated from another but close enough not to have unexposed pixels. A compromise would be a separation of 2.5 resolution elements. This would distribute $N \approx 272$ lines in one echelle order, and with a resolution of $R = 150000$ (i.e. FWHM = 2 km/s), the photon noise limited repeatability would be $\sigma_v^{order} = \sigma_i/\sqrt{N} \approx 0.41 \times 2\,\text{km/s}/(500 \times \sqrt{3 \times 272}) = 5.7\,\text{cm/s}$ per exposure.

A more rigorous calculation was performed by Murphy et al. [21], which included the dependence of spectral resolution on the echelle order. They simulate a comb

spectrum and calculate the repeatability as a function of the comb's mode spacing. For the parameters given above, the optimum spacing would be 15 GHz, corresponding to three times the spectrograph's resolution at the center of the assumed wavelength range. Depending on the echelle order, the photon noise limited repeatability per order is about 6 to 7 cm/s, and assuming a total wavelength range of 380 to 820 nm, this would correspond to an overall repeatability of $\sigma_v^{total} = 0.45$ cm/s per exposure. This result is very consistent with the back-of-the-envelope calculation above, and therefore confirms that the simplifications made were appropriate. The general expression for the overall repeatability per exposure is given by

$$\sigma_v^{total} = 0.45 \left(\frac{500}{\text{S/N}} \right) \left(\frac{1.5 \times 10^5}{R} \right)^{1.5} \text{cm/s}. \tag{2.20}$$

This relation is equivalent to equation (2.11), when considering that the prefactor is dependent on the wavelength range (though not exactly inversely proportional to the square root of the bandwidth) and S/N is proportional to the square root of the flux for dominating photon noise.

Over a range of 0.5 to 5 times the optimum mode spacing, the repeatability per echelle order does not vary by more than a factor of 2. It is therefore possible to use one fixed mode spacing and almost optimally calibrate over an octave-spanning spectrum. Most importantly, however, the photon noise limited overall repeatability is below one cm/s with the design parameters assumed above readily achievable using state-of-the-art technology. A frequency comb must therefore be developed to have a mode spacing of about 15 GHz with a spectral coverage of about 400 to 800 nm.

2.5.2   Increasing the comb's spacing

The spacing between a frequency comb's modes is given by the repetition rate of the laser, which serves as a comb generator. It is therefore determined by the physical size of the oscillator. A 10 GHz spacing corresponds to an empty cavity length of only 3 cm. There is only one laser demonstrated to have such a high repetition rate and emit a broad spectrum and sub-100 fs pulses [108]. It is a Ti:Sa laser, which has a footprint smaller than a 2-cent coin. In general, however, everyday lab practice shows that a bulk crystal laser, such as Ti:Sa or Cr:LiSAF, is not the best idea when aiming for an inexpensive, low maintenance and turn-key system. A much more promising way is to develop a fiber-laser based system. On the other hand, a fiber is an extended medium, and there is probably no hope to ever build a fiber resonator with more than 10 GHz fundamental mode spacing, which is additionally able to emit mode-locked femtosecond pulses. The key word in the last sentence is *fundamental*, since there are indeed fiber lasers that are harmonically mode-locked at high repetition rates, i.e. they emit pulses at a harmonic rate of the oscillator's fundamental repetition frequency. This might be an alternative to the solution

proposed hereafter and is currently being investigated at MPQ. The first preliminary results are discussed in the outlook (see chapter 6).

The highest fundamental repetition rate of a sub-ps fiber oscillator is $1\,\mathrm{GHz}$ [109, 110] and for a sub-100 fs laser only $670\,\mathrm{MHz}$ [111], which was developed during this work and will be described in section 3.3.2. Although there is some effort to decrease the cavity length and increase the mode spacing, it is obvious that an additional measure must be taken to achieve $> 10\,\mathrm{GHz}$ spacings. Fabry-Pérot type cavities (FPCs), acting as mode filters, have been proposed to provide a solution [21]. Their filter function is comb-like with a nearly equidistant and tunable spacing of transmitted modes. In section 3.6, the details of FPCs and their successful implementation in our frequency comb system are presented.

Chapter 3

Fiber-based frequency comb system

3.1 Choice of the appropriate comb generator

In the previous chapter, it was shown that a frequency comb is the ideal calibrator for astronomical spectrographs, if matches the spectrograph's properties in terms of spectral coverage and mode spacing. There was, however, no simple and suitable frequency comb system available when this project was started. A variety of methods has been developed in recent years for generating phase-locked, equidistant sets of modes, but as discussed in section 2.4, only a fs-laser based comb can be modified with state-of-the-art technology to fulfill all the requirements.

To further narrow down the choice of which system shall be developed, fs-laser based combs can be classified into two groups: combs based on bulk crystal lasers and based on fiber lasers. Crystal-based lasers consist of a crystalline gain material and a free-space setup of mirrors or other optical components. Various materials have a gain bandwidth, large enough to support sub-100 fs pulses, which can then be used as generators of frequency combs. When using, e.g. a Ti:Sa-laser, the gain bandwidth covers already half of the desired wavelength range, and very short pulses can be obtained, making wavelength conversion steps very effective. When this project was initiated, the highest repetition rate from a Ti:Sa-laser was only about 3.5 GHz [113]. To arrive at the desired mode spacing of more than 10 GHz, filter cavities would be necessary, which would lead to an inevitable reduction in pulse energy. Reamplification would require another gain crystal, further complicating the setup. In the meantime, an oscillator with a fundamental repetition rate up of 10 GHz and subsequent spectral broadening has been demonstrated [108]. If the size of the already impressively small oscillator could be further reduced, this frequency comb would be in principle a good candidate for a suitable calibration system. There is, however a major drawback of all free-space, crystal-based fs-lasers, namely their mechanical (non-)robustness. Their performance is very susceptible to

tiny misalignments due to changes in the ambient conditions. So far, all fs-Ti:Sa lasers have required regular maintenance by skilled personnel for daily operation. This is the main reason why a fiber-based comb system has been developed in this work, despite having the disadvantage of starting with repetition rates below 1 GHz. On the other hand, the possibility of setting up simple, single-pass fiber amplifiers compensates this disadvantage, since after each filter stage, the rejected power can be replenished. At the end, even a high-power amplifier, delivering pulses with an average power of several watts can be used to achieve sufficient pulse energies to drive wavelength conversion processes. A further advantage of fiber lasers is, that they can be pumped by inexpensive laser diodes. This reduces the costs of such a system significantly with respect to solid-state lasers, which so far require a large-frame pump laser. This is an important factor when considering that more than one spectrograph might benefit from a comb-based calibration.

Using the waveguide structure of fibers as a laser cavity was proposed only shortly after the invention of the laser itself [114]. In the meantime, a large variety of dopants has been investigated facilitating emission wavelengths ranging from 0.4 to 4 μm [115]. Only a few transitions of selected materials, however, allow for a mode-locked operation and the generation of sub-100 fs pulses. The first type of fiber laser with a phase-stabilized offset frequency was an Er-doped fiber laser [116, 117], and it was still the only one when this project started. The reason for Erbium playing an extraordinary role in fiber-laser technology is, that its emission wavelength range coincides with the frequency bands in telecommunication networks. Much effort has been put into the development of fiber-optic components for this wavelength range resulting in a vast choice of well-designed, reliable and inexpensive parts. Furthermore, erbium-doped fibers can be pumped very efficiently at 974 nm which allows for the use of inexpensive, compact and power efficient InGaAs laser diodes.

For the development of a fiber-laser frequency comb for the calibration of high-precision, astronomical spectrographs, Yb-doped fibers offer two advantages over Er-fibers. On the one hand, the emission wavelength range is more suitable for the application in mind. The fundamental spectrum with a central wavelength of 1030 nm only needs to be doubled in frequency to reach the center of the target wavelength range in the visible. On the other hand, the details of the absorption and emission band in Yb-doped fibers result in a small quantum defect between the pump and signal light. As a consequence, high-power amplifiers can be realized with considerably less pump power when using Yb-doped fibers instead of other doped fibers.

For these reasons, a Yb-doped femtosecond fiber-laser was chosen to be the basis of the frequency comb system. In figure 3.1, all relevant components of the system are depicted, and most of them needed to be specially developed for this project. First, a high repetition rate oscillator, capable of generating sub-100 fs pulses, was constructed. Different microstructured fibers were tested to obtain an octave-spanning spectrum and to set up a f-$2f$ interferometer for the detection and
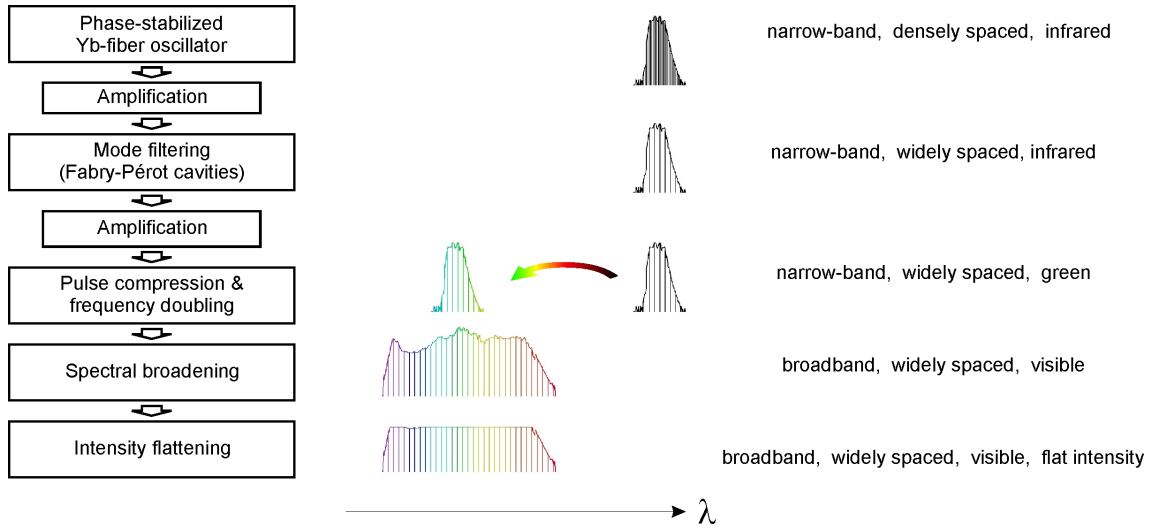
Figure 3.1: *Schematic of the frequency comb system developed in this work. The individual steps from the oscillator to the final calibration comb and their effect on the spectrum are depicted.*

stabilization of the offset frequency. A very time-consuming part involved finding a suitable design for the fiber amplifiers. Both core-pumped amplifiers and double-clad amplifiers were developed. Core-pumped amplifiers provide moderate powers below 1 W for the f-$2f$ interferometer and the Fabry-Pérot cavities. Double-clad amplifiers generate high powers above 10 W for the frequency conversion steps. Various techniques to stabilize the FPCs to the comb were investigated to increase the mode spacing from sub-1 GHz to more than 10 GHz, and a robust mechanical setup was designed. Transversing fibers amounting to a total length of more than 10 m requires that the pulses be recompressed after passing through the amplifiers and FPCs. Pulses should be as short as possible to efficiently drive the subsequent nonlinear processes. A hybrid grating/prism compressor was set up to compensate second and third order dispersion of the fibers and obtain pulses close to the bandwidth limit. The light is then doubled in its frequency in a selected crystal. Subsequently, tapered PCFs were studied that exhibit enough nonlinearity to broaden the spectrum. Finally, to eliminate the strong intensity modulations after the PCF, a spatial light modulator needs to be set up to act as a high-resolution, adaptive spectral filter. In this chapter, each of these steps is presented in detail (except the spectral flattening, which is discussed in the outlook).

3.2 Femtosecond fiber lasers

Before presenting the details of the Yb-fiber oscillator, used as comb generator, an introduction will be given on the generation of sub-picosecond laser pulses. This

section will not, however, go into great detail on this topic. Two excellent references for further reading are the textbooks by Diels [118] or Agrawal [119].

3.2.1   Optical fibers

A typical optical fiber is a cylindrical symmetric waveguide structure made of glass. The light is guided in a core that has a slightly higher index of refraction than the surrounding cladding. Solving Maxwell's equation for the propagation of light in a fiber leads to the wave equation

$$\nabla E(\omega) + n^2(\omega)\frac{\omega^2}{c^2}E(\omega) = 0, \tag{3.1}$$

with $E(\omega)$ being the Fourier transform of the electric field, n the refractive index and $\omega = 2\pi f$ the optical angular frequency. A detailed derivation of this result and the following can be found in any standard textbook on fiber optics (e.g. [119, 120]). By expressing the wave equation in cylindrical coordinates, it can be easily seen, that (modified) Bessel functions J_m (K_m) are solutions for the spatial distribution of the electric field inside (outside) the core. An eigenvalue equation can be derived determining the modes, which are truly guided in the fiber. The number of guided modes depends on the geometry of the fiber, in particular the core diameter a and the difference in refractive index between core and cladding. It is common to define the normalized frequency V by the relation

$$V = \frac{2\pi a}{\lambda}\sqrt{n_1^2 - n_2^2}, \tag{3.2}$$

with λ being the wavelength and n_1 (n_2) the core (cladding) index of refraction. For $V < 2.405$, only one mode is guided, called the fundamental mode, since the corresponding field distribution is always a solution of the wave equation. Setting up the frequency comb system, only single-mode fibers are used for the signal light. This is prerequisite for a stable, pulsed operation of the laser and well-defined beams after the output of the amplifiers. Multimode fibers are employed only for special applications, e.g. for guiding the pump light in double-clad amplifiers or for coupling the signal light to the spectrograph.

Taking into account that the electric field can be polarized in two states, a truly cylindrical symmetric, single-mode fiber supports two degenerate polarization modes. Any asymmetry in the fiber — derived from irregularities in the core shape or size, impurities or macroscopic bending — will lift the degeneracy and thus a standard fiber will mix the input polarization unpredictably. The output polarization will vary, depending on changes of the fiber's ambient conditions. This effect can be circumvented by intentionally breaking the cylindrical symmetry e.g. with the insertion of stress-inducing elements. The use of such a polarization-maintaining (PM) fiber is beneficial for driving polarization-dependent processes like frequency conversions after the output.

3.2.2   Mode-locking of a laser

Generating ultrashort pulses in the sub-ps regime is only possible by mode-locking the laser. This expression derives again from a picture in the frequency domain: For a number of modes to form a pulse train rather than a stochastic intensity fluctuation, their phases must be locked, i.e. they must have a fixed relation. Only then can the modes interfere constructively during a short period of time and destructively at any other time. The modes derive originally from the longitudinal modes of the laser cavity. The cavity modes are, however, not equidistant, but due to the dispersion in the various intracavity elements, the spacing is wavelength dependent. For a regular pulse train with perfectly equidistant modes to form, the cavity modes must be "pulled" onto a regular grid. Each mode can be understood as being modulated with the repetition rate, leading to modulation side bands. These side bands injection lock the neighboring modes and pull them onto the equidistant grid corresponding to the regular pulse train [134]. The mechanism, leading to mode-locking, however, is best described by looking at the time-domain picture and analyzing the pulse formation process.

Mode-locking can be accomplished actively, passively or in a hybrid combination. Active coupling is usually achieved either with a modulator that is externally driven and enforces pulsed operation or with synchronous pumping, which modulates the gain itself. Only passive techniques, however, are fast enough to enable the formation of pulses shorter than a picosecond. Passive mode-locking is generally accomplished by a saturable absorber, i.e. an element whose absorption decreases when the incident light intensity exceeds a threshold value. Therefore, an initial intensity fluctuation that is strong enough to start saturating this absorption experiences less loss and will be amplified in further cavity round-trips. A pulse will form and shorten with every passage through the absorber, because the pulse center has the highest intensity and lowest loss. If a relaxation time constant is associated with the saturable absorption, this can limit the pulse shaping effect and therefore the obtainable pulse duration (e.g. with semiconductor saturable absorber mirrors (SESAMs), which are often used to mode-lock fiber lasers.) Alternatively, the Kerr nonlinearity of a medium, i.e. its intensity dependent index of refraction $n = n(I)$, can be used to act as a virtual saturable absorber. Since the Kerr response is of electronic origin, its time constant is below the femtosecond level for all mediums and will not limit the minimum pulse duration. The theoretical limit of the pulse width is then given by the spectral bandwidth of the pulse. While this should intuitively be limited by the gain bandwidth of the laser material, it can be extended by exploiting additional intra-cavity spectral broadening. In this way, pulses shorter than two optical cycles can be generated directly from an Ti:Sa oscillator [121]. In fiber lasers spectra broader than the gain bandwidth can be generated too. These spectra can even contain frequency components with wavelengths shorter than the pump light.

To mode-lock crystal-based lasers — such as Ti:Sa lasers — the self-focusing effect of the Kerr nonlinearity is exploited, leading to Kerr-lens mode-locking (KLM) [23]. These lasers are a reliable tool to generate sub-100 fs, which paved the way for broadband frequency combs. The principle of KLM is well described in standard literature (e.g. [118]) and will not be explained in further detail, as this work focuses on fs-fiber lasers. To passively mode-lock a fiber laser, three concepts have been successfully demonstrated.

Nonlinear polarization evolution   The preferred method, employed in all lasers developed in this project, is to set up a ring cavity and exploit self-phase modulation (SPM) and cross-phase modulation (XPM) between the polarization modes for mode-locking. This so-called nonlinear polarization evolution (NPE) also relies on the fast electronic Kerr effect. NPE mode-locking was first demonstrated in an Nd-doped fiber laser [122]. Even during this earlier work, pulse durations as short as 70 fs with a Fourier limit of only 20 fs could be obtained. In figure 3.2 the basic principle of NPE mode-locking is depicted. As discussed above, any non-PM fiber is randomly birefringent, i.e. the two polarization axes are non-degenerate along its length, which leads to an intensity-independent phase shift. At every position within the fiber, the two polarization components of the light experience SPM and XPM, resulting in an additional, nonlinearly accumulated phase. In other words, the birefringence is modulated and the polarization of the light is rotated, to a degree dependent on the intensity. This is exploited to construct a virtual saturable absorber by defining the input polarization and putting an analyzing polarizer after the output of the fiber. The axes of the analyzer can be set such that high intensities — having a different polarization — are preferred over low intensities. Exceeding a threshold intensity, namely the onset of nonlinear effects, the light experiences less loss, giving a pulse-shaping mechanism. Minimum pulse durations of less than 30 fs have been demonstrated [123] with this technique, and during this work, repetition rates exceeding 500 MHz could be achieved [111].

Semiconductor saturable absorbers   Another possibility to mode-lock a fiber laser is to implement fast semiconductor saturable absorbers with relaxation times below 1 ps. They can be used in transmission or reflection inside a ring cavity or as an end mirror in a linear cavity. When this project began, only repetition rates comparable with those obtained with NPE lasers had been achieved with this method. Additionally, no pulses with durations below 150 fs had been demonstrated. This appeared especially problematic considering that no laser could be phase stabilized until then with spectra significantly smaller than 13 THz (see section 3.4). At that time, it thus seemed futile to further investigate this technique for mode-locking. Since then, repetition rates up to 1 GHz have been demonstrated using linear cavities [109]. By broadening the spectrum moderately before coupling the light into the PCF, this laser could also be phase-stabilized. If the obtainable pulse duration
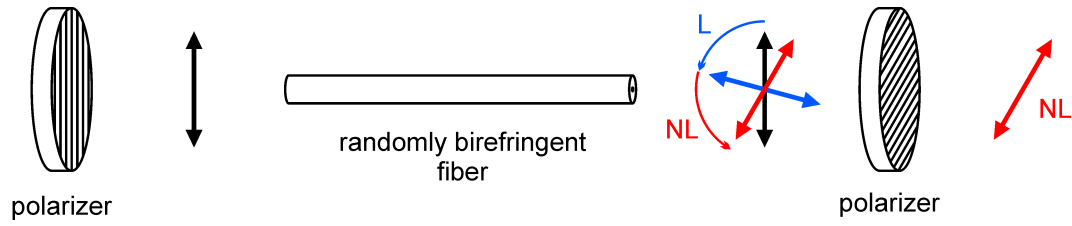
Figure 3.2: *Principle of mode-locking via nonlinear polarization evolution. In an anisotropic medium, a defined input polarization experiences a linear (L) phase shift (blue) and an additional nonlinear (NL) shift (red). The analyzer can be set such that high intensities, which experience a stronger nonlinear phase shift, are preferred. The polarization at the output is in general elliptical but can be made linear with a combination of a quarter and half wave plate (not depicted).*

of 150 fs can be further reduced to facilitate the required nonlinear frequency conversion processes, a linear fiber cavity with a high repetition rate can be considered as an alternative as a comb generator.

Nonlinear amplifying loop mirror   A second alternative to NPE is the use of a nonlinear amplifying loop mirror [124, 125]. A loop is set up after a 50:50 fiber splitter (consisting of two input and two output ports) with a section of gain fiber spliced asymmetrically in the loop. Light is propagating in both directions through the loop but will accumulate different nonlinear phase shifts, depending on whether it passes the amplifying section at the beginning or the end of the loop. At the coupler, the light from both directions is recombined and will interfere. Depending on the accumulated phases, it is either coupled back into the original input port or the other. As the phases are power-dependent, a virtual saturable absorber can be realized, leading to ultra-short pulse-formation. A cavity is formed by closing a second loop between the two input ports of the splitter and inserting an isolator and an output coupler into the second loop. For obvious reasons, this two-loop configuration is called a figure-8 laser. Thus far, however, no pulse durations significantly smaller than 100 fs have been demonstrated with this setup, and this laser is unsuitable when aiming for high repetition rates. A fiber section for the nonlinear phase shift is needed in addition to the gain fiber, which inhibits the design of short cavities.

3.2.3   Oscillator cavity dispersion

Fiber dispersion   Having only a potentially large spectral bandwidth and a fast pulse shaping mechanism is not the only prerequisite for obtaining short pulses. As mentioned above, intra-cavity dispersion prevents the cavity modes from coinciding with the modes of an equidistant pulse train. The nonlinear pulse shaping mechanisms are responsible for phase shifts, too, adding to the phases acquired due to propagation in the dispersive intra-cavity media. Consequently, only if the disper-

sion is in a regime that it can be compensated by the nonlinear phase shifts, will mode-locking occur.

Generally speaking, dispersion refers to the dependency of the refractive index on frequency $n = n(\omega)$. Its effect on pulse propagation can be easily seen by looking at the Taylor expansion of the propagation constant:

$$\beta(\omega) = \omega \frac{n(\omega)}{c} = \beta(\omega_c) + \left(\frac{\partial \beta}{\partial \omega}\right)_{\omega_c} (\omega - \omega_c) + \frac{1}{2} \left(\frac{\partial^2 \beta}{\partial \omega^2}\right)_{\omega_c} (\omega - \omega_c)^2 + \ldots, \quad (3.3)$$

with ω_c being the center frequency of the wavelength range of interest.

For practical purposes the constant and linear term of this expansion are of no concern, since the constant term is only the definition of a reference phase, while the linear term $\partial \beta / \partial \omega = 1/v_g$ is the definition of the inverse group velocity in the medium that leads to a constant delay of all pulses. Only the nonlinear terms will lead to a deformation of the pulse. The second order term is called group velocity dispersion (GVD)

$$\beta_2 = \left(\frac{\partial^2 \beta}{\partial \omega^2}\right)_{\omega_c} = \left(\frac{\partial}{\partial \omega}\right)_{\omega_c} \frac{1}{v_g} = \frac{1}{c} \left(2\frac{\partial n}{\partial \omega} + \omega \frac{\partial^2 n}{\partial \omega^2}\right)_{\omega_c}. \quad (3.4)$$

In ultrafast optics dispersion usually refers to GVD, which will also be the case during the rest of this work. GVD is always a property of a medium and refers to the dispersion per unit length. When quoting the dispersion of a component, such as a cavity or pulse compressor, the group delay dispersion (GDD) is given, being the derivative of the group delay τ_g or the second derivative of the spectral phase ϕ with frequency, respectively:

$$\text{GDD} = \left(\frac{\partial \tau_g}{\partial \omega}\right)_{\omega_c} = \left(\frac{\partial^2 \phi}{\partial \omega^2}\right)_{\omega_c}. \quad (3.5)$$

In fused silica, the GVD is positive for wavelengths smaller than $1.27 \, \mu$m (see figure 3.3), i.e. higher frequencies travel slower than lower frequencies and a pulse becomes "up-chirped". SPM will act on a pulse in the same way, because the second order nonlinear refractive index n_2 is mostly positive far from resonance [118]. Consequently, in this wavelength regime there is no chance that material dispersion and nonlinearity will cancel each other out and an initially short pulse will inevitably broaden. Additional measures must be taken to introduce negative GVD in the cavity in order to recompress the pulses and achieve a steady state of the oscillation. There are a large number of pulse compression techniques, including grating pairs [127] and prism pairs [128] or a combination of the two [129], chirped mirrors [130], microstructured fibers [131], higher order spatial modes in fibers [132] and chirped fiber Bragg gratings [133]. For the fiber laser system developed in this work, a grating compressor is used in the oscillator and subsequently a hybrid
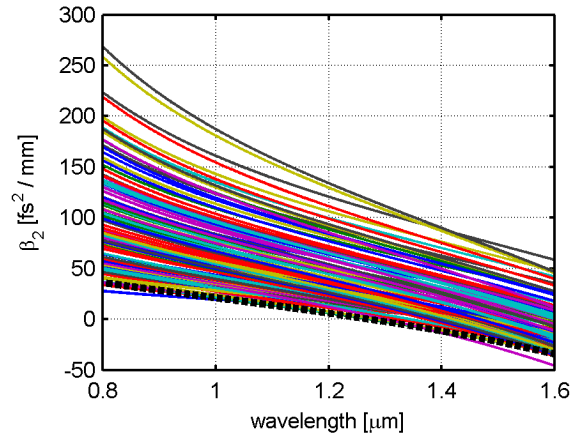
Figure 3.3: *Variation of the GVD with wavelength of all glasses contained in the Schott catalog [126], computed from their Sellmeier coefficients. Fused silica (black dashed line) has the smallest zero dispersion wavelength ($\lambda_{zd} \approx 1.27\,\mu m$).*

grating and prism compressor after the amplifiers. Their principles are described in appendix B.

If GVD and SPM are compensated by a compressor, higher order dispersion must be considered and can limit the obtainable pulse duration. A small mismatch that remains between the cavity's modes and the modes of the pulse train can be tolerated. It will be compensated by the mode-pulling effect. Only when the cavity dispersion is too large and the modes need to be pulled too far will the spectral bandwidth suffer or mode-locking cease to work.

Dispersion compensation   The GVD parameter β_2 of a fiber is determined by the material dispersion of the glass in core and cladding, to which the contribution of the so-called waveguide dispersion is added. To guide the light in a fiber the index of refraction is slightly lower in the cladding where the evanescent part of the electric field is non-vanishing. The effective index of the mode is thus lowered. This reduction is frequency-dependent, since the evanescent part of the mode grows with increasing wavelength. The resulting waveguide dispersion is therefore always positive. This is an important design parameter of fibers, since it can be influenced by the shape of the core region and the type of the glasses. For wavelength regions where the GVD of the material is negative, waveguide dispersion can be used for compensation, and the zero-dispersion wavelength can be designed as desired. In this way, the accumulated net-dispersion in an oscillator can be chosen by the proper combination of different fibers with adequate lengths. Er-doped fiber lasers, for example, have been successfully operated in an all-fiber setup with all of the three above-mentioned cavity-designs and in all dispersion regimes explained below.

At wavelengths below 1270 nm, however, all standard glasses have a positive

GVD. In this case, it is therefore not possible to use combinations of standard fibers to construct a dispersion compensated cavity. The simplest and preferred solution is then to use a pulse compressor made from bulk components in a free-space section of the cavity. While an all-fiber laser is certainly beneficial for a mechanically robust setup, an intracavity free-space section offers some practical advantages, too. Bulk optics consume less optical path length than comparable, commercial fiber components, enabling higher repetition rates. In a free-space section, a retroreflector, mounted on a translation stage, is also easily implemented, which is useful for tuning the repetition rate over large ranges (several MHz).

Standard fibers for light, with a wavelength around $1000\,\mathrm{nm}$, have a GVD of $\beta_2 \approx 23\,\mathrm{fs^2/mm}$. When using fiber lengths of about $1\,\mathrm{m}$, the accumulated chirp amounts to more than ten thousand $\mathrm{fs^2}$. Prism compressors, which are typically used in crystal-based lasers, cannot provide this much GDD with reasonable prism separations. Hence, grating compressors are normally employed in fiber lasers. Their GDD can be easily calculated (see appendix B.1), and with a groove density of $600\,\mathrm{lines/mm}$ and a separation of $2\,\mathrm{cm}$ it already amounts to more than $25{,}000\,\mathrm{fs^2}$. The exact value still depends on the angle of incidence.

Dispersion compensation is not only necessary inside the laser cavity, but also after propagation through subsequent fibers, e.g. amplifiers. Intracavity, a compensation of only the GDD is sufficient for defining the dispersion regime and thus the laser's state of operation. Higher order dispersion is compensated by mode-pulling. If, however, the pulses shall be compressed to their bandwidth limit outside the cavity, a higher order chirp can severely limit the minimum obtainable pulse duration once the (GVD-induced) linear chirp is compensated for. Unfortunately, the third-order dispersion (TOD) of standard fibers and of a grating compressor are both positive, and the quadratic chirp induced by both will add up. When using tens of meters of fiber, this effect is so strong that it cannot be ignored. With a hybrid grating/prism compressor, described in detail in appendix B.2, it is possible to independently tune its GDD and TOD such that both the linear and quadratic chirp of a pulse can be removed.

Dispersion regimes   For a laser to emit a regular pulse train, the pulse shape must be a self-reproducing solution of the wave equation. After each round-trip, the pulse must be identical to the initial one. For the simple propagation in a fiber, the wave equation (3.1) can be rewritten as a nonlinear Schrödinger equation (NLS) (see [119]). It can take several forms depending on which nonlinear effects are included and to which order the dispersion is approximated (see equation (3.16)). In any case, the NLS has solitonic solutions, i.e. field distributions that travel through space without changing their shape or that at least reproduce themselves periodically. For negative GVD, the soliton assumes a pulse-like shape with a $\mathrm{sech^2}$-envelope. The tendency of a pulse to broaden due to dispersion is canceled by the nonlinear effects, such as SPM. A solitonic solution is stable, i.e. a small distortion will heal during

propagation and an initially non-solitonic pulse will evolve into one, if it is close enough to the steady-state solution.

In a laser cavity, additional pulse shaping mechanisms, such as gain, saturable loss, spectral filtering, birefringence and the extraction of the signal, must be considered [135]. Depending on the GDD of the cavity, averaged over one round-trip, the pulse evolution differs. For both positive and negative values, however, mode-locked operation has been demonstrated. The following list gives an overview of the three distinctive dispersion regimes in which pulse formation is described by different mechanisms. For exemplary spectra see section 3.3, figure 3.5.

$\text{GDD} \ll 0$ In a net-anomalous fiber cavity, the pulse's evolution is solitonic and both its spectra and pulse envelope have a sech^2-shape. A periodic amplitude modulation in the laser, due to the gain and loss dynamics, leads to the typical Kelly-sidebands [136] in the spectrum. Pulse energy, duration and spectral bandwidth are uniquely coupled [119], and thus, the minimum achievable pulse width is limited. For shorter pulses, the pulse energy would need to be increased, leading to the formation of higher-order solitons and pulse break-up. Compared with the other dispersion regimes, the threshold for self-starting mode-locking is the lowest in the solitonic regime.

$\text{GDD} \approx 0$ In the dispersion-managed regime, the pulses evolve in a stretched pulse mode. The cavity typically consists of a section with normal and anomalous GDD, and thus, the pulses are breathing during one round-trip [137] (hence the name stretched-pulse). This allows for wider spectra and shorter pulses when extracting the pulses after the normal-dispersive section, where soliton shaping is minimized. It is possible to design the cavity such that the pulses have their minimum duration within the fiber section. In this case, the spectra are additionally broadened via SPM. The shortest pulses from fiber lasers are obtained with this configuration [123]. Higher pulse energies can be achieved with respect to the solitonic regime but at the cost of increased susceptibility to pulse break-up and multipulsed operation. Careful design of the arrangement of the gain-fiber within the cavity is necessary to avoid these problems.

$\text{GDD} \gg 0$ Even in the positive dispersion regimes, mode-locking is observed, although both dispersion and nonlinearity chirp the pulse in the same direction. The pulse-shaping element in these all-normal-dispersion lasers is a temporal filter. In the fiber, the pulse becomes highly chirped with the pulse wings containing the spectral wings. A spectral filter, clipping the spectral wings, can then act as a temporal filter and shorten the pulse duration [138]. Alternatively, the

NPE mechanism can be the temporal filter. The resulting spectrum is parabolic [139] for small accumulated nonlinear phase shifts and will develop sharp peaks at the edges for larger nonlinear phase shifts [138]. The pulses are highly chirped within the cavity, allowing for the extraction of high pulse energies directly from the oscillator without pulse break-up. The threshold for mode-locking is increased as well.

3.3　Yb-fiber oscillators

3.3.1　Medium repetition rate oscillator

According to the considerations above, a Yb-fiber laser was set up (see figure 3.4). It consists of a ring cavity with a free-space section, mode-locked via NPE. The pump source is a laser diode, pigtailed to a single-mode fiber and delivering up to 600 mW optical power at 974 nm, which is coupled into the fiber ring via a wavelength division multiplexer (WDM). The gain fiber is a 25 cm long, highly doped Yb-fiber with a nominal absorption of 2000 dB/m at 975 nm. Every other fiber length is kept to a minimum that is determined by the available fusion splicer, which requires a distance of more than 6 cm between the splice and a component. The total fiber length amounts to ~ 55 cm.

All free-space components, including the pigtailed collimators, are anti-reflection coated for $1000-1100$ nm, since small back-reflections inhibit the initiation of mode-locking very efficiently. The length of the free-space section amounts to ~ 35 cm, resulting in a repetition rate of 250 MHz. The signal is coupled out of the cavity at the polarizing beam splitter, which is also used as the analyzer for NPE mode-locking. No fixed output coupling ratio can be quoted, but, depending on the state in which the laser is operated, 50-90 % of the intracavity power is extracted.

The grating compressor consists of a pair of two reflection gratings with a groove density of 600 lines/mm and an incidence angle of $\sim 30°$. The retroreflector in the grating compressor is glued onto a piezo actuator. By applying a voltage to the piezo, the cavity length can be tuned. This is important to enable control of the repetition rate as discussed in the next section. Long-term drifts that would exceed the small travel range of the piezo (only 5 μm) are countered by a translation stage, on which the same mirror is mounted. 1 cm travel range enables a shift in repetition rate of 4 MHz.

Self-starting mode-locking can be obtained in all three dispersion regimes, depending on the grating separation of the compressor. The corresponding spectra are depicted in figure 3.5. In the solitonic regime, stable operation is achieved with a pump power of 300 mW and a laser emission of 100 mW. With increasing GDD, the mode-locking threshold increases as well. At a GDD of $+5600 \, \mathrm{fs}^2$ the maximum pump power of 600 mW is needed and the laser emits 230 mW.
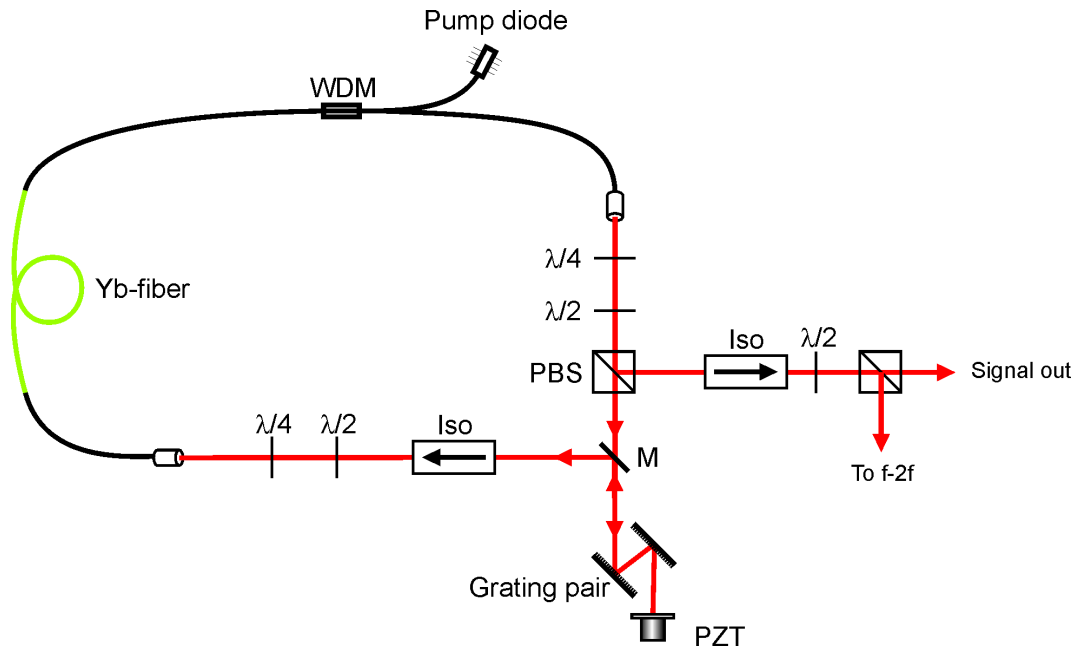
Figure 3.4: *Schematic of the oscillator setup. At the retroreflector of the grating compressor, the beam is vertically tilted to be separated from the incoming beam at the mirror M. WDM: wavelength division multiplexer, Iso: isolator, PBS: polarizing beam splitter, PZT: piezo actuator.*

It is difficult to exactly determine the GDD of the cavity, since the exact value of the fiber GVD — especially of the doped fiber — is unknown. Measuring the dispersion of doped fiber is not only difficult, due to its high absorption in the wavelength regime of interest, but also ambiguous, since it varies with the population inversion. The broadest spectrum, corresponding to the dispersion-managed regime, is therefore assumed to be generated in a cavity with vanishing GDD. For larger grating separations and negative GDD, solitonic pulses are emitted. These pulses show the characteristic narrow spectra with Kelly sidebands. All-normal dispersive operation is observed as well, and the steep edges of the spectrum indicate a high nonlinear phase shift.

An important characteristic of the laser is the linewidth of its individual modes. When increasing the mode spacing with filter cavities, a finite linewidth can possibly lead to a shift of the spectral envelope (see section 3.8). A heterodyne beat measurement of the oscillator with a narrow linewidth continuous wave (cw) laser is thus performed. The comb is fully phase-locked in repetition rate and offset frequency for this measurement and the cw laser is free running. As expected for a fiber laser, a linewidth of $\lesssim 1\,\mathrm{MHz}$ is observed for all modes within the oscillator's fundamental spectrum (see figure 3.6). This linewidth is sufficiently narrow that any impact on the calibration is negligible within the frame of this work. When aiming for an absolute calibration on the cm/s-scale, however, it might be necessary
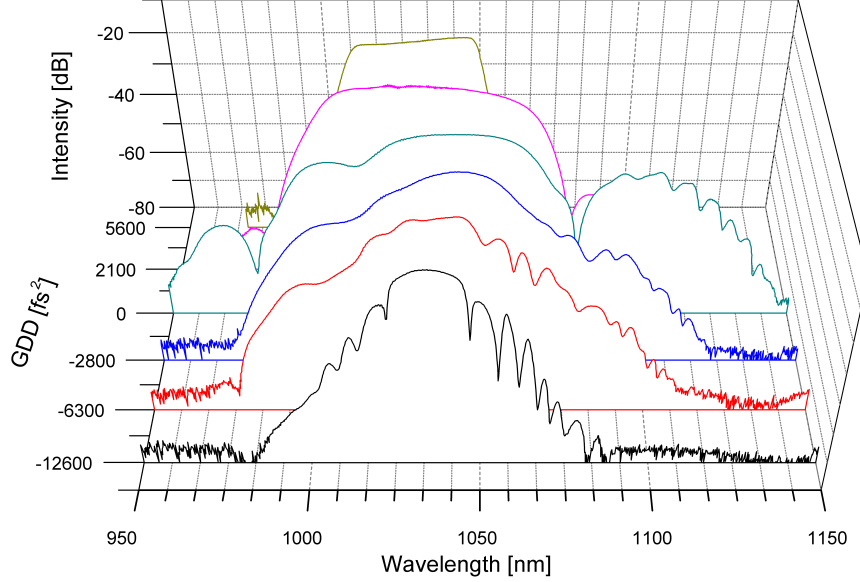
Figure 3.5*: Variation of the laser spectra with the GDD of the 250 MHz cavity. Solitonic, stretched pulse and all-normal dispersive pulse evolution are observed. The spectral holes at 980 and 1080 nm are caused by the WDM which is designed to split 980 from 1030 nm and thus splits 1080 from 1030 nm as well. Note, that the GDD axis is non-linear and prone to an unknown, constant bias, because the zero point is not calculated but chosen from the broadest spectrum (see text). The quoted differences in GDD are exact, since they are computed from the change in compressor grating separation.*
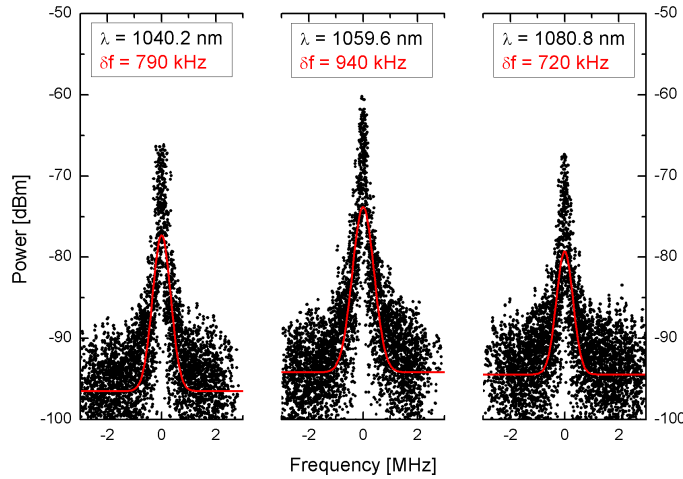

Figure 3.6*: FWHM linewidth δf of the comb modes at three wavelengths λ. The comb is phase-locked in repetition rate and offset frequency to a hydrogen maser, while the cw laser is free-running. The resolution bandwidth is 51 kHz and the sweep time 2 ms. The linewidth of the cw laser for the beat measurement is specified with 100 kHz and can be neglected along with drifts of the laser within the short sweep time.*

to reduce the linewidth by an order of magnitude. In this case, the residual noise on repetition rate and offset frequency will need to be suppressed.

Since the stability of laser cavities exceeds that of the best RF sources on time scales shorter than 1 ms, only other optical references can be employed to further reduce repetition rate noise, when thermal and acoustic noise are removed. High-finesse cavities, made from ultra-low expansion glass, can be employed to achieve sub-Hz linewidths of cw lasers [98]. Locking a frequency comb to such a cavity instead of an RF reference transfers the stability of the cw laser to the comb, resulting in the desired reduction in comb mode linewidth.

On the other hand, the direct reference to the atomic clock is lost and must be recovered by monitoring the comb's frequencies. Residual noise on the offset frequency can be reduced by increasing the servo bandwidth, e.g. by employing a phase advance circuit in the feedback loop [140]. Since the offset frequency is controlled via the pump current, the lifetime of the upper state of the laser transition acts as a low-pass filter and limits the servo bandwidth. By counteracting this low-pass behavior with a carefully designed high-pass filter, the bandwidth can be extended, and a significant reduction of the offset beat noise can be achieved.

A laser with an improved mechanical setup in a industrial-grade, rugged housing has been developed based on the oscillator design presented in this chapter. This laser is temperature stabilized and fully computer-controlled, allowing it to run continuously over months with both repetition rate and offset frequency phase-locked to an external reference.

3.3.2 High repetition rate oscillator

In an attempt to increase the repetition rate of the laser, all fiber lengths have been reduced to a minimum. I.e. the oscillator only contains gain fiber and the fiber pump coupler as well as the pigtailed collimators are replaced by free space components. The pump light is superimposed with the signal light on a dichroic mirror with a sharp spectral edge at 1000 nm. Connectors are glued to both ends of the gain fiber, and the glass facets are polished at an angle of 8° to avoid back-reflections. The light is coupled into the bare fiber ends via aspheric lenses. Optimizing the mode-matching of both pump and signal beam is tricky, since both beams are coupled to one fiber end with the same lens. An iterative process in which the pump and signal beams are alternatingly aligning proved to be successful.

The gain fiber is shortened to ~ 15 cm, at which point the bending of the fiber becomes critical for the laser's ability to mode-lock. Only for distinctive fiber bendings can waveplate settings be found at which the laser starts pulsing. Mode-locking will cease to start from noise when the nonlinear phase shift accumulated during one round-trip is insufficient. Shortening the cavity length decreases the nonlinear effects in several ways. First, increasing the repetition rate while keeping the same pump power and thus the maximum average signal power constant will lead to a
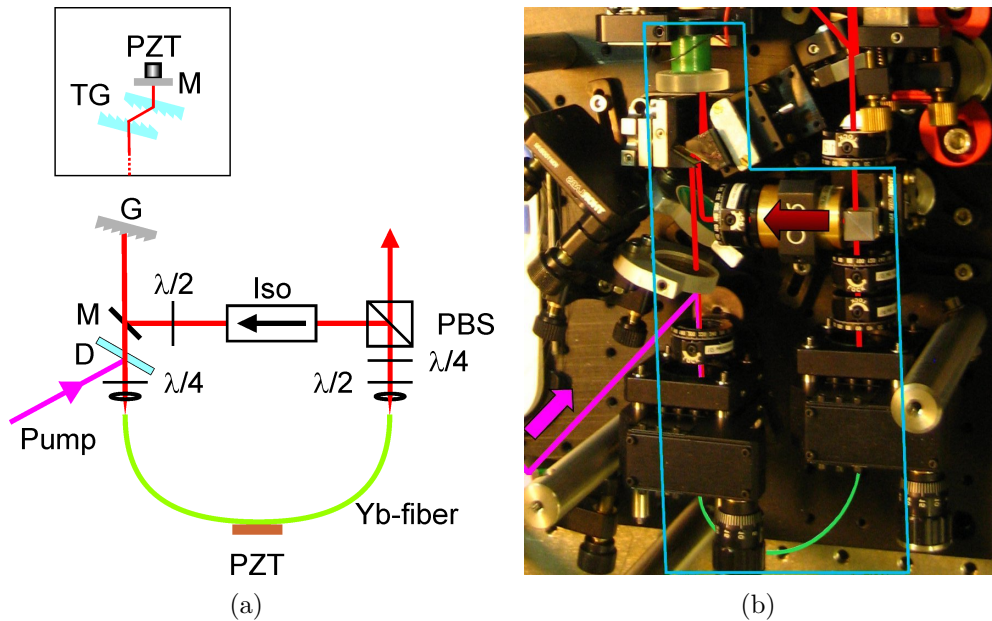
Figure 3.7: *(a) Design of the high repetition rate ring cavity. Either a pair of transmission gratings (TG) is used for dispersion compensation or a single reflective grating (G) acts as additional spectral filter. In the latter case, the piezo actuator (PZT) for repetition rate control is glued directly to the fiber. The pump light is coupled to the fiber via a dichroic mirror (D). Further abbreviations as above. (b) Photograph of the setup with the pump light path in purple, the signal path in red, the gain fiber in green and the components belonging to the oscillator within the blue box.*

decreased pulse energy. Provided that the pulse length does not shorten, the peak intensity and thus the nonlinear effects will decrease. Second, the accumulated non-linear phase shift is directly dependent on the fiber length. Third, the shorter the gain fiber, the less pump power will be absorbed and thus the more the available signal power will decrease. To enable mode-locking despite these difficulties, two laser diodes, each delivering up to 750 mW, are combined in crossed polarizations to provide a maximum pump power of 1.5 W at 974 nm.

In addition to the solitonic pulse-shaping in a dispersion compensated cavity, an all-normal dispersive cavity without intracavity compressor has been set up. Instead, a spectral filter is inserted to assist mode-locking. Both configurations are depicted in figure 3.7.

Dispersion compensated setup   In the dispersion-compensated setup, a pair of transmission gratings with 1000 lines/mm is employed. Using a high grove density enables a small separation, and transmission gratings are favorable to avoid clipping of the beam. The diffraction efficiency of the specially designed gratings exceeds 93 %, minimizing the intracavity losses. The free-space section is shortened to $\sim$
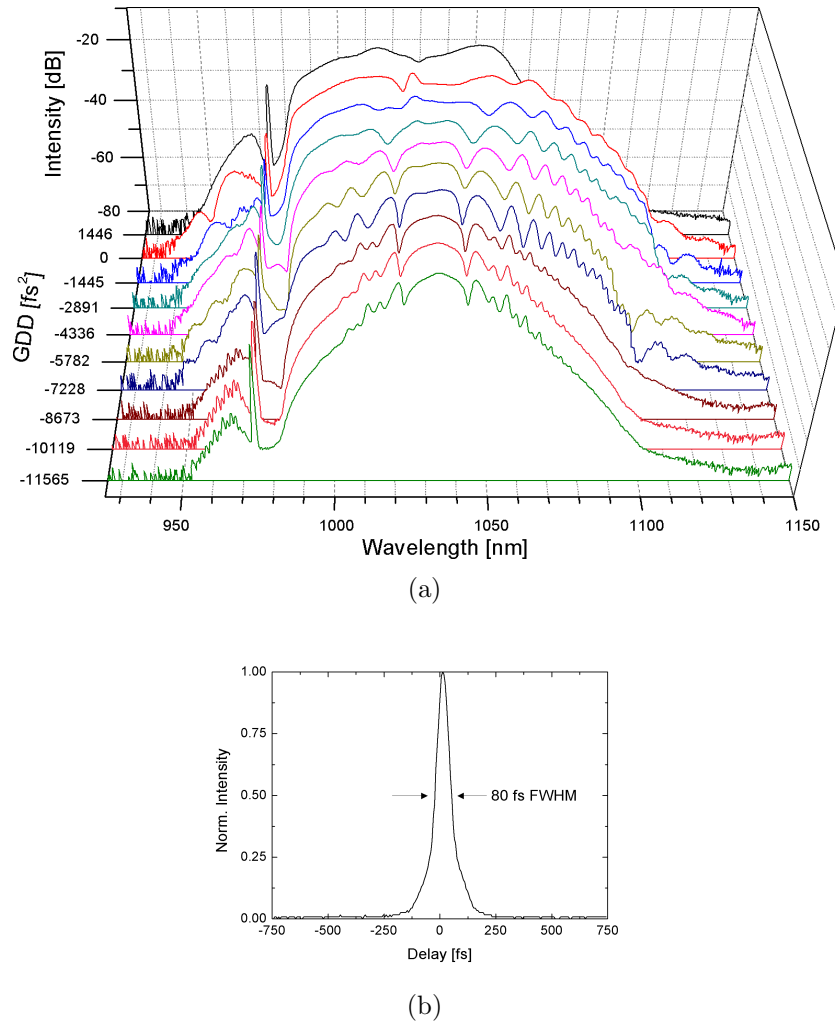
(a)

(b)

Figure 3.8*: (a) Variation of the laser spectra with the GDD of the 550 MHz cavity. Solitonic and stretched pulse operation could be obtained. The broadest spectrum is attributed to vanishing GDD. (b) Minimum obtained pulse duration. The pulses with the broadest spectrum are compressed in an external grating compressor and measured with an autocorrelator.*

30 cm, which results in a repetition rate of $\sim 550\,\text{MHz}$. Self-starting mode-locking is observed in the solitonic and dispersion managed regime at pump powers above $1\,\text{W}$ (see figure 3.8), resulting in an output power of $\sim 500\,\text{mW}$. No multipulsing is observed in the range of available pump powers. Having a maximum spectral bandwidth of $70\,\text{nm}$ FWHM, the pulses can be externally compressed to a pulse duration of only $60\,\text{fs}$. Despite bearing a greater resemblance to a free-space crystal-based laser, this oscillator maintains the key feature of a fiber laser, namely its robust mode-locking behavior. This laser can run for weeks without realignment

and starts immediately in the previous mode-locked state after being switched off for some time.

While this laser was already available for the calibration campaign of the HARPS spectrograph in 2010 (see section 5.2), a commercialized version of the 250 MHz system was used instead. For the calibration tests, the benefits of a computer-controlled laser in an industrial-grade housing outweighed those of one with an increased fundamental mode spacing. In the future, however, using a commercialized 500 MHz system would significantly relax the requirements for the following Fabry-Pérot cavities.

All-normal dispersive setup In the previous design of the high-repetition rate fiber laser, mode-locking could not be obtained in the all-normal dispersive regime due to insufficient pump power. In general, pulse shaping in this regime is dominated by a spectral filter, clipping the wings of the spectrum and thereby shortening the pulse. Only one explicit filter is present in the dispersion-compensated setup: the dichroic mirror. Its spectral edge, however, is designed to be as far away from the signal's center wavelength as possible, and for narrow spectra, it has a negligible effect. Pulse shaping via NPE is thus the only spectral filter in the oscillator, and with increasing chirp of the circulating pulse, its effect decreases until it is insufficient to sustain mode-locking.

An explicit, narrow-band spectral filter can thus be inserted in the cavity to assist mode-locking [141]. When using an interference filter at 1030 ± 5 nm, the grating compressor can be relinquished and the laser still mode-locks. However, the interferometric nature of the filter leaves a mark on the spectrum, as observed in earlier work [142]. Clean spectra without significant fine-structure are obtained when replacing the bandpass filter with a simple grating. The bandwidth of this type of filter is determined by the grating constant g and the distance between the grating and the fiber facet. Three different gratings have been used and the corresponding spectra of the laser are depicted in figure 3.9(a). The gratings with $g = 300$ lines/mm and $g = 600$ lines/mm are reflection gratings operated in Littrow configuration and replace the retroreflector from the previously used compressor. Their absolute efficiency is $\sim 80\%$. To reduce the intracavity losses, a transmission grating has been tested with $g = 1000$ lines/mm, which proved successful as the mode-locking threshold decreased despite having a very narrow spectrum and long pulses. Table 3.1 summarizes the pump powers required for stable operation, the corresponding output powers and the obtained spectral bandwidths. The repetition rate of ~ 550 MHz is comparable to the dispersion-compensated setup.

By employing the explicit spectral filter, not only the spectral bandwidth but also the center wavelength becomes an easily accessible design parameter. By simply tuning the incidence angle on the grating, the spectrum can be shifted. Within a large range from 1010 to 1060 nm, self-starting mode-locking is obtained (see figure 3.9(b)). The farther apart the filter is from the gain maximum (indicated

		Groove density		
	IF	300 l/mm	600 l/mm	1000 l/mm [a]
Pump power [W]	1.3	0.6	1.0	0.6
Output power [mW]	590	280	525	300
Bandwidth (FWHM) [nm]	12.8	6.7	2.7	0.3

[a]Transmission grating

Table 3.1: *Performance data of the all-normal dispersive 550 MHz oscillator with an interference filter (IF) and three different gratings.*

by the broad peak of the amplified spontaneous emission (ASE)), the narrower the parameter range for the waveplate settings to achieve mode-locking is. Eventually, mode-locking is no longer obtainable and ASE becomes dominant.

Due to the pulse-shaping mechanisms, the pulses circulating in the resonator are highly chirped in spite of the short cavity length. According to the compressor separation for stretched pulse operation, the single pass GDD of the cavity is only about $15.000\,\mathrm{fs}^2$. A FWHM of 1.6 ps of the autocorrelation peak is measured directly after the output when using the $g = 600\,\mathrm{lines/mm}$ grating with a bandwidth limit of only 790 fs. Assuming a linear chirp, a GDD of $\sim -200.000\,\mathrm{fs}^2$ is needed to compress the pulses, which is confirmed by setting up an external grating compressor accordingly. Pulse durations within 5 % of the bandwidth limit are obtained with an autocorrelation width of 840 fs (see figure 3.9(c)).

With these narrow bandwidths and long pulse durations, the laser is clearly unsuited to serve as a frequency comb generator. This, however, was not the motivation for studying this narrow-band, tunable oscillator in detail. It is an ideal pump source for an Yb:YAG Innoslab amplifier, which has a gain bandwidth of only 1.9 nm at a central wavelength of 1029.8 nm. The oscillator can be tuned to exactly match these parameters. In a cooperation with the Fraunhofer Institute for Laser Technology, this oscillator was tested and could be amplified to 375 W average power without further customization of the amplifier [143]. At MPQ, the oscillator is used to couple the amplified light to a high-finesse enhancement cavity ($\mathcal{F} \approx 1000$) such that high harmonics would be generated in a gas jet. For this application, the repetition rate of the laser needs to be locked to the cavity length with a high servo bandwidth. Lacking a small retroreflector in the cavity, the piezo actuator is glued directly to the fiber cladding. Stable locking can be achieved with a sufficiently high servo bandwidth.

Taking even more care to shrink the setup and using an even shorter gain fiber with a length of only 12 cm, the repetition rate has been further increased to above 670 MHz, as shown in figure 3.9(d). Here, a $g = 600\,\mathrm{lines/mm}$ grating is employed, and pump powers of 1.1 W are necessary for stable, mode-locked operation. Since a margin in pump power still exists, setting up an oscillator with an even higher
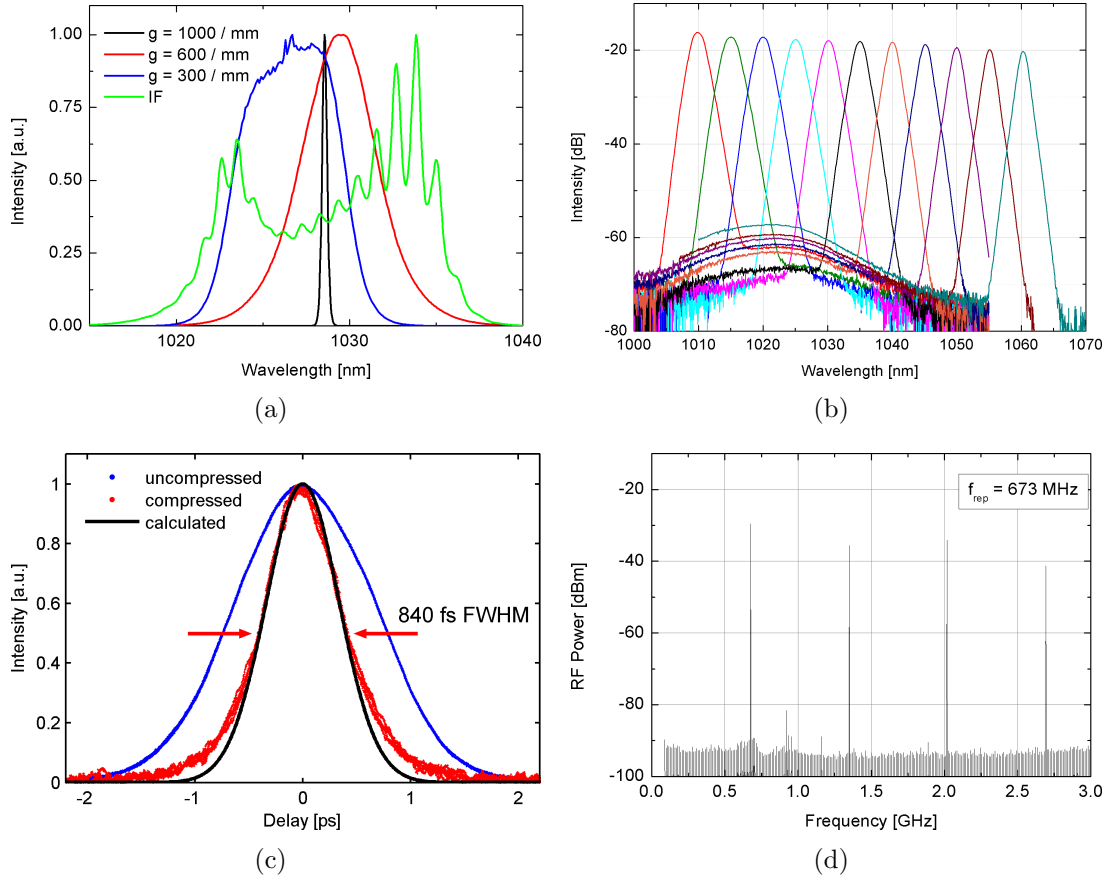
Figure 3.9: *(a) Spectra of the high repetition rate oscillator. An interference filter (IF) or different gratings were used as explicit spectral filter to assist mode-locking. (b) Variation of the center wavelength of the spectrum with the grating angle (g = 600 lines/mm). (c) Minimum obtained pulse duration. The autocorrelation of the pulses directly after the oscillator (with the g = 600 lines/mm grating) and after an external compressor (having a GDD of −200.000 fs²) is compared with the bandwidth-limited autocorrelation computed from the spectrum. (d) Highest repetition rate obtained with this setup.*

repetition rate also seems feasible. To realize this, the previously used commercial optics mounts would have to be replaced by smaller, custom-made mounts. For the use as frequency comb generator, either a dispersion-compensated setup must be used or a broader spectral filter. In principle, 100 fs pulses can be obtained from an all-normal dispersion laser with an explicit intracavity filter [142]. In conclusion, further development of this oscillator shows great promise for achieving even higher fundamental repetition rates of fiber ring lasers.

3.4 Phase-stabilizing the comb

There are only few applications where a femtosecond oscillator with an unstabilized offset frequency can be used for precision measurements [144]. In most cases, however, a fully stabilized frequency comb is desired. This implies locking both the repetition rate and offset frequency to a local oscillator, which is either a radio frequency (e.g. an atomic clock or a reference oscillator) or an optical reference (e.g. a high-finesse cavity or an optical atomic clock). To perform this task, both frequencies must be detected and two parameters of the laser must be found that can be used control them independently. Consequently, a phase lock needs to be set up to force the target oscillation to follow the reference in phase without losing cycles.

3.4.1 Repetition rate stabilization

Detecting and stabilizing the repetition rate is straight forward. For detection, a fast photodiode suffices. All comb modes will beat with each other and the resulting electronic signal will be a comb in the radio frequency (RF) regime with the repetition rate as spacing and zero offset. Any of these RF modes can be compared with the local oscillator just by electronically mixing the two signals. It is, however, advantageous to take a higher harmonic of the repetition rate, as this will make the servo more sensitive to small excursions. The resulting beat can be used as an error signal for a servo loop acting on a piezo-mounted mirror in the cavity. Applying a voltage to the piezo will change the cavity length and thus repetition rate.

The servo bandwidth of this lock should not be chosen too large. The goal is to remove slow variations of the cavity length that are induced by acoustic noise and thermal drifts. The power spectrum of these noise sources contains frequency components up to about 1 kHz. Above this Fourier frequency, a laser cavity is typically less noisy than even the best RF reference [145] and consequently the noise of the reference will be transfered onto the comb. This would destroy the comb structure in the optical regime as the repetition rate is multiplied with the mode number n, which is on the order of 10^6, and the spectral density of phase noise added to the repetition rate is multiplied by n^2. The phase noise would be amplified by 120 dB, which would drown out the comb modes. This effect, termed "carrier collapse", is well known from electronics and was a key argument against the possibility of building a frequency comb [146]. The solution to this problem is hence to restrict the servo bandwidth to below 1 kHz and rely on the laser cavity as flywheel, using its intrinsic stability, for higher frequencies.

3.4.2 Offset frequency stabilization

Compared to the repetition rate, it is more complicated to detect the offset frequency and this is the main reason why frequency combs have not been developed earlier.
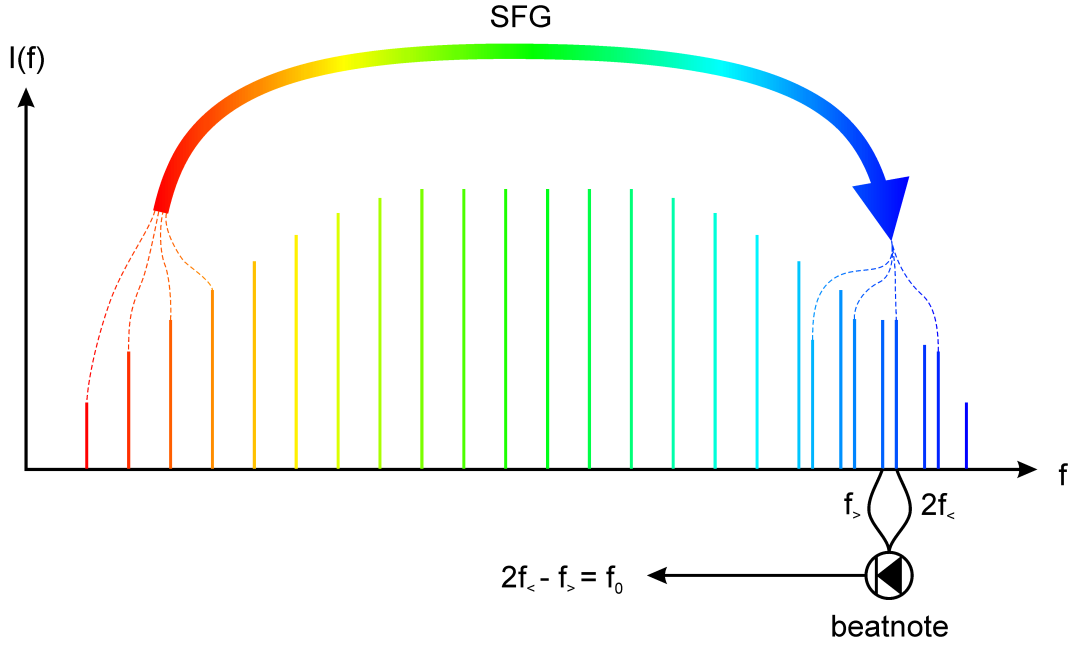
Figure 3.10: *Offset frequency detection. The low frequency part of the spectrum is converted to twice its frequency via sum frequency generation (SFG). By heterodyning with the modes of the high frequency part, the offset frequency can be obtained.*

In case the comb's spectrum spans an optical octave, however, there is an easy way of detecting the offset frequency. With an f-$2f$ interferometer, whose principle is depicted in figure 3.10, it can be observed as an RF beatnote.

The low frequency part of the spectrum $f_< = nf_r + f_0$ is frequency doubled via sum frequency generation. This will generate frequencies $2f_< = 2(nf_r + f_0)$, which spectrally overlap with the high frequency part of the original spectrum $f_> = 2nf_r + f_0$. When generating the beatnote between these two frequencies with a photodiode, the offset frequency is obtained:

$$2f_< - f_> = 2(nf_r + f_0) - 2nf_r + f_0 = f_0. \tag{3.6}$$

Note that in the sum frequency generation not only the doubled frequencies are generated but also combinations of the nth and $n+1$th mode, leading to a multiplied comb with $1 \times f_r$ spacing.

The question is thus: how can an octave spanning spectrum be obtained? There is no laser gain medium with an octave-spanning bandwidth and only Ti:Sa oscillators have so far been built with such a broad spectrum directly from the oscillator [147], which was only achieved after frequency combs were already demonstrated. The second key ingredient to the invention of the frequency comb — after having a Kerr-lens mode-locked Ti:Sa laser — was therefore the ability to use microstructured or photonic crystal fibers (PCF) to broaden the spectrum outside the

laser oscillator [24]. Due to the long interaction length and the strong confinement in the core, SPM and Raman processes can phase-coherently generate new frequencies over large bandwidths. In these fibers, the zero-dispersion wavelength can be tailored by varying the core diameter and the geometry of the air-filled structure surrounding it. This can be exploited to design fibers that show efficient spectral broadening and with their help, octave-spanning spectra can be generated with a variety of fs-lasers.

That spectral broadening is involved in the process of detecting the offset frequency gives a hint why sub-100 fs laser pulses are essential for frequency combs. In principle, all the mathematical arguments above are independent of the spectral bandwidth or the pulse duration, respectively. When using spectral broadening, however, the situation changes, as for example the Raman effect has its maximum gain in silica fibers approximately -13 THz from the pump frequency [119]. While it could not yet be proven, a plausible reasoning goes as follows. The Raman effect cannot generate coherent frequency components from noise, since it is a non-parametric process (see section 3.8). If, now, the input spectrum is too narrow, the Raman effect will predominantly amplify initially spontaneous photons. Coherent amplification, however, is possible if the input spectrum is wide enough, such that there are sufficient photons -13 THz from the central frequency to seed the Raman effect. To generate new frequency components which are coherent with the seed light, parametric effects such as four-wave mixing must be exploited. They are bound to energy conservation and maintain the equidistancy of the comb modes as well as their phase relation. Since both, parametric and non-parametric effects participate in the spectral broadening process, the seed spectrum should be sufficiently broad to inhibit the generation of incoherent spectral components. Which effect exactly is responsible for the degradation of the coherence still needs to be determined, but it has been experimentally verified that, when broadening too narrow of a seed spectrum (corresponding to bandwidth limited pulses of more than ~ 100 fs), the output spectrum might be very broad but no offset beat is observable because the comb structure has been destroyed [27].

After being able to detect the offset frequency, the next question is how can it be controlled. A hint is given by the realization that the offset frequency is related to the difference of phase and group velocity. In solitonic propagation, a change in the pulse energy does not affect the group velocity but has an impact on the pulse's phase [119]. A more realistic theory needs to consider higher order effects and an elaborate model is needed to explain the observed shifts [148]. Experimentally, modulating the pump power of the oscillator and thereby the pulse energy was shown to give good control over the offset frequency [149] soon after the first demonstration of a comb.

In contrast to the lock of the repetition rate, experience shows that large phase excursions of the offset frequency are likely to occur and the phase lock must have a large locking range. Using a frequency divider or a forward-backward counting

digital phase detector [150] is a prerequisite for reliably locking the offset phase to the reference. Since the offset frequency merely adds to the optical frequencies, noise multiplication is not an issue (in contrast to the stabilization of the repetition rate), and thus a high servo bandwidth can be employed.

This is beneficial for the combined performance of both phase locks, since they are not linearly independent. Changing the cavity length can act on the pulse energy, e.g. by beam pointing or because a higher repetition rate reduces the pulse energy at constant average power. Modulating the pump power will on the other hand change the dissipated energy in the cavity and via thermal expansion the repetition rate as well. Separating the locks in its servo bandwidth is thus helpful for stable operation.

3.4.3   Octave-spanning spectra

The output spectrum of the Yb-fiber oscillators presented in the previous section is at most 100 nm wide, if taking advantage of intracavity spectral broadening and considering also the wings of the spectrum. Since an octave-spanning spectrum is necessary for a convenient detection and stabilization of the comb's offset frequency, the oscillator spectrum must be broadened externally as well. Phase stabilization of the offset frequency had not yet been demonstrated with an Yb-fiber laser when this project was started and thus a nonlinear fiber had to be found that provided a suitable spectrum.

A series of different nonlinear fibers have been investigated. To provide sufficient power, a core-pumped amplifier is set up, that delivers 600 mW optical power and the pulses are compressed to ~ 80 fs with a pair of transmission gratings, resulting in a total efficiency of about 75 % (see figure 3.12). The repetition rate of the oscillator is 166 MHz and thus pulse energies of 2.7 nJ are available in front of the PCF.

The most important characteristic of highly nonlinear fibers is their zero-dispersion wavelength λ_{zd}. For efficient spectral broadening, λ_{zd} should be slightly smaller than the center wavelength λ_c of the fundamental spectrum. In this case, a solitonic pulse can form that propagates without temporal broadening and maintains a high peak intensity for a long distance. New frequency components are then generated and amplified via four-wave mixing and Raman effect. As λ_{zd} is close to λ_c, the group delay for new frequencies on opposite sides of the spectrum is approximately the same, leading to symmetrically broadened spectra.

Spectral broadening in fused silica PCFs   When the first tests for spectral broadening were performed, only two classes of PCFs with largely different λ_{zd} were commercially available. On the one hand, fibers with $\lambda_{zd} \approx 1050$ nm and a core diameter a between 2.5 and 5 μm had been developed for broadening narrow-band Nd:YAG lasers with $\lambda_c = 1064$ nm. For Yb-fiber lasers with $\lambda_c \approx 1030$ nm, λ_{zd} is
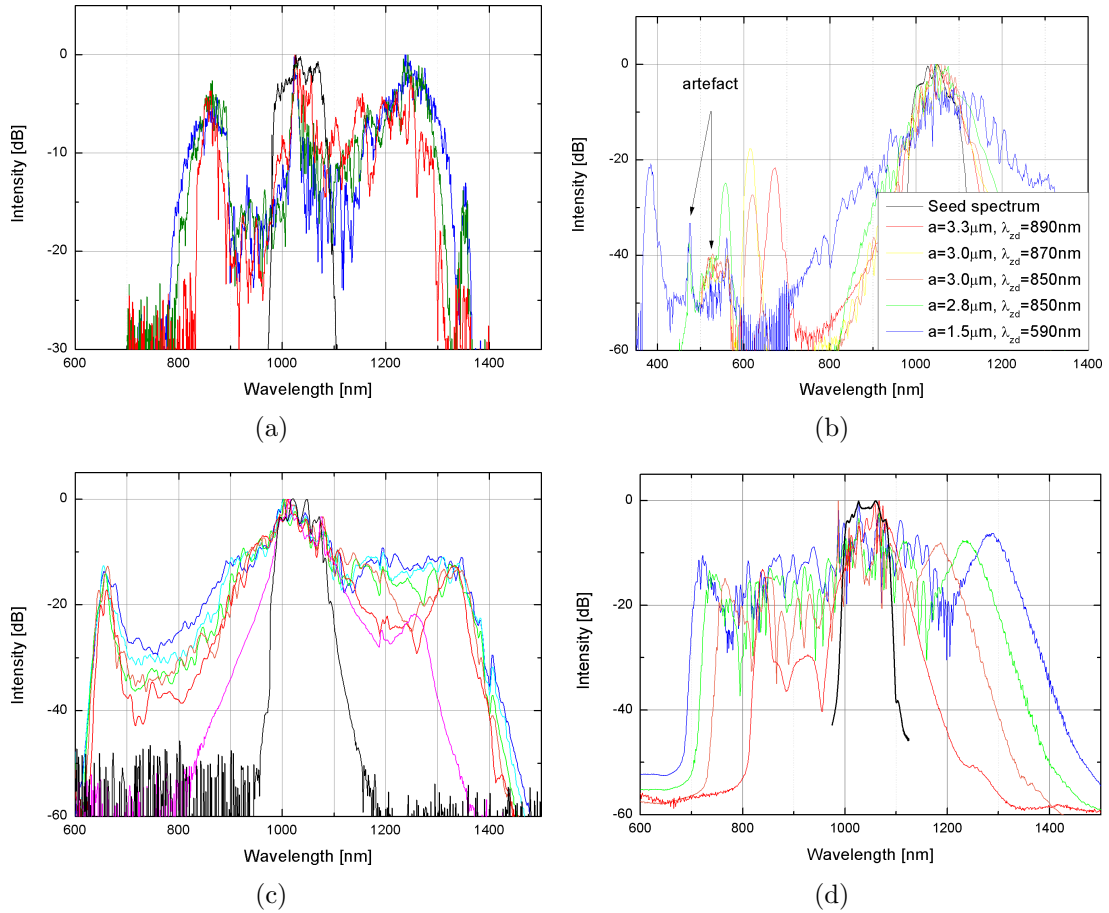
Figure 3.11: *Spectral broadening of amplified pulses from an Yb-fiber oscillator (black spectrum) (a) in 1 m of a PCF with $a = 2.3\,\mu m$ and $\lambda_{zd} = 1050\,nm$ at various power levels. (b) in 4 cm of different PCFs with $\lambda_{zd} = 590 - 890\,nm$ and $\sim 200\,mW$ coupled through the fiber. (c) in 4 cm of a SF6-glass PCF with $a = 1.5\,\mu m$ and $\lambda_{zd} = 1060 - 1080\,nm$ at various power levels. (d) in 25 cm of a PCF with $a = 3.7\,\mu m$ and $\lambda_{zd} = 975\,nm$ at various power levels.*

too large and consequently the broadening is not very efficient. The available signal power is not sufficient to generate octave spanning spectra (see figure 3.11(a)).

On the other hand, PCFs for broadening Ti:Sa lasers had been developed with $\lambda_{zd} < 900\,nm$. The spectral broadening in these fibers is strongly asymmetric, as $\lambda_{zd} \ll \lambda_c$, and shows a very distinctive feature. A sharp peak several hundred nanometers from the central wavelength is generated with its position independent from the signal power (see figure 3.11(b)). Although the distance of spectral features usually scales with power, in this combination of fiber and input spectrum, the position of the generated peak is solely a function of the fiber's core diameter. The smaller the core, the more the peak is shifted towards the blue. With the smallest

core size available ($a = 1.5\,\mu$m, $\lambda_{zd} = 590$ nm), a peak at 385 nm is generated, but 1.1 W of input power are required. This could only be demonstrated employing a double-clad amplifier. With the lower powers from the core-pumped amplifier, a peak at ≈ 535 nm is generated when using a fiber with $a = 2.8\,\mu$m and $\lambda_{zd} = 850$ nm. This is very convenient, as light at 1070 nm — abundantly available — would only need to be frequency doubled to enable f-$2f$ interferometry. 350 mW input power are sufficient to generate a peak strong enough to detect an offset beatnote with an adequate S/N for setting up a servo loop.

In comparison with Ti:Sa or Er-fiber lasers, however, the highest obtained S/N is rather low and one possible explanation is that the broadening mechanism, which is responsible for the generation of the distinct peak at the short-wavelength edge, produces significant excess noise. A different PCF, generating symmetric spectra similar to those employed in other laser systems might thus solve this issue. Recently, a PCF has been made commercially available with $a = 3.7\,\mu$m and $\lambda_{zd} = 975$ nm. First tests show symmetric spectral broadening without the formation of distinct features (see figure 3.11(d)). Measurements by another group [151] showed that with twice as much input power, octave-spanning spectra can also be obtained. The analysis of the quality of the offset beat obtained with this fiber still needs to be performed.

Spectral broadening in a SF6-glass PCF   To reduce the power requirements of the offset beat detection an alternative fiber was investigated. In cooperation with the group led by P. Russell at the Max-Planck-Institute for the Science of Light (MPL), a PCF made from SF6 glass was tested. Its nonlinear refractive index $n_2 = 2.2 \times 10^{-19}\,$m^2/W is one order of magnitude larger than in fused silica. Additionally, the core diameter was designed to be very small ($a \approx 1.5\,\mu$m), thereby increasing the fiber's nonlinearity further. Since this fiber was drawn specifically to broaden spectra of a Yb-fiber fs-laser, the design target was to obtain $\lambda_{zd} \approx 1000$ nm. A measurement of the dispersion with a white-light interferometer showed that the fiber has two different zero-dispersion wavelengths at 1060 and 1080 nm for the two orthogonal polarization eigen-states.

Using only the oscillator with an output power of 200 mW, the pulses can be compressed to 60 fs with pulse energies up to 1 nJ. Coupling only 20 pJ through the PCF is sufficient to generate an octave-spanning spectrum that is symmetric around λ_c (see figure 3.11(c)). With distinct peaks at 660 and 1320 nm, f-$2f$ interferometry should be easily possible with this spectrum. The problem of requiring so little pulse energy for spectral broadening, however, is that even less pulse energy is available afterwards in the spectral wings. Frequency doubling of the long-wavelength part is thus seriously impeded and an offset beatnote could not be detected thus far. Increasing the input power will on the one hand counteract the initial effort to reduce the required power. On the other hand, the damage threshold of SF6-fibers is so low that no powers higher than 500 mW can be coupled to this fiber without
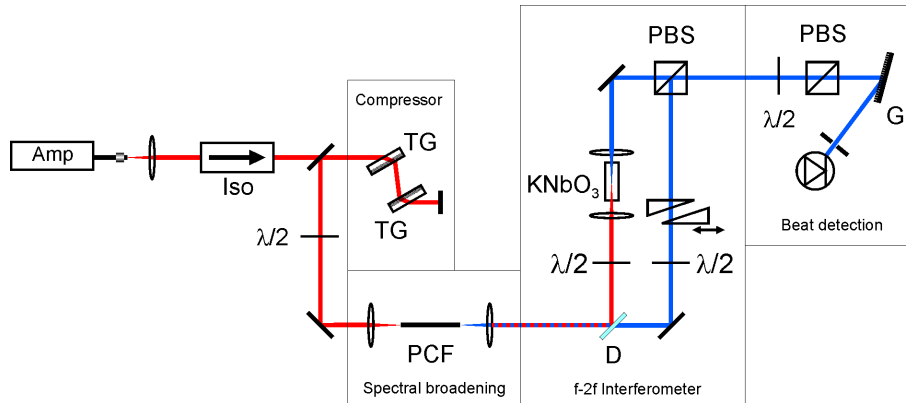
Figure 3.12: *Schematic of the detection of the offset frequency, including the pulse compressor, the spectral broadening in the PCF, the f-2f interferometer, and the beat detection unit.*

melting the input facet. Hence this particular fiber is no longer considered to be a good candidate for generating octave-spanning spectra for offset beat detection.

The results of the measurements with the SF6-glass PCF are published in Optics Express [152].

3.4.4 The f-$2f$ interferometer

Having generated an octave-spanning spectrum, a f-$2f$ interferometer as depicted in figure 3.12, is a convenient way of detecting the offset frequency for subsequent stabilization. The spectrum is split into two parts, one with short wavelengths and one with long wavelengths, using a dichroic mirror. The red end of the spectrum is then frequency-doubled in a potassium niobate ($KNbO_3$) crystal. In the blue arm of the interferometer, a pair of wedges is inserted to match its group delay with respect to the second arm. The polarization in both arms is tuned such that both beams are combined on a polarizing beam splitter, and with another half-wave plate and polarizer, the two polarizations are projected onto the same axis at an arbitrary intensity ratio. A combination of a grating and an iris is used to transmit only a narrow spectral window, in which both beams with f_0 and $2f_0$ are present, onto the photodiode.

If the beams are sufficiently strong, correctly aligned and have pulses that overlap in time, the offset frequency of the light will be detected on the photodiode. A S/N ratio of 30 dB (at a resolution bandwidth of 51 kHz) is obtained when using the PCF with $\lambda_c = 850$ nm and setting up the interferometer at 535 nm, as shown in figure 3.13. Once detected, the beatnote is employed to stabilize the offset frequency by comparing it with a reference oscillator and using the phase difference as error signal for a servo loop. Several hours of continuous operation can be achieved, as evident from the plotted counter signal in figure 3.13.
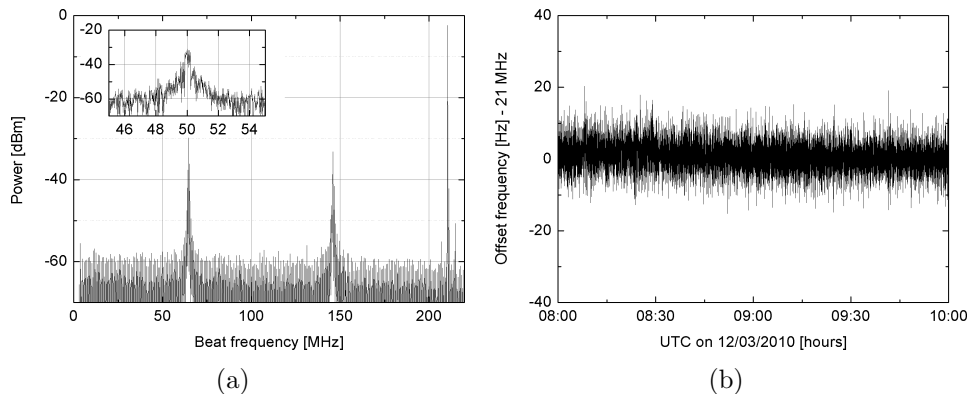
Figure 3.13: *(a) Beatnote of the offset frequency, detected after the f-2f interferometer. The octave-spanning spectrum is generated in 4 cm of a fiber with $a = 2.8\,\mu m$ and $\lambda_{zd} = 850\,nm$, 90 fs pulses at a repetition rate of 210 MHz, 320 mW input power and $\approx 70\,\%$ coupling efficiency. The resolution bandwidth of the spectrum analyzer is 51kHz. (b) Counter trace of the stabilized offset frequency. The time interval coincides with the time in which the data, shown in figure 5.8, was recorded.*

3.5   Fiber amplifiers

For most applications of a frequency comb, the output power of the oscillator itself is insufficient. Besides, an octave spanning spectrum must be generated for the f-2f interferometer. While this is possible with the light coming directly from the oscillator [152] it leaves only few milliwatts for applications, which is only useful when e.g. directly setting up a heterodyne beatnote. In every other case, the light needs to be amplified and this is exactly one of the advantages of fiber lasers. Since doped fibers have a very high gain combined with a practically infinite mode-matching between pump and signal light, they can be used to design highly efficient single-pass amplifiers

Depending on the subsequent application of the light, nonlinear effects may or may not be desirable to happen in the amplifier. They can be beneficial to broaden the spectrum and enable shorter pulses but more often they are detrimental to the pulse shape and should be avoided. A simple solution is to stretch the pulses in a passive fiber section before amplification. This method comes at the price of adding not only linear but also higher order chirp to the pulses which must be compensated for during recompression.

Another problem which is in general encountered when sending light through a fiber is the evolution of its polarization. As previously discussed, standard single-mode fibers will not preserve the polarization but instead rotate it randomly with a high sensitivity to environmental conditions. Thus, when putting a polarizer after the output, uncontrollable modulations in intensity can occur during operation. A solution to this problem is the use of PM fiber, which preserves a linear polarization
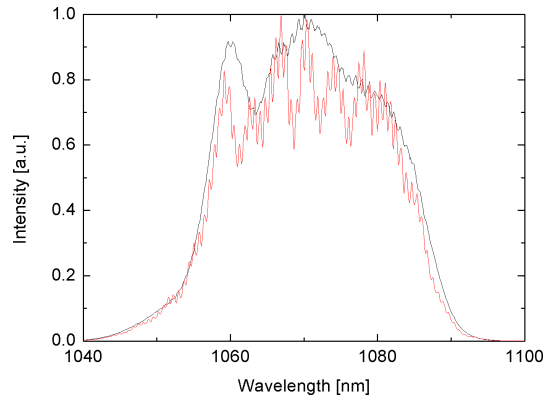
Figure 3.14: *Spectral modulation due to polarization mode dispersion (red) and its reduction (black) when the polarization of the incident light matches one of the optical axes of the fiber.*

of the incident light when coinciding with the fiber's optical axis. Aiming for a long-term stable system we have set up an all-PM system, although it is considerably more effort (and hence more expensive). All splices must be carried out with a PM-capable splicing device and at the coupling to and from the fiber, its optical axis must be carefully aligned. Since the two optical axes have a significant difference in group velocity — which is termed polarization mode dispersion — any misalignment will lead to pulse splitting and spectral interference patterns (see figure 3.14).

Doped fiber for setting up an amplifier is available in two conceptually different designs. Either the pump and signal light are guided both in the fiber core or the pump light is guided in the cladding, in which case the cladding must be surrounded by a material with an even smaller index of refraction. Both variations have been tested and are employed in the latest setup. Since the aim was for a long-term stable system, only PM-fibers were used. Especially in the double-clad amplifiers, which require large fiber lengths, the passive stability of the polarization in non-PM fibers is insufficient.

3.5.1 Core-pumped amplifiers

For the pump light to be guided in the same small core as the signal light, the beam profile of the pump diode must be well shaped to enable efficient coupling to a single-mode fiber. Therefore, only small, single emitters can be used, which limits the maximum available power. State-of-the-art diodes can deliver up to 750 mW at 974 nm. More pump power can only be obtained by combining more than one diode either with a polarization combiner or with a narrow band spectral combiner e.g. when using diodes at 974 and 980 nm.

The pump light is combined with the signal light in a WDM and absorbed in the doped fiber within a very short distance. The nominal pump light absorption

of the fibers used in this work is $1200\,\mathrm{dB/m}$ or $2000\,\mathrm{dB/m}$ at $975\,\mathrm{nm}$. Short fiber sections can thus be employed, which offers two major advantages. First, only a little TOD is accumulated and a simple grating compressor might suffice for decent pulse compression. The second advantage is related to residual back reflections. In doped fibers that have a very high gain, these reflections can mimic a cavity mirror and lead to the onset of lasing when the amplifier is only seeded insufficiently. This can even lead to the destruction of components as described in the next paragraph. In low-power, core-pumped amplifiers this risk is largely reduced, and so far, no damage has been observed when pumping an unseeded amplifier with up to $1\,\mathrm{W}$.

The choice of the optimum length of the gain fiber is best determined empirically. For large fiber lengths, the amplified spectrum narrows and shifts towards longer wavelengths. The reason for this effect is a significant overlap of the absorption and emission band of Ytterbium in the short-wavelength range. Figure 3.15(a) shows that shortening the gain fiber will reduce this reabsorption but eventually cause the absorbed power to decrease and an increasing amount of the pump light to be wasted. The optimum fiber length is thus a compromise between maximum signal output power, spectral bandwidth and peak wavelength.

In figure 3.15(b) the major advantage of Yb-doped fibers is demonstrated. Amplifiers with a slope efficiency of up to $75\,\%$ can be realized, which facilitate heat management and require only moderate pump powers. This amplifier is employed for the generation of octave-spanning spectra for the f-$2f$ interferometer as discussed in the previous section.

3.5.2   Double-clad amplifiers

While core-pumped amplifiers have advantages for the pulse evolution due to the short fiber lengths, their limitation in output power is a significant drawback. The alternative is to use so-called double-clad fibers for amplification. In these fibers, the signal light is still guided in the core but the pump light is guided in the cladding, which has a diameter that is about ten times larger. The fiber is thus multimodal for the pump light, significantly relaxing the requirements for the diode modules. Large emitters can be used and lately $25\,\mathrm{W}$ at $974\,\mathrm{nm}$ have become commercially available from a single diode coupled to a fiber with $105\,\mu\mathrm{m}$ core diameter. This advantage is also reflected in the price per Watt pump power, which is at present a factor of 60 lower for the multimode modules with respect to single-mode diodes. A WDM is obviously unsuited for coupling pump and signal light to the same fiber and a different component must be used. Specifically designed, fused pump combiners are available that can couple the light from six multimode pump fibers and one signal fiber to one output fiber with a double-clad structure.

The spatial overlap between the pump light in the large cladding and the signal light in the core is only very small. A fiber with an absorption of $1200\,\mathrm{dB/m}$ with the pump guided in a $6\,\mu\mathrm{m}$ core has an absorption of only $2.6\,\mathrm{dB/m}$ with the pump

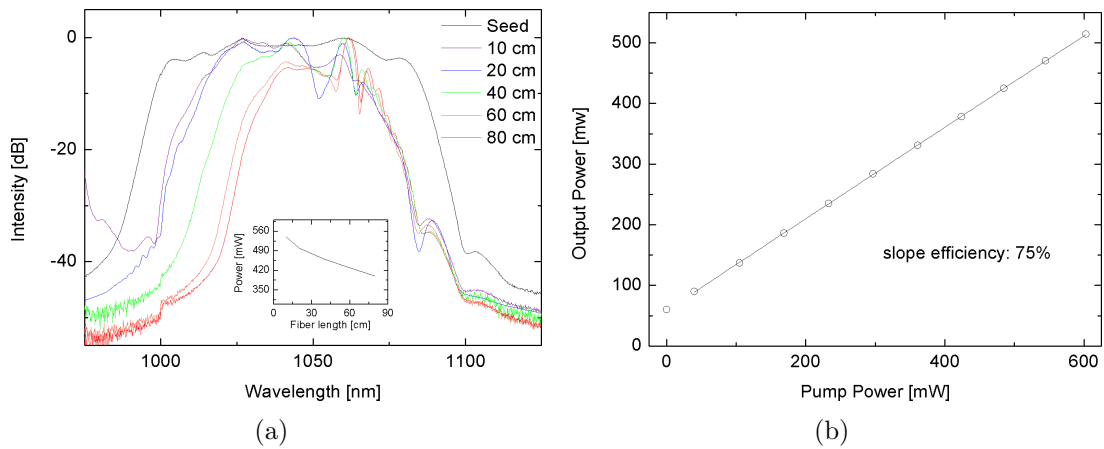(a)   (b)

Figure 3.15: *(a) Reabsorption in a core-pumped amplifier and corresponding spectral shift. The pump light is coupled to gain fiber (2000 dB/m absorption at 975 nm and 4 µm core diameter) of various lengths. The shifted short-wavelength edge of the shortest amplifier and the dip in all spectra at 1080 nm is caused by the WDM for pump coupling. The inset shows the output power at 600 mW pump power and a seed power of 140 mW. With a 10 cm long gain fiber, the pump light is absorbed only insufficiently and adds to the transmitted power. (b) Slope efficiency of the core-pumped amplifier with 20 cm gain fiber.*

guided in the cladding. The length of fiber required for efficient amplification thus increases drastically to several meters instead of centimeters. This is the main disadvantage of the double-clad design, when aiming for powers similar to those in core-pumped amplifiers. The typical application, however, is the construction of high-power amplifiers for which long fiber sections in front of the amplifier are needed anyway to stretch the pulses sufficiently to avoid nonlinearities.

Employing double-clad amplifiers increases the problems with residual back reflections as discussed above. The damage threshold of the fiber, splices or components can be exceeded if the amplifier is seeded insufficiently, especially when working with high pump powers. Since the purpose of the amplifiers is to replenish the power lost due to mode filtering, they are used after the FPCs. Once the transmission of the filter cavity has a brief dip, e.g. due to a mechanical shock or a dust particle crossing the beam, the effect can be a damaged component. To minimize this risk, a fast interlock circuit has been designed to quickly switch off the power supply of the pump diodes in case the seed power drops. Its implementation is depicted in figure 3.16. The circuit is designed such that it switches the pump diodes off within $70 \, \mu s$ after a drop in signal power. The rate of damages is significantly reduced but still not all events can be prevented. An improved version with $10 \, \mu s$ response time is currently being tested, which, according to the fiber manufacturer, should completely prevent self-induced lasing.

Regarding the choice of the optimum length of the gain fiber, the same consid-
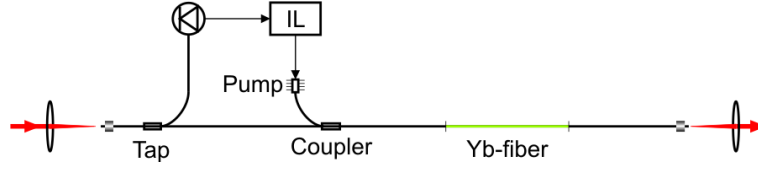
Figure 3.16: *Double-clad amplifiers including an interlock (IL) circuit to prevent self-induced lasing. Only a small fraction (1-10 %) of the signal is used for the interlock.*

erations as for core-pumped amplifiers apply. Due to the lower inversion, however, reabsorption is more pronounced and reduces the output spectral bandwidth much more. While the spectrum after core-pumped amplifiers can even be broader than the fundamental spectrum (up to 100 nm by clever exploitation of SPM), no spectra broader than 30 nm could be obtained with double-clad amplifiers when aiming for a decent efficiency.

3.6 Fabry-Pérot type filter cavities

3.6.1 Transmission of an ideal cavity

As proposed in section 2.5, a Fabry-Pérot cavity can be used as a mode filter to increase the comb's repetition rate. The phase

$$\delta = 4\pi n \frac{fL}{c} + 2\phi_m + 2\arccos(\sqrt{(1 - L/R_1)(1 - L/R_2)}), \tag{3.7}$$

acquired by any frequency component f during one round-trip in such a cavity consists of three terms: the propagation phase (depending on the refractive index n of the medium in the cavity and the cavity length L), the phase shift ϕ_m upon reflection (due to GDD of the mirrors), and the Guoy phase (depending on the cavity geometry, i.e. on the radii of curvature R_1, R_2 of the mirrors). Neglecting absorption, the amplitude A_t of the transmitted light with respect to the incident amplitude A_i is then given by

$$\frac{A_t(f)}{A_i(f)} = \frac{1 - r}{1 - re^{i\delta}}, \tag{3.8}$$

with r being the reflectivity of the mirrors. The quantity of interest, however, is the intensity transmission I_t of a FPC given by the Airy function [112]

$$I_t(f) = I_i(f)\frac{(1 - r)^2}{(1 - r)^2 + 4r\sin^2(\delta/2)} = \frac{1}{1 + F\sin^2(\delta/2)} \tag{3.9}$$

with the parameter $F = 4r/(1 - r)^2$. Light is thus transmitted whenever δ is a multiple of 2π. Neglecting dispersion and the Guoy phase (which is a small, additive
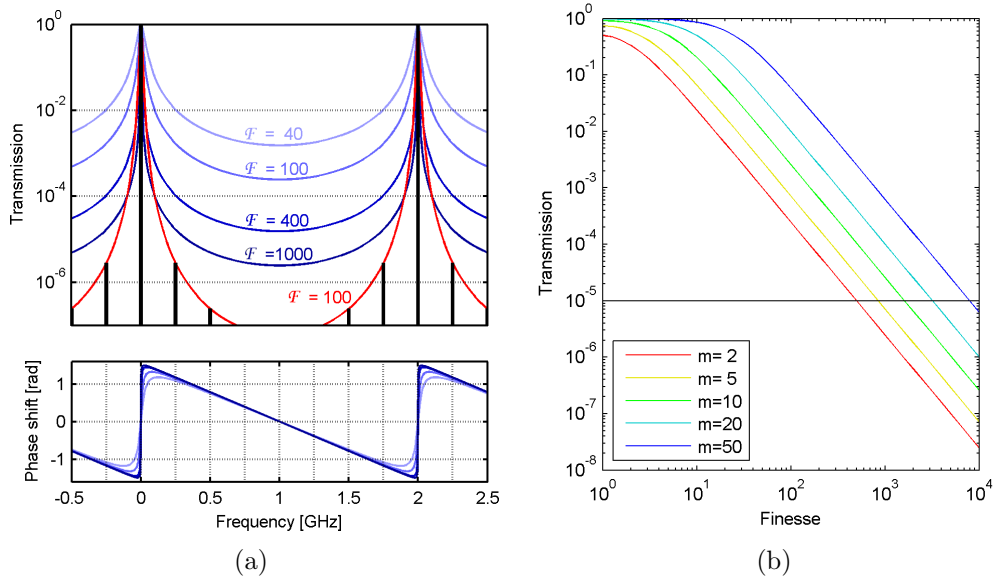
Figure 3.17: *(a) Transmission spectrum of an ideal Fabry-Pérot cavity (Airy function) and a perfectly matched comb spectrum (black) for different values of the finesse (blue). The filter ratio is $m = 8$ and the FSR is $2\,GHz$. For a cavity finesse of $\mathcal{F} = 100$, the suppression after passing the FPC twice is shown (red). Below, the phase shift of the cavity is plotted. (b) Transmission of the strongest intermediate mode of a comb, filtered with a FPC, in dependence on the filter ratio m and the finesse $\mathcal{F}$.*

phase compared to fL/c) and according to equation (3.7), the resonance frequencies are spaced with the free spectral range $\mathrm{FSR} = c/(2L)$ of the cavity. For a dispersion-free FPC the transmission has an equidistant, comb-like spectrum with zero offset. To transmit the modes of a frequency comb, the laser should consequently have zero offset frequency as well. Real cavities, however, suffer from dispersion due to the mirror surfaces and the air in between the mirrors. This leads to a non-equidistant transmission spectrum, making the definition of an offset frequency for the FPC meaningless. The effect of cavity dispersion and offsets between a comb line and the FPC's transmission peak is studied in more detail further below. In short, ignoring the comb's offset frequency might result in an imperfectly set cavity mode spacing and, as a consequence, in a reduced bandwidth of the FPC or even shifts of the detected line position.

In the case where the comb modes exactly coincide with the FPC transmission, the ratio between the length L_{laser} of the laser resonator and the separation L_{FPC} of the FPC mirrors determines the filter ratio $m = L_{laser}/L_{FPC}$. Only every m-th line is fully transmitted while the other lines are suppressed (i.e. reflected) as depicted in figure 3.17(a).

The filter depth is dependent on the finesse $\mathcal{F}$, defined as the ratio between the

free spectral range and the FWHM Δf of the cavity's transmission peak

$$\mathcal{F} = \frac{\mathrm{FSR}}{\Delta f} \approx \frac{\pi \sqrt{\mathrm{F}}}{2}, \tag{3.10}$$

with the approximation being valid for $r > 0.5$. In figure 3.17(b), the relation between the finesse of a FPC and the transmission of the first and therefore strongest intermediate mode is depicted for various filter ratios. For high finesses, this dependency is approximately inversely proportional to $\mathcal{F}^2$, and thus, increasing the finesse will further suppress the intermediate modes. On the other hand, increasing the finesse not only makes the handling of the FPC more delicate but also affects the transmitted bandwidth. The reason is that in the design of a dielectric mirror, there is a trade-off between the dispersion of the layer system and the bandwidth of the reflectivity. An alternative to increasing the finesse is to simply use either two cavities or one in double-pass, which squares the suppression without affecting the bandwidth (see fig. 3.17(a)).

It is important to note that a FPC not only modulates the intensity of the input spectrum but also the phases (see below). Evaluating the phase of equation (3.8) shows that the suppressed modes, which are next to the transmitted modes, acquire phase shifts of almost $\pi/2$ for moderate to high finesses. Especially problematic is the fact that the sign of the phase shift is opposite for the higher and lower frequency neighboring mode.

3.6.2   Optimum choice of the cavity mirrors

A FPC consists of two mirrors enclosing a Gaussian beam. At both mirrors, the phase fronts of the beam coincide with the mirror surfaces. The beam is in this way "trapped", forming a standing wave inside the resonator. Since the radii of curvature R_1 and R_2 of the reflecting surfaces define the geometry of the transmitted mode, they are a critical design parameter. An arbitrary combination of radii and mirror separation L, however, does not necessarily have a real and finite solution for the Gaussian beam parameters, but only if the stability condition

$$0 \leq g_1 g_2 \leq 1 \tag{3.11}$$

is fulfilled [134], with $g_{1,2} = 1 - L/R_{1,2}$. This is illustrated in figure 3.18(a).

Although L is fixed by the desired filter ratio, a wide range of combinations for R_1 and R_2 remains available. For practical reasons it is beneficial to choose a flat first mirror ($R_1 = \infty$), as one cavity mirror must be mounted onto a piezo actuator. To obtain a high servo bandwidth, this mirror must be small and only flat mirrors are available in the required size. Besides, in a flat-concave cavity, the beam waist is always at the flat mirror, which facilitates the alignment.
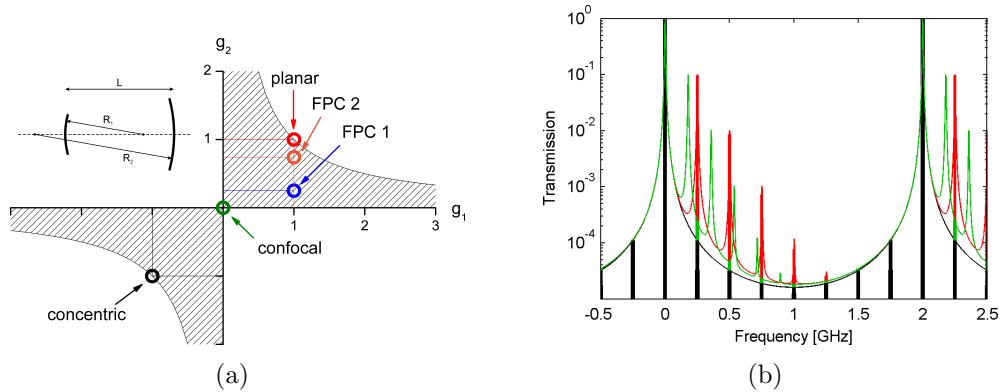
Figure 3.18: *(a) Stability diagram for a FPC. In the shaded area, relation (3.11) is fulfilled. The parameters of the two FPCs used in this work are plotted together with standard geometries. (b) Frequency comb filtered by a FPC with a filter ratio $m = 8$ and Finesse $\mathcal{F} = 400$. Higher order spatial modes with $n + m = 1, 2, 3, 4, 5$ are assumed to spatially overlap with the incident beam by -10, -20, -30, -40 and -50 dB, respectively, relative to the fundamental mode ($n, m = 0$, black). An appropriate choice of mirror curvatures ($R_1 = \infty$, $R_2 = 13L$, green) increases the transmission only by maximally 3dB, while for an unfortunate choice ($R_1 = \infty$, $R_2 = 6.8L$, red) all higher order modes coincide with intermediate comb modes.*

When choosing the radius of the second mirror, it is still possible to take another effect into consideration, namely the resonances of higher order spatial modes. These modes can also couple resonantly to the FPC, but in general at different frequencies

$$f_{qnm} = \frac{c}{2L} \left(q + \frac{n + m + 1}{\pi} \arccos(\sqrt{g_1 g_2}) \right), \tag{3.12}$$

for $g_1, g_2 > 0$. q is the longitudinal mode number and n, m are the transversal mode numbers of the Hermite-Gaussian mode under consideration. If these frequencies happen to coincide with intermediate comb modes, they can contribute significantly to the transmission and thus lower the desired suppression. It is therefore advantageous to choose an appropriate radius of the second mirror and thereby tune the higher order resonances to uncritical values. In figure 3.18(b), the effect of higher order spatial modes is demonstrated for a favorable and an unfavorable choice of R_2, assuming that the incident beam has a certain overlap with the higher order cavity modes.

The issue of higher order spatial modes can be further relaxed by applying a mode filter after the FPC. A single-mode fiber is a very efficient mode filter. Since the light is coupled to such a fiber for subsequent amplification, the contribution of higher order cavity modes can be neglected after the amplifier.

The considerations to the optimum design of the FPC are published in Applied Physics B [153].

3.6.3 Cavity dispersion and transmission

The mode spacing of a perfect cavity is equidistant. In reality, however, material dispersion or phase contributions of the mirror coatings shift the modes from their regular grid. In order to suppress the intermediate modes of the comb sufficiently, the FPC must have a reasonably high finesse and thus mirrors with a high reflectivity. These mirrors consist of many dielectric layers which impress a frequency dependent phase lag on the reflected light. For each comb mode, this phase lag adds to the phase $2\pi n f L/c$, acquired due to normal propagation. If the nonlinear phase lag — determined by the mirror's GDD and the GDD of the intracavity medium (air) — is sufficiently large, the comb mode will no longer be centered on the cavity mode and the comb's transmission will decrease (see eq. (3.9)). Although it is possible to produce mirrors with low GDD, there will always be a trade-off between the finesse of a cavity and its usable bandwidth, which is smaller than that given by the reflectivity curve of the mirrors. The approach in this work is thus to only filter a narrow, unbroadened spectrum and perform the frequency conversion steps to match the spectrograph's bandwidth afterwards. For a typical mirror in our FPCs ($r = 99.2\%$, $\mathrm{d}^3\phi/\mathrm{d}f^3 = 20\mathrm{fs}^2/15\mathrm{THz}$), the maximum additional phase amounts to only $\approx 2.4 \times 10^{-4}\,$rad per reflection (see appendix A). In comparsion with the phase of $2.6 \times 10^{-3}\,$rad, at which the transmission drops to $50\,\%$, it is clear that these mirrors will not limit the bandwidth.

An alternative approach to dielectric mirrors could be metal-coated mirrors. Far from electronic resonances, their reflection curve is flat and thus their dispersion is too. Due to non-resonant absorption, however, the reflection is in general below $99\,\%$ with especially suited metals being gold, silver and aluminum (see figure 3.19). Only low finesse cavities ($\mathcal{F} < 300$) can be constructed in this way, resulting in a poor mode suppression. Nonetheless, by using more than one FPC in series as discussed below, metal mirrors provide an appealing method for achieving large filter bandwidths. Unfortunately all three of the above-mentioned metals have some resonant absorption in the visible region which is of particular interest in this work. In the infrared region, however, broadband cavities with metal mirrors might be the optimum solution, since they eliminate the necessity to drive nonlinear processes after the filter stage.

In case the GDD of the mirrors is not limiting, the medium in between the mirrors, usually air, must be considered. Due to its dispersion, each comb mode acquires a slightly different propagation phase. This modification of the phase will lead to a walk-off between cavity transmission and comb modes as well. Starting from eq. (3.9) and calculating the maximum bandwidth $\Delta\lambda$ over which the change in refractive index Δn will not lead to a decrease in transmission by more than $50\,\%$, gives (see appendix A and [155])

$$\Delta\lambda \leq \frac{4}{\pi} \frac{\lambda^2 m f_r}{c\sqrt{F}} \frac{n}{\Delta n}. \tag{3.13}$$
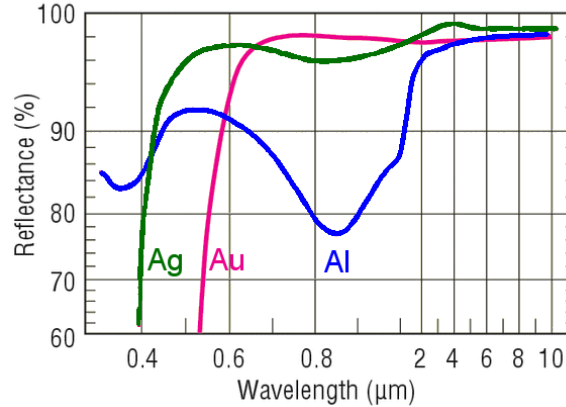
Figure 3.19: *Reflectivity of aluminum (Al), silver (Ag) and gold (Au). None of these metals has a flat reflectivity throughout the whole visible region. Nevertheless, especially gold mirrors are appealing for broadband filter cavities in the near-infrared and infrared region. Adopted from the Newport catalog [154].*

n is the refractive index of the medium, λ the central wavelength, m the filter ratio and f_r the comb's fundamental spacing. For typical parameters of an unbroadened Yb-fiber comb ($\lambda = 1030$nm, $m = 8$, $f_r = 250$MHz) this would limit the spectral bandwidth to about 150 nm. After the double-clad amplifiers, the comb spectrum is typically centered around 1060 nm and no broader than 40 nm. In the case of a FPC with a FSR of 2 or 18 GHz, this results in a maximal additional phase shift of 2.7×10^{-4} rad or 3×10^{-5} rad at the edges of the spectrum.

In the calculations above, the assumption was made, that at the center frequency f_c the cavity's FSR matches the comb's repetition rate f_r. This is, however, not automatically the case. For simplicity, first assume a dispersion-free cavity with a filter ratio of $m = 1$, which is characterized by an equidistant mode spacing (the FSR) and a well-defined frequency offset $f_{0,cav}$. At f_c, one cavity mode is locked onto one comb mode by pulling the FSR until cavity and comb mode coincide. In case that $f_{0,cav}$ equals the comb's offset frequency f_0, the FSR is pulled to match f_r. If, however, $f_{0,cav} \neq f_0$, the FSR will differ from f_r in the locked stated. This effect can be generalized to the case of filter ratios $m > 1$ when $f_{0,cav}$ only needs to match a (virtual) RF comb mode that is smaller than the FSR. Since the $f_{0,cav}$ is not easily tunable and not even well-defined in real, dispersive cavities, f_0 must be tuned to achieve $f_r = FSR$ when locking the cavity. Only in this case is the maximum spectral bandwidth, limited by the aforementioned effects, transmitted.

3.6.4   Cavity stabilization

The resonance wavelengths λ of a FPC are defined by the distance L between the two mirrors, and the width of the resonance peaks is determined by the cavity finesse $\mathcal{F}$. According to equation (3.9), for $\mathcal{F} = 400$ and $\lambda \approx 1000\,\mathrm{nm}$, a variation in the distance between the mirrors of only $0.625\,\mathrm{nm}$ will lead to a drop in transmission by $50\,\%$. Hence, tiny vibrations of the mirrors or density fluctuations of the intermediate medium suffice to shift the resonance significantly with respect to the given laser frequency. Consequently, the distance between the mirrors has to be stabilized actively via a servo loop. An error signal proportional to the difference between the maximally transmitted frequency and the laser frequency must be generated and the cavity length must be tunable. To achieve the latter, one mirror is typically mounted on a piezo tube with the light coupled through the center of the tube.

Generating a feedback signal for the stabilization of passive, optical cavities to a laser frequency is important for many applications, and several standard techniques have been developed for doing so. During this work, four of them were tested. These techniques will now be described briefly in the order in which they have been employed in the setup.

Hänsch-Couillaud lock   Phase differences between different parts of the beams can be exploited to determine the detuning of the cavity [156]. If, e.g. the cavity has a polarization dependent loss, the reflected polarization components acquire a phase shift with respect to each other, if not on resonance. In this case, originally linearly polarized light becomes elliptically polarized with the handedness of the ellipse depending on the sign of the detuning. Analyzing the polarization with a balanced receiver results in the desired error signal.

Although used in the initial tests, it soon became clear that this technique is unsuited to stabilize filter cavities. An additional element must be inserted in the cavity to induce a polarization sensitivity, thereby reducing the finesse and complicating the setup.

Dither lock   A direct way of analyzing the difference between the length of the cavity and the wavelength of the incident laser is to modulate the cavity length via the piezo voltage and observe the transmission. Part of the transmitted light is sent to a photodiode whose output is demodulated with a lock-in amplifier, referenced to the modulation frequency. This generates a bi-polar error signal which, using a second piezo actuator, keeps the FPC on resonance.

In general, a locking technique based on intensity variations is susceptible to intensity noise, in contrast to interferometric methods. Compared with the other three techniques, the dither lock indeed showed a smaller S/N and the cavity transmission was less stable. In addition, sidebands are generated at each comb mode due to the cavity modulation, which, for the application in mind, might be detrimental.

Tilt lock Alternatively, different spatial modes can be used to compare cavity length and laser wavelength [157]. Higher-order modes have a different resonance frequency than the fundamental Gaussian mode and are thus completely reflected when the fundamental mode is on or close to resonance. They serve as a reference for the fundamental mode which, again, acquires a frequency-dependent phase shift in reflection. On a split photodiode, the asymmetry of the higher-order mode is exploited to generate an error signal when taking the difference of both halves of the diode.

The tilt lock technique generates an excellent error signal for a cw laser without the need for additional modulations or components. The cw laser can be locked onto one comb mode to transmit the comb as well. As the cavity reflection is used, however, the rejected higher-order mode is outshone by the rejected comb modes. Despite the use of a spectral filter, the error signal is still compromised by the comb light. Another disadvantage is the sensitivity to the alignment of the split photodiode.

Pound-Drever-Hall lock Finally, the cavity length can be probed with different longitudinal modes instead of spatial modes. This is called the Pound-Drever-Hall (PDH) technique [158]. In this method, sidebands are impressed on the cw laser via phase modulation, which are reflected by the cavity if they are far away from the resonance. The total reflected power is detected with a photodiode and the beatnote between the reflected carrier and modulation frequency is phase sensitive to the deviation of the cavity frequency from the carrier frequency. When demodulating this beat frequency with the modulation frequency in a phase detector, an error signal is generated.

The PDH scheme has several advantages over the previously used methods. It can also be applied in transmission and in this case, the separation from the comb light is easily achieved by using orthogonal polarizations. The transmission version of the PDH scheme suffers from a lower servo bandwidth due to the photon life-time in the cavity but in our setup this is completely negligible. The photon life-time in a $2\,\mathrm{GHz}$ cavity with $\mathcal{F} = 400$ is smaller than $100\,\mathrm{ns}$. Additionally, the PDH-type locking scheme is insensitive to alignment, and fiber coupling the cw laser onto the comb is feasible. The latter is particularly important for the next generation design, because it saves the need for mode-matching of cw and comb light and employs as few bulk components as possible.

3.6.5 Implementation and performance

The first experiments using a FPC to increase the mode spacing of a comb-like spectrum were performed even before a fully phase-stabilized comb was developed [159]. In that work, however, the FPC was only used to increase the mode spacing to facilitate the determination of the mode number.
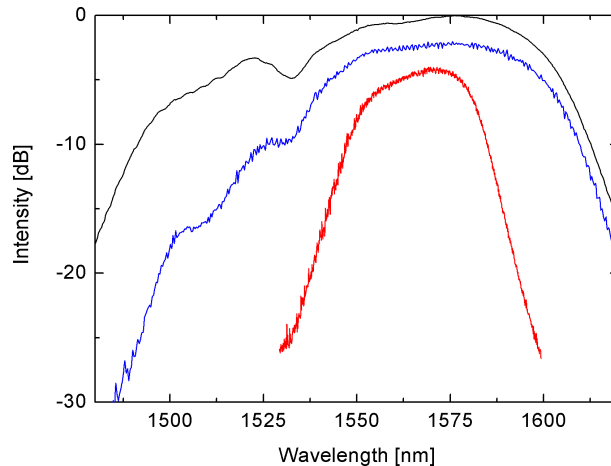
Figure 3.20: *Spectrum of an Er-fiber laser (black) filtered by a FPC with $\mathcal{F} = 400$ (blue) and $\mathcal{F} = 2400$ (red). Curves have been offset vertically for clarity.*

A precursor experiment in which the phase noise properties of a frequency comb after a filter cavity were investigated was performed in cooperation with the group led by F. Kärtner at the Massachusetts Institute of Technology [160]. An Er-fiber laser with a repetition rate of $f_r = 200$ MHz is employed and filtered to 2 GHz while testing FPCs with $\mathcal{F} = 200$ and 2000. The cavities are stabilized with the Hänsch-Couillaud locking scheme. No influence of the FPC on the phase noise is observed but an increase in intensity fluctuations occurs. This can be explained by a conversion of frequency jitter to intensity noise due to the filter characteristics of the FPC.

The first FPC-filtered comb employed at a telescope was an Er-fiber laser with $f_r = 250$ MHz [140] and a single FPC with $\mathcal{F} = 2400$ (see chapter 4). Due to this high finesse, the transmitted spectrum is significantly narrowed (see figure 3.20) but suppression ratios of 40 to 50 dB are obtained for filter ratios of $m = 10 - 60$. The cavity is dither-locked with a modulation frequency of 40 kHz.

Since the reduction of spectral bandwidth is intolerable for the final comb system, especially because of the potentially induced systematic shifts (see section 3.8), the double pass configuration was developed. The same Er-laser system has been used for tests but with tilt-locked cavities. As discussed in section 2.5, using two cavities squares the suppression without affecting the transmitted bandwidth. One variation is to pass twice through the same cavity using orthogonal polarizations. While saving one servo loop, the generation of the error signal is more involved in this case and thus the measurements were performed with two identical cavities in series. In this way, more than 70 dB suppression can be achieved with two FPCs with $\mathcal{F} = 400$ and $m = 20$ [153].

If even higher filter ratios of $m > 50$ are used, the intermediate modes are so densely spaced that the suppression of the first intermediate mode in the double pass
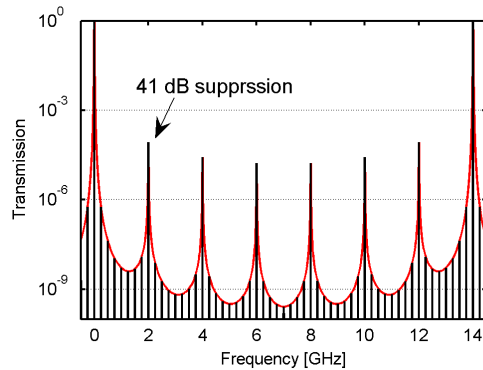
Figure 3.21: *Transmission of a frequency comb (black) filtered with two FPCs with $m_1 = 8$, $m_2 = 7$ and $\mathcal{F} = 400$. The transmission function is plotted in red.*

configuration can be lower than that of an intermediate mode in the middle of the FSR in the single pass configuration. In this case, it is beneficial to use two FPCs with different filter ratios m_1 and m_2 to first prefilter the densely spaced modes to an intermediate spacing and then only suppress all undesired modes in a second cavity. A second reason to prefer two steps is that each filter transmits only $1/m$ of the incident power, if neglecting additional losses due, e.g., to mode-matching. Splitting the filter ratio into two approximately equal parts allows for easy reamplification between the cavities, whereas in the other case, special low-noise amplifiers must be constructed that are capable of handling small seed powers. Yet another benefit of a prefilter cavity is not to have too densely spaced intermediate modes and thus allow for a good suppression of higher order modes as explained above. Starting with a fundamental repetition rate of $250\,\mathrm{MHz}$ and aiming for a final spacing of $14 - 18\,\mathrm{GHz}$, filter ratios of $m_1 = 8$ and $m_2 = 7 - 9$ are a good choice for FPCs with $\mathcal{F} = 400$. This configuration leads to intermediate modes with a spacing of $2\,\mathrm{GHz}$, which are the least suppressed. The corresponding transmission after both cavities is depicted in figure 3.21.

To measure the actual suppression of the comb modes, a heterodyne measurement can be employed. A simple RF detection of the filtered comb with a photodiode is an erroneous method since the higher and lower frequency suppressed modes have an opposite phase shift (see figure 3.17(a)). Their contributions to the RF beatnote can interfere destructively and the intensities of the RF modes overestimate the suppression of the optical modes. The heterodyne detection, on the other hand, maps each comb mode individually into the RF domain and preserves the original intensity ratios.

The heterodyne measurement has been performed after the first and second FPC with $m_2 = 7$ ($\mathrm{FSR}_2 = 14\,\mathrm{GHz}$). The intermediate mode at $250\,\mathrm{MHz}$ is suppressed by $35\,\mathrm{dB}$ after the first FPC and $50\,\mathrm{dB}$ after the second FPC. The intermediate $2\,\mathrm{GHz}$ mode is suppressed by $37\,\mathrm{dB}$ after the second FPC. These values are consistent and
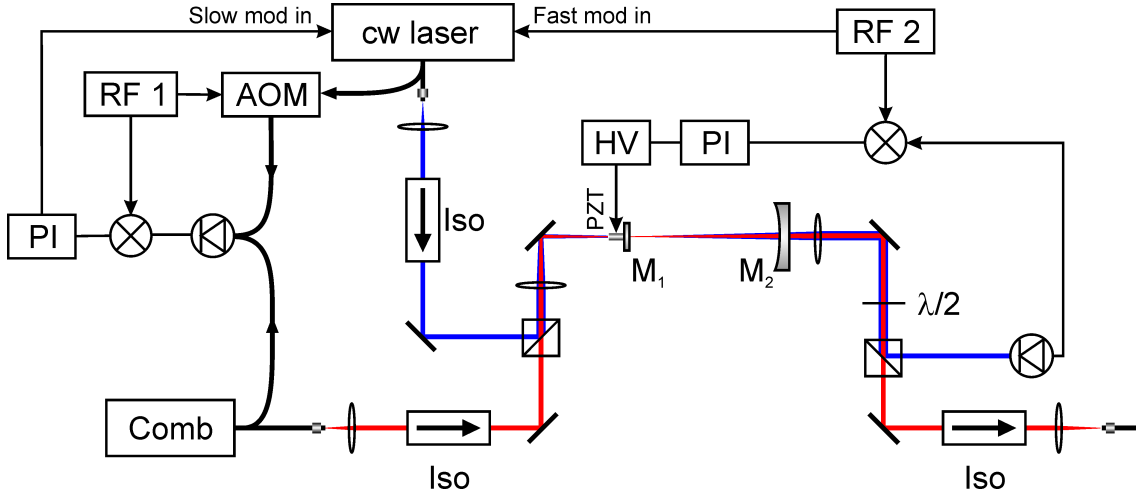
Figure 3.22: *Schematic of the FPC, consisting of the two mirrors M_1 and M_2, including coupling and PDH locking scheme. AOM: acousto-optical modulator, RF 1,RF 2: radio frequency synthesizers, PI: proportional-integral controller, HV: high-voltage amplifier.*

the actual finesses of the two FPCs are determined to be $\mathcal{F}_1 = 150$ and $\mathcal{F}_2 = 280$.

The setup in its latest version is shown in figure 3.22. A cw laser is locked onto a mode of the frequency comb. Part of it is shifted by 80 MHz with an acousto-optical modulator (AOM) and locked to the comb at the AOM frequency. The unshifted laser thus exactly coincides in frequency with one of the comb modes. In front of the FPC, the cw laser is spatially overlapped with the comb on a polarizing beam splitter, such that both cw and comb light are coupled through the cavity but with orthogonal polarizations. After the FPC, the cw laser is separated from the comb to be detected with a photodiode. For PDH-locking, the cw laser is modulated at a resonance frequency of the internal piezo actuator (at ~ 2 MHz), which at the same time is employed for compensating long-term drifts of the laser. The error signal for locking the cavity is generated by mixing the modulation frequency with the detected beatnote after the FPC. It is low-pass filtered and amplified in an adjustable proportional-integral (PI) controller, a circuitry with a tunable characteristic to shape the error signal for optimum servo performance. The same controller is employed in all servo loops of the system, i.e. also for locking repetition rate and offset frequency to an atomic clock. Finally, the control signal is amplified with a high-voltage amplifier to enable utilizing the whole travel range of the piezo actuator.

Special care must be taken to isolate the incident comb light against the reflection at the first cavity mirror. As this is highly reflective and most of the comb modes are rejected by the cavity, a large amount of the light is coupled back into the fiber. The reflection is especially critical for the amplifier in between the two FPCs, as the combination of two mode-matched high-reflectors and an intermediate gain-medium resembles a laser cavity. For low-power, core-pumped amplifiers, a single

30 dB isolator in front of the second cavity is sufficient to prevent lasing. Using a double-clad amplifier with up to 2 W output power, oscillation can only be avoided when using a 30 dB isolator after the first FPC and a 60 dB isolator in front of the second.

3.7 Spectral broadening

To cover the required wavelength range of 400 to 800 nm, the spectrum must be broadened after the filter cavities. The same strategy is pursued which has already proved to be successful when generating an octave-spanning spectrum for f-$2f$ interferometry: The narrow seed spectrum is amplified and short pulses are coupled to a highly nonlinear, microstructured fiber. In comparison with the spectral broadening for the offset beat detection, however, there are two conditions which further complicate this process. First, the increased mode spacing leads to generally lower pulse energies and second, the target wavelength range is far from the fundamental spectrum of a Yb-fiber laser.

Low pulse energies can be compensated by high-power amplifiers. For this application a double-clad amplifier, delivering up to 12 W has been designed. After the amplifier the pulses are compressed in a hybrid grating/prism compressor, which has an absolute efficiency of 65 % and thus provides 8 W for subsequent applications. Pulse durations of ~ 100 fs are obtained, which is close to the bandwidth limit of ~ 80 fs and corresponds to a 20 nm wide spectrum. While the pulse duration is comparable with that used for broadening the fundamentally spaced comb, pulse energies of only $400 - 600$ pJ are available after the compressor, when the mode spacing is $14 - 18$ GHz. With the PCFs, described in section 3.4, no sufficient spectral broadening can be achieved when seeding directly with the compressed pulses at the fundamental wavelength.

Tests have thus been performed to taper the PCFs to increase their nonlinearity. Since no professional taper station was available for use, a filament splicer (Vytran FFS-2000) was used instead. It only has a travel range of a few millimeters, though, and hence the taper length and the transition length between tapered and original diameter are both very short. An image of such a taper is shown in figure 3.23(a). The original fiber has a core diameter of $a = 1.5 \, \mu$m and a zero-dispersion wavelength of $\lambda_{zd} = 590$ nm. The tapered section is ≈ 5 mm long and the outer diameter is reduced by 30 %. This reduction of the core size not only increases the intensity of the light but also shifts λ_{zd} towards shorter wavelengths. At the fundamental repetition rate of 250 MHz and incident pulse energies of 1 nJ, sufficient spectral broadening in this taper is observed (see figure 3.23(b)) covering wavelengths from 420 to 900 nm. With this PCF, the fundamental wavelength range is only transmitted at large losses. A heterodyne measurement has been performed with the broadened spectrum and a frequency-doubled Nd:YAG laser at 532 nm and
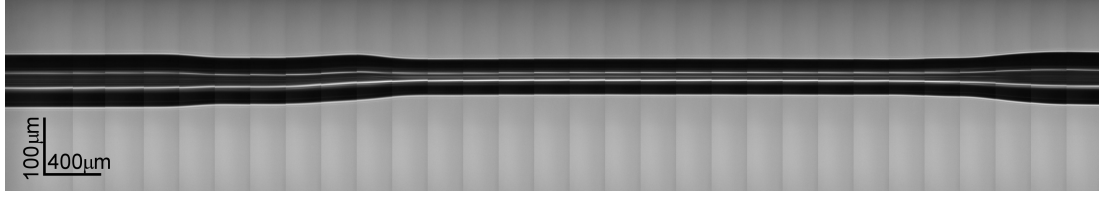
(a)
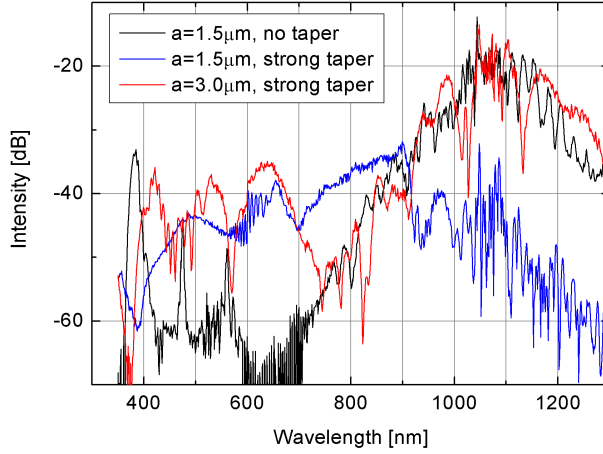
(b)

Figure 3.23: *(a) Taper of a fiber with $a = 1.5\,\mu m$ and $\lambda_{zd} = 590\,nm$, drawn with a filament splicer. The fiber is tapered three times at approximately the same position to 70 % of its original diameter. The length of the depicted fiber section is 7.7 mm. Note the aspect ratio of 1:4. (b) Spectral broadening of 100 fs pulses with $\lambda_c = 1050\,nm$ in the same, untapered fiber (black), the taper shown above (blue) and a taper of fiber with $a = 3.0\,\mu m$ and $\lambda_{zd} = 870\,nm$ (red), drawn to 50 % of its outer diameter. The pulse energies coupled into the fiber are 1 nJ for the untapered fiber and 0.5 nJ for the two tapers, corresponding to launch efficiencies of $25 - 30\,\%$.*

a beatnote can be observed. This indicates that the broadened spectrum is at least partially coherent.

The direct spectral broadening in tapered PCFs using the fundamental spectrum is very promising. Although it was not obtained using the desired mode spacing, its pulse energies and durations are comparable to the filtered, amplified and compressed pulses. Assuming that only the peak intensity of the pulses determines the nonlinear processes, the results should always be the same when using this ratio of average power to mode spacing — provided that the pulse duration can be maintained. Unfortunately, it has not been possible to couple more than $\sim 2\,W$ stably into any PCF. Above this power the coupling parameters start to drift no matter how the fiber has been mounted. Hence, improved coupling needs to be developed, e.g. by gluing the PCF tightly into a matched ceramic ferrule or splicing a short
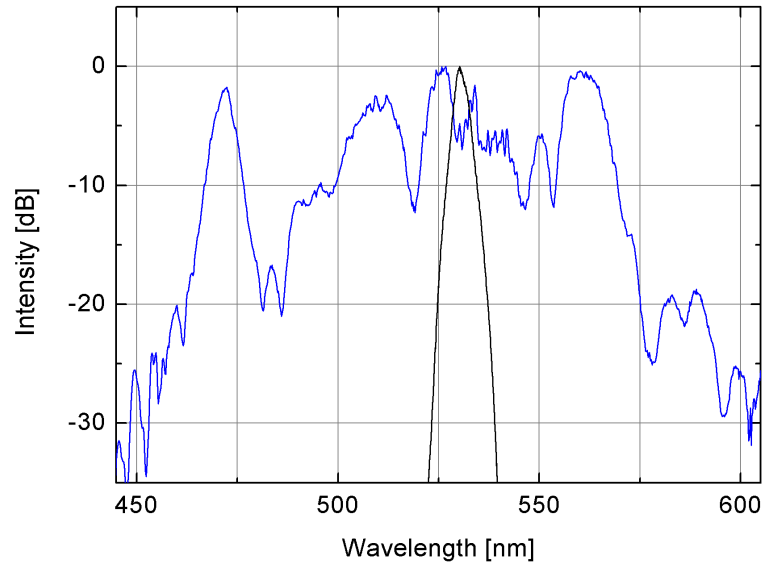
Figure 3.24: *Spectral broadening of 100 fs pulses with $\lambda_c = 530\,nm$ (black) in a tapered PCF with $a = 1.2\,\mu m$ and $\lambda_{zd} \approx 600\,nm$ (blue). The tapered section is 35 cm long and is drawn to 60 % of the original diameter.*

piece of standard fiber in front of the PCF [161].

An alternative approach is to first double the frequencies of the seed spectrum and subsequently broaden the spectrum. A drawback to this approach is the inefficiency of the sum frequency generation for low pulse energies (doubling the frequency of a ultra-short pulse is in practice four-wave mixing of all available modes, i.e. sum frequency generation). With a 5 mm long lithium triborate (LBO) crystal, 300 mW at ~ 530 nm are generated, which only provides 20 pJ with 100 fs pulses.

For a second time during this project, the group led by P. Russell provided us with a custom fiber for spectral broadening. A PCF with $a = 1.2\,\mu$m and $\lambda_{zd} \approx 600$ nm is tapered by 40 % in a 35 cm long section. With 38 mW, corresponding to ~ 2.7 pJ at 14 GHz mode spacing coupled through the fiber, spectral broadening to $465 - 575$ nm at 20 dB below the peak is obtained (see figure 3.24). While this is not yet sufficient to meet the requirements given in the previous chapter, the result is very encouraging. With further improvements, e.g. by increasing the efficiency of the frequency doubling (e.g. with a cavity) or the coupling efficiency to the PCF (which was only ~ 15 %), even stronger broadening can be expected. Based on these measurements, the design of the PCF itself can be improved as well, especially the shape of the dispersion curve.

As the results with tapered PCFs show, achieving the desired wavelength coverage of 400 to 800 nm in the near future seems to be realistic.

3.8 Impact of comb mode manipulations on the calibration

Starting with a low repetition rate frequency comb and a spectrum in the infrared region, the light is manipulated to achieve a high mode spacing comb in the visible spectral range. Naturally the question arises whether these manipulations have an impact on the calibration performance. There are in principle four mechanisms involved in the system proposed in this work: filtering the modes with a FPC to increase the mode spacing, amplification to increase the available pulse energy, sum frequency generation to convert infrared to visible wavelengths and spectral broadening in a highly nonlinear fiber to cover the desired wavelength range.

Naively, one could expect to have problems with the nonlinear steps, as these can generate photons which are potentially incoherent, i.e. do not match the original comb's frequencies and phase. It has been shown, however, that frequency conversion like sum or difference frequency generation do not affect the equidistancy of the comb modes [101].

The spectral broadening itself will also not affect the calibration. As was described in section 3.4, too narrow an input spectrum can lead to incoherent broadening, and as a consequence, drown the modes in noise. It would, however, not shift the line centers or affect the line shapes. In the end, this process can reduce the available S/N and inhibit an adequate calibration but, as with frequency conversion, it will not lead to miscalibration and simulated drifts on its own.

As long as the amplifiers are operated in the linear regime, the output pulse train is an exact copy of the seed light and there is no effect on the mode positions or intensity ratios. For optimum use of the pump power, however, the amplifiers are operated in saturation. At full saturation, the output power is independent of the seed power and any intensity fluctuations, (e.g. those induced by the FPCs) are flattened. In this case, the mode suppression would even be increased. In general, no detrimental effect of the amplifiers on the calibration performance is expected.

Now that the nonlinear processes are proven to maintain the mode's frequencies, what is the effect of the FPCs? As they are linear elements, i.e. their transmission function is not intensity-dependent, they cannot lead to the generation of incoherent photons. They will, however, modulate the spectral envelope of the modes. As long as the suppressed modes are symmetric in intensity around the transmitted mode and temporally stable, they have no other effect on the calibration than reducing the S/N on the CCD. For this reason alone, the suppression should be better than 10^4 for the measured spectral intensity to be dominated by the detector noise between the transmitted calibration lines. An asymmetric mode suppression or an asymmetry in the shape of the transmitted modes, however, will induce an absolute shift of the calibration, since the modes are not resolved by the spectrograph. A potential temporal variation of these asymmetries (e.g. due to acoustic noise, thermal drift, material degradation), will even simulate a drift. It is therefore crucial to carefully
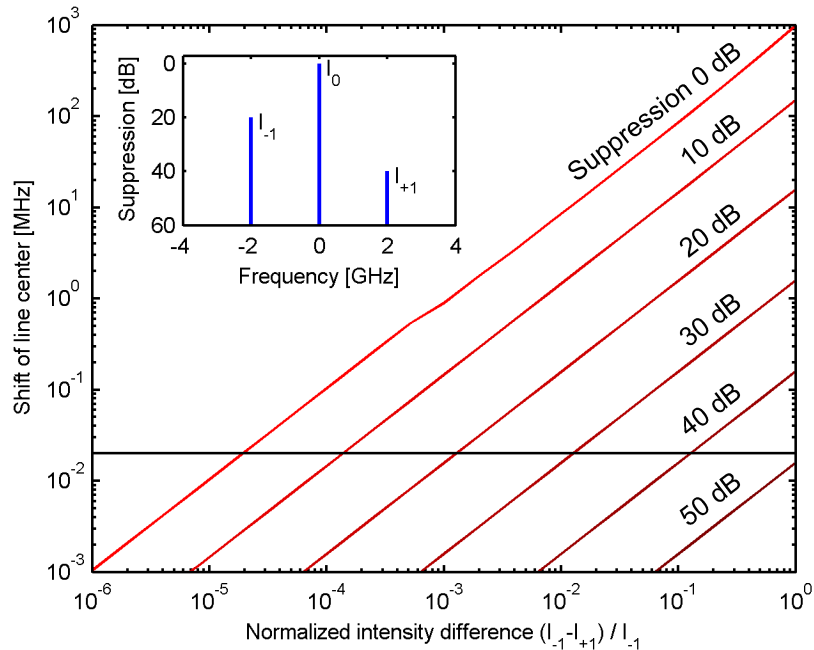
Figure 3.25: *Line shift of asymmetrically suppressed modes, as detected by a spectrograph, as a function of the asymmetry for various suppressions. The suppression is defined as the ratio I_0/I_1 between the transmitted mode and the stronger of the neighboring modes. The separation between the modes is 2 GHz and there is an additional asymmetry between the suppressed modes. The spectrograph is assumed to have a Gaussian point-spread-function with a FWHM of 5 MHz (i.e. the neighboring modes are not resolved by the spectrograph). A normalized intensity difference of 10^0 corresponds to $I_2 = 0$, i.e. the weaker, neighboring mode is completely suppressed. The black line indicates a detected shift of 20 kHz, corresponding to 1 cm/s radial velocity variation at 500 nm.*

analyze the requirements to the cavities that are necessary to guarantee a cm/s-level calibration.

After the filter cavities, the suppression must be maintained during the following manipulations of the comb light. Unfortunately, nonlinear processes can lead to a recovery of the suppressed modes. This reamplification can again induce asymmetries and in the worst case be sensitive to changes in the ambient conditions. Since this effect indeed was prominently observed in the 2010 calibration campaign, it is theoretically analyzed in this section and the results of experimental investigations are presented in section 5.5.

3.8.1 Cavity induced calibration inaccuracies

Mode suppression and tolerable asymmetry Increasing the mode spacing of a frequency comb with FPCs will inevitably lead to suppressed, but still existing

intermediate modes. Any asymmetry in their distribution, be it in intensity or position, will lead to a shift of the line detected by the spectrograph. As the frequency and thus position of the fundamental comb lines is known without any doubt, a first, important question is how well the modes need to be suppressed if there is an asymmetry in their intensities, which might already be inherent in the oscillator's spectrum. The spectrum of the oscillator itself is very smooth and intensity variations from one mode to the next are well below 10%, which can be verified by beat measurements with a cw laser. In figure 3.25 the line shift, which results from an intensity difference between one single intermediate mode and the corresponding mode on the other side of the transmitted mode, is plotted as a function of the suppression. It shows that an asymmetry of only 10^{-5} between two unsuppressed $2\,\text{GHz}$ sidemodes would lead to a shift of $20\,\text{kHz}$ or $1\,\text{cm/s}$ (at a wavelength of $500\,\text{nm}$). On the other hand, for one sidemode vanishing completely (i.e. infinite asymmetry), the suppression must be better than 10^5 to ensure sufficiently small line shifts. A mode separation of $2\,\text{GHz}$ is chosen for demonstration as this is still unresolved by the spectrograph (assuming a resolution of $5\,\text{GHz}$) and thus has a large effect without being detected as a separate line. Moreover, in the final setup, the $2\,\text{GHz}$ line is the mode with least suppression due to a setup with two FPCs (see section 3.6).

Since the initial asymmetry of the comb spectrum is unknown, it is safe to say, that with a suppression of 10^5 no asymmetric intensity distribution can lead to a detectable shift. While the initial line-by-line asymmetry is certainly smaller than $10\,\%$ (which would not require such a high suppression), it is shown below that the suppressed modes can become reamplified. This reamplification might induce additional asymmetries. Figure 3.25 gives an idea of the tolerable, induced mode asymmetry to ascertain that the detected line shift on the CCD is sufficiently small. To give an example, if one neighboring mode is suppressed by 10^2 (with respect to the transmitted mode), an intensity difference of only $0.1\,\%$ to the opposite neighboring mode is tolerable to ensure a detected line shift of $< 20\,\text{kHz}$. In the following, a flat intensity distribution for the initial comb spectrum is assumed. This is justified because the effects, discussed in the rest of this section, will be dominating.

Asymmetric line shape   If a comb line does not coincide with the transmission peak of a FPC, not only will the transmitted intensity decrease but asymmetries will also arise. One reason for this is that the comb modes are not infinitely narrow but have a linewidth of $\approx 1\,\text{MHz}$, when employing fiber lasers (see section 3.3). Assuming a finesse of $\mathcal{F} = 400$ and a FSR of $2\,\text{GHz}$, the cavity's transmission peak has a FWHM of only $5\,\text{MHz}$. When sitting on the side of the transmission peak, the shape of the comb lines is modulated, resulting in an asymmetrically transmitted line with a shifted center. The frequency of the mode — i.e. the number of cycles per unit time — is unaffected. It is phase-stabilized to the reference and remains constant at all times. The spectrograph, however, measures only intensity and will thus detect the line at a shifted position.
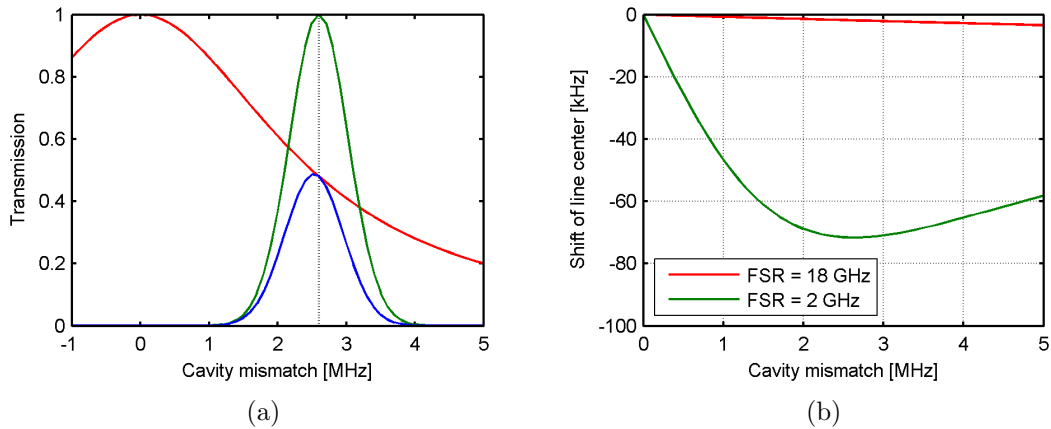
Figure 3.26: *(a) Transmission of a FPC with $\mathcal{F} = 400$ and $FSR = 2\,GHz$ (red), the normalized intensity profile of a comb mode with a FWHM linewidth of $1\,MHz$ (green) and the transmitted mode (blue). While sitting on the slope of the Airy function, the transmitted mode becomes asymmetric (not clearly visible) and the line center is shifted. (b) For the same FPC the line shift is plotted as a function of the mismatch between cavity and comb mode (green). The line center is determined from a Gaussian fit to the shifted line. For comparison, the effect of a FPC with $FSR = 18\,GHz$ is shown (red).*

In figure 3.26 this effect is shown for a comb mode which is only transmitted at 50 %, i.e. having an additional round trip phase of $\delta = 2.6 \times 10^{-3}$ rad with respect to a mode at the transmission peak. The resulting shift of the line center amounts to $70\,$kHz, corresponding to $3.5\,$cm/s in radial velocity variation at $500\,$nm. Aiming at shifts below $20\,$kHz, the maximum of the cavity's transmission should at no frequency deviate from a comb mode by more than $400\,$kHz when using these FPC parameters. The maximum deviation of a comb mode from the cavity's transmission peak in the developed comb system is $700\,$kHz. Both, contributions of the mirror dispersion and of the dispersion of air are considered (see section 3.6), leading to a maximal additional phase shift of $\delta \approx 4 \times 10^{-4}$ rad in the FPC. In case that the FSR of the cavity and the comb's mode spacing do not coincide (i.e. if the comb's offset frequency is mismatched), additional phase shifts must be considered. This effect of a FPC on the lineshape can only be reduced by choosing a lower finesse or a larger filter ratio. To maintain a required suppression and filter ratio, using two cavities in series is thus favored over increasing the finesse of a single cavity. Alternatively, the linewidth of the comb modes would have to be reduced.

Asymmetric suppression   The second reason for the FPCs to cause a shift in the measured line positions are asymmetrically suppressed modes. If the transmitted comb mode is off from the center of the cavity's transmission peak, the suppression of the neighboring modes becomes asymmetric. Since the spectrograph cannot resolve
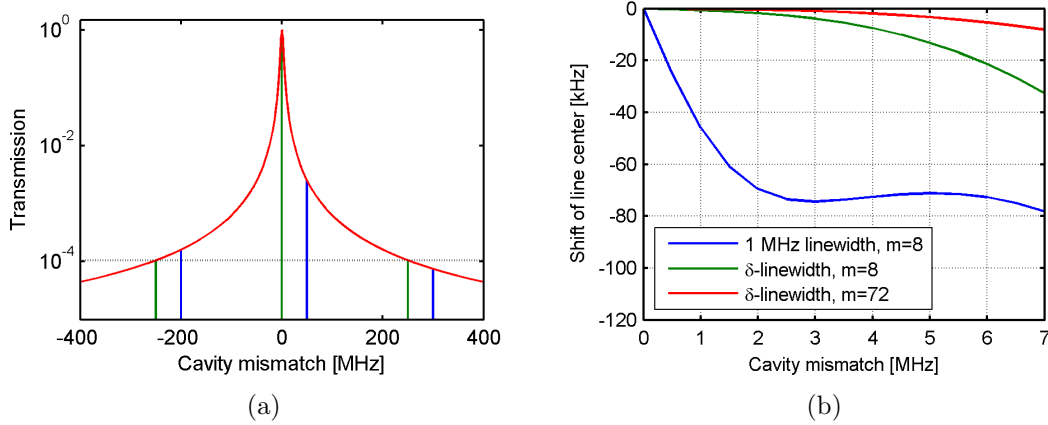
Figure 3.27: *(a) Transmission of a FPC ($\mathcal{F} = 400$ FSR $= 2$ GHz, $m = 8$) (red), and comb modes which either coincide with the transmission peak (green) or are mismatched due to cavity dispersion (blue). The suppression of the intermediate comb modes becomes asymmetric if comb and cavity have an offset. (b) For the same FPC the line shift is plotted as a function of the mismatch between cavity and comb mode for an infinitely narrow comb line (green) and a linewidth of 1 GHz (blue). The line center is determined from a Gaussian fit to a convolution of the transmitted comb modes with the point spread function of the spectrograph (having a FWHM of 5 GHz). For comparison, the effect of a FPC with FSR $= 18$ GHz, $m = 72$ is shown (red).*

the fundamental spacing of the comb modes this will shift the center of the detected line. In figure 3.27 this effect is demonstrated. For the aforementioned cavity and laser parameters and a filter ratio of $m = 8$ — corresponding to a fundamental mode spacing of $f_r = 250$ MHz — the line shift is computed by first convolving the transmitted modes with the spectrograph's point spread function and then fitting a Gaussian to the resulting line profile. First, the pure effect of the suppressed modes is calculated by assuming an infinitely narrow comb linewidth. The simulation shows that this effect is negligible for a small comb-cavity mismatch and the effect of an asymmetrically transmitted mode is dominant. This second effect can be reduced by increasing the suppression of the intermediate modes.

Cascaded cavities   When aiming for a mode spacing of about 15 GHz and starting with a fiber laser with e.g. $f_r = 250$ MHz, it is clear from the calculations above that this cannot be done in one step. The filter ratio would be $m = 60$ and demand either a finesse so high that the resulting line shifts would become significant, or an insufficient suppression of the modes. The best option is therefore to use at least two FPCs. As discussed in section 3.6 different filter ratios m_1, m_2 offer some practical advantages. In practice, $m_1 = 8$ and $m_2 = 7 - 9$ are chosen, resulting in a mode spacing of $14 - 18$ GHz.

In the case that the dispersion of air is the dominating contribution of the mismatch between comb and cavity modes, the peaks of the transmission functions of two subsequent FPCs will exactly coincide at common multiples of the two filter ratios. Using equation 3.9, it can be easily verified that the phase shift at a given frequency, which coincides with a transmission peak, is always zero for different filter ratios. The calculations above can thus be extended to the case of two cavities in series by simply multiplying the two transmission functions. As depicted in the corresponding figures, the induced line shifts are then dominated by the first FPC. On the other hand, if the mirrors are dominating the cavity GDD, the higher the filter ratio, the closer the transmission peak is to the dispersion-free case and thus to the comb modes. The asymmetries induced by a second FPC with a higher filter ratio can therefore be neglected.

3.8.2 Nonlinear processes and mode suppression

After filtering the frequency comb with FPCs and thereby increasing its mode spacing, the light will be doubled in frequency and spectrally broadened. As was discussed above, these processes will not induce frequency shifts, but may lead to a reamplification of the suppressed modes and must therefore be studied in more detail.

Frequency doubling   When frequency doubling a short pulse, the evolution of the fundamental field E_1 and the second harmonic field E_2 (oscillating at the carrier frequencies ω_1 and $\omega_2 = 2\omega_1$) must be calculated by solving the wave equation within the crystal. The second-order nonlinear polarization

$$P^{(2)} \propto \chi^{(2)} \left(E_1 + E_2 + \text{c.c.}\right)^2 \tag{3.14}$$

is the source term for new frequencies in the wave equation with $\chi^{(2)}$ being the second order susceptibility of the material. Assuming small conversion efficiencies, i.e. that the fundamental field is unaffected by the conversion process, the second harmonic field at frequency Ω after propagating a distance L in the crystal is given by [118]

$$E_2(\Omega, L) = -i \frac{\chi^{(2)} \omega_2^2 L}{4c^2 k_2} \operatorname{sinc}\left[\left(\Delta(v^{-1})\Omega - \Delta k\right) L/2\right] \int E_1(\Omega') E_1(\Omega - \Omega') \, d\Omega', \tag{3.15}$$

with k_2 being the propagation constant of the second harmonic wave. The group velocity mismatch $\Delta(v^{-1})$ and the wave vector mismatch Δk determine the efficiency of the process. A crucial factor for the intensity distribution of the modes after frequency doubling is the integral of the product of the fundamental fields. To understand its impact, first consider a transmitted mode of the FPCs at ω_1 with two neighboring, suppressed modes at $\omega_1 \pm \Delta\omega$. Each mode can be assumed to be a
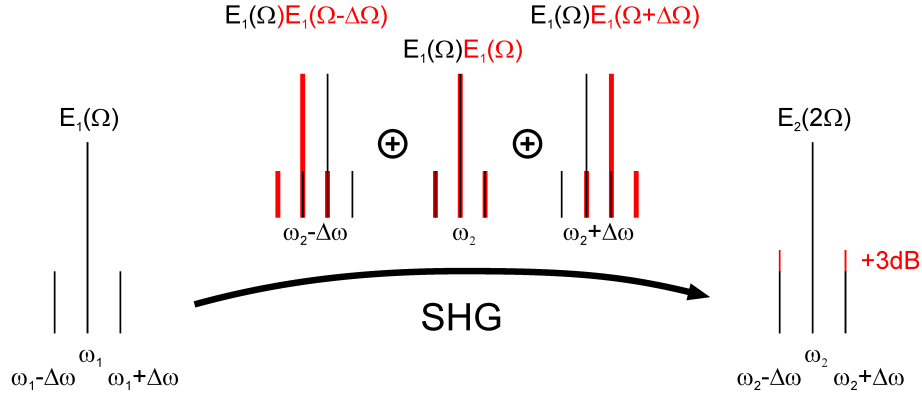
Figure 3.28: *Reamplification of suppressed modes in the SHG process. For details see text.*

δ-function and evaluating the integral simply turns into systematically summing up the contribution of each mode mixed with each other. Contributions of a suppressed mode mixed with another suppressed mode can be neglected. Relevant contributions derive thus only from the product of the transmitted modes with themselves $(E_1(\omega_1)^2)$ and from products of the transmitted modes with the suppressed modes $(E_1(\omega_1)E_1(\omega_1 \pm \Delta\omega))$. Figure 3.28 shows that the suppression of the frequency-doubled, neighboring modes $E_2(\omega_2)/E_2(\omega_2 \pm \Delta\omega)$ is decreased by $3\,\mathrm{dB}$, if all modes add up constructively (i.e. neglecting relative phases between the modes). In this worst case two contributions add up for the neighboring modes, while only one combination of fundamental modes contributes to the doubled, transmitted mode. This reasoning stays true if extending this picture to an infinite series of filtered comb modes. When detecting the modes with a photodiode, of course the intensity is relevant and its suppression is consequently reduced in the frequency doubling step by $6\,\mathrm{dB}$ at maximum.

A central simplification in the calculation above has been the assumption of small conversion efficiency. It is justified for the SHG stage, which is employed in this work, since only $\sim 5\,\%$ doubling efficiency could be achieved. If, in the future this can be improved, e.g. by increasing the amplified spectral bandwidth and subsequently reducing the compressed pulse width, a depletion of the fundamental pulse can no longer be neglected. In this case, however, a computation of the suppression after the frequency doubling stage becomes much more complex.

Spectral broadening   The final, nonlinear step is broadening the comb in a highly nonlinear fiber. Glass fibers, being an anisotropic medium, have a vanishing second order susceptibility and third order nonlinearities, governed by $\chi^{(3)}$, are dominant. A variety of effects are associated with a third order susceptibility and they can be classified as parametric and nonparametric effects [162]. Parametric effects will not affect the medium except during the interaction time and will thus conserve

the energy of all photons involved. Self- and cross-phase modulation, parametric amplification and modulation instability are prominent examples. Nonparametric effects will affect the medium via absorption or stimulated emission, e.g. stimulated Raman or Brillouin scattering, two photon absorption or saturable absorption. The origin of spectral broadening is a complex interplay between parametric effects and scattering processes. The evolution of a femtosecond pulse in a fiber can be modelled by a generalized nonlinear Schrödinger equation [119]. Depending on the effects that will be included in the model, this equation can become quite extensive, e.g.:

$$\frac{\partial A}{\partial z} + \frac{\alpha}{2}A + \frac{i\beta_2}{2}\frac{\partial^2 A}{\partial T^2} + \frac{\beta_3}{6}\frac{\partial^3 A}{\partial T^3} = i\gamma\left(|A|^2 A + \frac{i}{\omega_0}\frac{\partial}{\partial T}(|A|^2 A) - T_R A\frac{\partial|A|^2}{\partial T}\right). \quad (3.16)$$

A denotes the slowly varying pulse envelope, ω_0 the carrier frequency, T the retarded time and z the propagation coordinate. α is the fibers's absorption coefficient, $\beta_{2,3}$ the second and third order dispersion, γ the coefficient of the instantaneous nonlinearity and T_R is related to the Raman response function. This equation cannot be solved analytically and numeric algorithms such as the split-step Fourier method have been developed to study the behavior of ultrashort pulses in nonlinear fibers.

Recently, an analysis of the impact of the nonlinear effects responsible for spectral broadening on the suppression ratio of comb lines, filtered with a FPC, was performed [163]. Parametric amplification, being one aspect of four-wave mixing, was proposed as a reason for the recovery of initially suppressed modes. Four-wave mixing (FWM) in general describes the interaction of four photons at frequencies $\omega_1, \omega_2, \omega_3$ and ω_4. Parametric amplification is a FWM process which converts two photons at ω_1 and ω_2 into two new photons at ω_3 and ω_4. In the case that $\omega_1 = \omega_2$ is the frequency of a transmitted comb mode and ω_3 and ω_4 are the frequencies of the upper and lower neighboring modes, this effect will lead to a decreased suppression. The inverse process can happen as well, but only with reduced probability, since the suppressed modes are much weaker.

This process is strictly symmetric, due to energy conservation

$$\hbar(\omega_1 + \omega_2) = \hbar(\omega_3 + \omega_4). \quad (3.17)$$

For any photon generated by parametric amplification in a lower frequency, suppressed mode, a photon in the corresponding higher frequency, suppressed mode will be generated as well. When considering the neighboring modes of a transmitted mode, the center of the convolution with the spectrograph's resolution will not be shifted. Still, locally in the spectrum, this effect can lead to asymmetries if the higher and lower neighboring modes under consideration are more than one FSR away from the central mode. Since parametric amplification is a phase-sensitive process [164], the phase-asymmetry of the suppressed modes can be transfered in an asymmetric reamplification of the suppressed modes.

Not only is parametric amplification phase sensitive, but in the case of large conversion efficiency, the phase can also change depending on the mode's intensity

[119]. The final intensity distribution and possible line shifts can therefore critically depend on fiber length and even more so on the input power. As this can change over time, temporally varying line shifts would be the consequence and thus a drifting calibration.

In addition to the parametric processes, nonparametric processes are not bound to energy conservation. They, too, will happen in a highly nonlinear fiber, and can possibly lead to reamplified intermediate modes. In particular, Brillouin scattering could be responsible for an induced asymmetry, as its gain bandwidth is very narrow (on the order of several MHz) and in scattering processes the red-shifted Stokes-sideband is typically stronger. In conventional fibers, Brillouin scattering is phase-matched with a forward-traveling acoustic wave in the fiber and the light is scattered in the backward direction. In microstructured fibers, however, the acoustic wave can also be trapped in the transverse direction and forward scattering is possible. Recently, forward Brillouin scattering has been demonstrated to generate cascaded sidebands in a PCF, if pumped strong enough [165]. A back-of-the-envelope estimation of the efficiency of this process, however, suggests that this process should be several orders of magnitude too weak to cause problems with the available pulse energies.

Since the actual strengths of these nonlinear effects in fibers are sensitive to the exact parameters of the fiber and the input pulses, simulations will not suffice to exclude potential line shifts or even drifts. At present it is not even clear which of these processes actually might be responsible for a recovery of suppressed modes, but measurements clearly show that this effect indeed happens and that its impact is tremendous. The accuracy and stability of the calibration comb's modes had to therefore be checked experimentally. The results of these tests are presented in section 5.5.

Chapter 4

Proof-of-principle calibration tests

4.1 Calibrating the VTT solar spectrograph

The first opportunity to test a frequency comb at an astronomical spectrograph was in 2008 at the Vacuum Tower Telescope (VTT) on Tenerife. The VTT is a solar telescope, operated by the Kiepenheuer Institute for Solar physics (KIS) with a 70 cm primary mirror and a focal length of 46 m. The light can be slit-coupled to an echelle spectrograph which has a resolution of $R \approx 250000$ when using the infrared-optimized grating in fifth order. At a wavelength of $1.5\,\mu$m, this corresponds to a FWHM of the point-spread-function of 800 MHz or 1.2 km/s. As an echelle spectrograph operates under a large diffraction angle in a high diffraction order, adjacent echelle orders will overlap on the detector. This can be prevented by either using a predisperser in front of the spectrograph or, as was the case in this measurement, a narrow band interference filter in front of the detector. The spectral bandwidth on the detector is 1.5 nm. The detector is a 1k×1k HgCdTe CMOS camera with a linear dynamic range up to 350000 photoelectron counts that samples the spectrum at 172 MHz per pixel (i.e. 4.6 pixel per resolution element). If the detection were dominated by the photon noise of the signal, the lower limit of the uncertainty of one single line, according to equation (2.19), is

$$\sigma_i \geq 0.41 \frac{1200\,\mathrm{m/s}}{195 \times \sqrt{4.6}} = 1.2\,\mathrm{m/s},\qquad(4.1)$$

with S/N ≤ 195 in a single exposure. There is, however, a significant dark count rate, induced by thermal photons that are also detected. Assuming that they are detected with the same quantum efficiency as the signal photons, this will reduce the S/N and lead to an upper limit of the uncertainty of a single line of

$$\sigma_i \leq 0.41 \frac{1200\,\mathrm{m/s}}{113 \times \sqrt{4.6}} = 2.0\,\mathrm{m/s},\qquad(4.2)$$
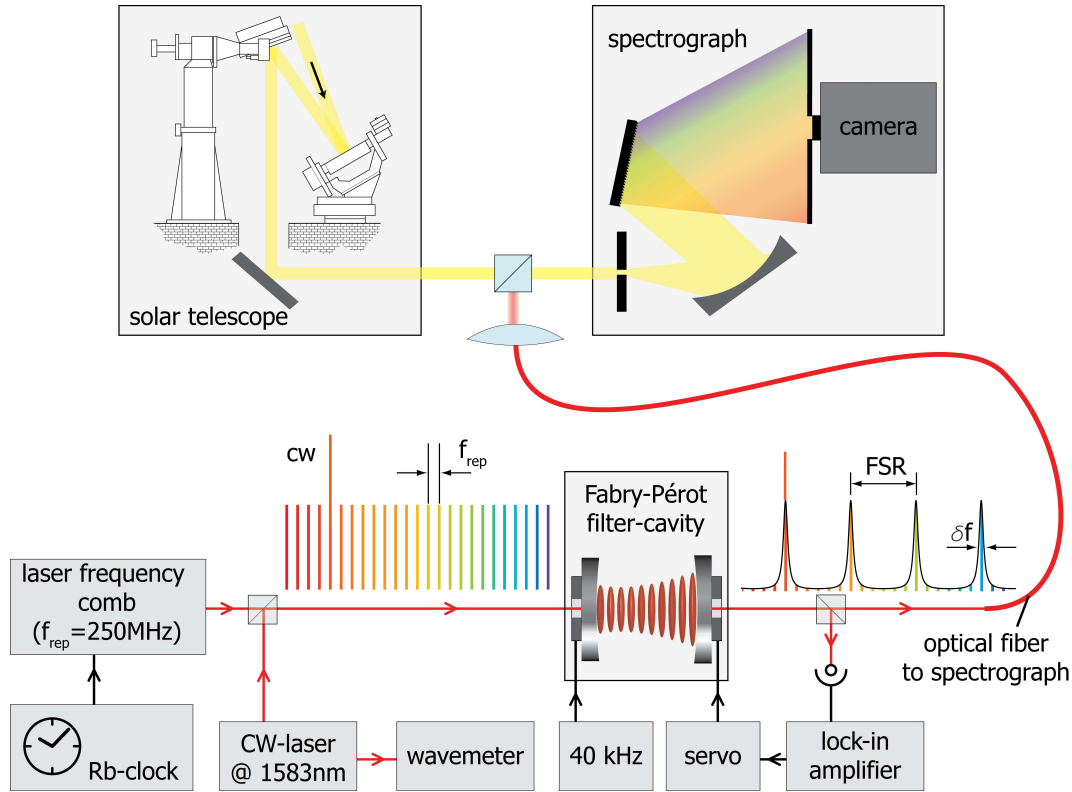
with a minimum S/N of 113.

Figure 4.1: *Sketch of the experimental setup of the calibration tests at the Vacuum Tower Telescope. An Er-fiber frequency comb with a repetition rate of $f_r = 250\,MHz$ was filtered with a FPC to mode spacings from $1\,GHz$ to $15\,GHz$. The comb is phase-locked to a Rb-clock and a cw-laser was locked to one comb mode to determine its mode number n. The cw laser is also sent through the FPC, to be able to monitor, that at any time, the same fundamental modes of the comb are transmitted. The comb light is then coupled to the spectrograph via a beamsplitter, where it can be superimposed with light from the Sun. The spectrograph has a resolution of $\sim 800\,MHz$ at wavelengths around $1.5\,\mu m$.*

The VTT spectrograph was chosen for the first proof-of-principle demonstration, as it has a very high resolution and an infrared CCD. In this combination, a readily available Er-fiber frequency comb (Menlosystems FC1500-250) could be used and the modes only needed to be filtered moderately. The oscillator design of an Er-fiber laser is identical to that of an Yb-fiber laser, except that no grating pair is needed for dispersion compensation, since the GVD of doped fiber and the standard fiber in the coupler and collimators has opposite signs. Careful adjustment of the fiber lengths thus suffices to compensate the cavity GDD. The mode separation was set to $f_r = 250\,\text{MHz}$ and the frequency comb emitted a spectrum ranging from 1480 to 1620 nm. The modes were filtered with one FPC, which was dither-locked to the transmission signal. The cavity mirrors had a reflectivity of 99.87 %, leading to a finesse of 2400 and the transmitted spectrum is shown in figure 3.20.

The frequency comb was phase-stabilized to a rubidium atomic clock with an accuracy of 5×10^{-11} (1.5 cm/s), which was far more accurate than needed. A cw-laser was locked onto one comb mode (by first frequency shifting it with an AOM and then locking it at the AOM's frequency) to determine its mode number n. It was also coupled through the FPCs to serve as a marker laser and to ensure that the same fundamental mode was always transmitted through the cavity. After the FPCs, the light was coupled to a single-mode fiber, which delivered it to the 40μm entrance slit of the spectrograph. Approximately 1 m in front of the slit, comb and Sun light could be superimposed on a beam splitter cube. See figure 4.1 for an overview of the setup.

With a mode spacing of 15 GHz, a series of acquisitions was taken for demonstration purposes with both sunlight and a comb calibration superimposed. In figure 4.2, the two-dimensional raw data is plotted with the photoelectron counts encoded on a linear color scale. In the horizontal direction of the detector, the light is spectrally dispersed, while the vertical direction is a cross section of a few percent of the Sun's photosphere. Dark lines, being either Fraunhofer lines or absorption lines of the Earth's atmosphere, are visible. Previously, the atmospheric lines were used for calibration, but they are few and spread far apart. For comparison, the only thorium line in this wavelength range was recorded. This was done in a separate acquisition, as it takes 30 minutes integration time to record this line, whereas only 1 s suffices for the solar and comb exposure. This is another advantage of frequency combs over spectral lamps. High flux per line can be achieved, which can be advantageous when observing very bright objects like the Sun.

4.2 Calibration repeatability

A time series of 12 acquisitions was recorded to determine the repeatability of the calibration with the frequency comb. The mode spacing was once again 15 GHz and no sunlight was superimposed for this measurement. Individual Lorentzians were fitted to the recorded modes to determine their line center. For each mode, the difference in position on the CCD with respect to a reference acquisition was computed and averaged over all 11 modes. The result is plotted in figure 4.3. After approximately 7 min, the calibration deviates from the reference acquisition at time zero by more than 50 m/s. This is significantly more than the photon noise limited repeatability. Since the spectrograph is neither temperature stabilized nor in vacuum (although its housing could be evacuated), it is not surprising that there are detectable drifts of instrumental origin. From a linear fit to the data, a drift of 8 m/s per minute is derived.

In comparison with other astronomical spectrographs, which are specially designed for high stability, the VTT spectrograph drifts strongly. As it is a solar spectrograph, however, passive stability is not as important as with spectrographs,
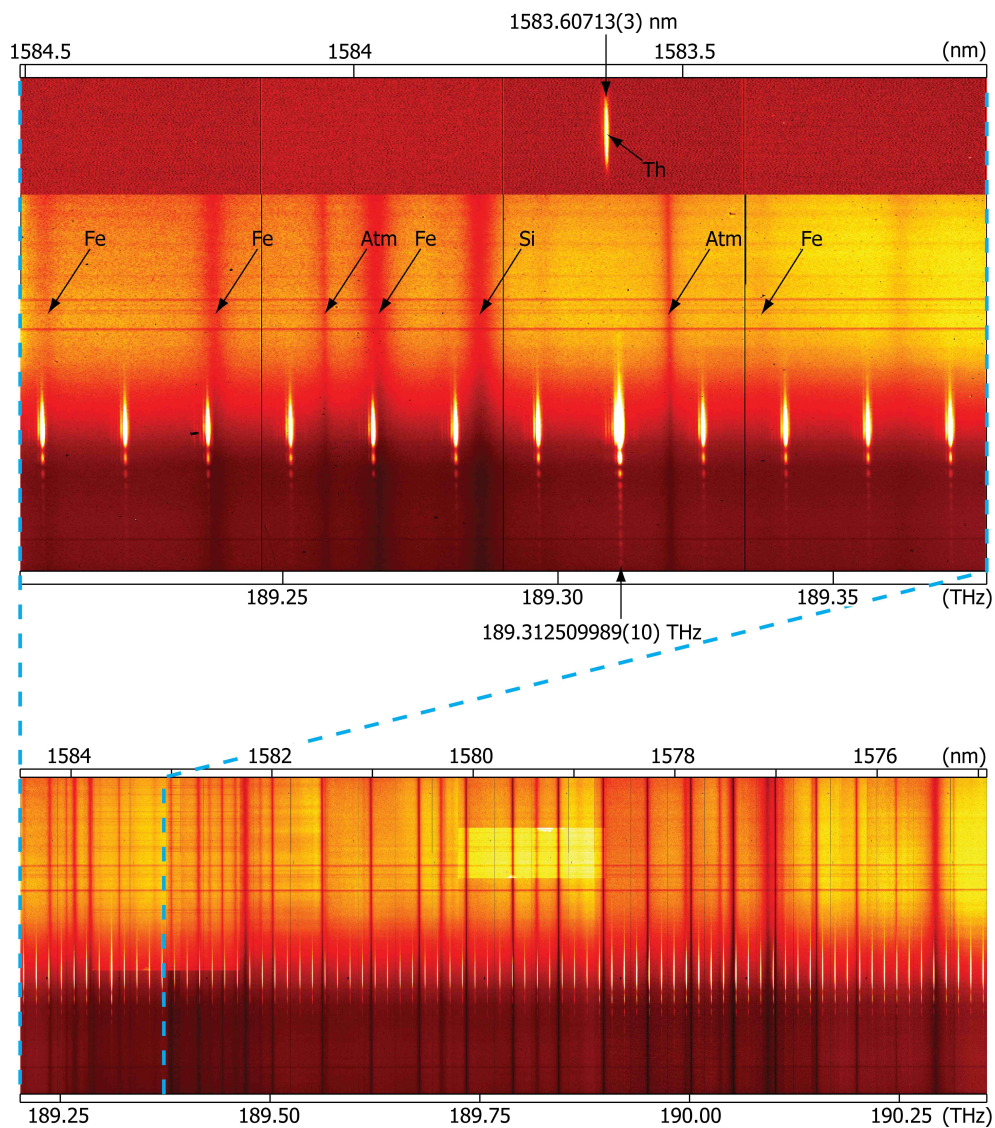
Figure 4.2: *Spectra of the solar photosphere (background image) overlaid by a frequency comb with 15 GHz mode spacing (white). Spectra are dispersed horizontally, whereas the vertical axis is a spatial cross section of the Sun s photosphere. The upper panel shows a small section of the larger portion of the spectrum below. The brighter mode labeled with its absolute frequency is the cw laser, used as marker and to determine the mode number n. The uncertainty of this mode's frequency is determined by the Rb clock. Dark lines are either Fraunhofer lines (labeled with their atomic origin) or absorption lines of the Earth's atmosphere ("Atm"). Also shown in the upper panel is the only thorium emission line lying in this wavelength range from a typical hollow-cathode calibration lamp. The nominal horizontal scale is 1.5×10^{-3} nm per pixel with ~ 1000 pixels shown horizontally in the upper panel. Black horizontal and vertical lines are artifacts of the detector array.*
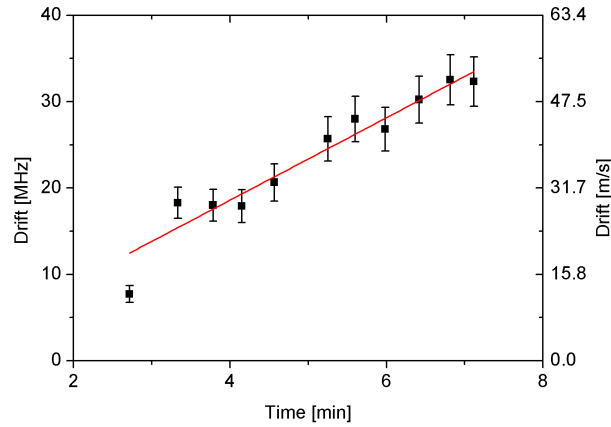
Figure 4.3: *Repeatability of the comb calibration of the VTT spectrograph. A series of 12 acquisitions with 10 ms exposure time is recorded and the average difference of the 11 comb lines is plotted with respect to a reference acquisition at time zero. The error bars represent the standard deviation of the drift of individual lines per acquisition. A linear fit (red) to the data results in an average drift of 8 m/s per minute (5 MHz/min). Note that the ordinate labels in cm/s are only approximative since $\delta v = (c/f)\delta f$. The inaccuracy is smaller than 0.1%, however.*

which are used to observe faint, cosmic objects where the exposure time can be anywhere from several minutes up to a few hours. The typical exposure time at the VTT is only a few milliseconds and within this time scale, instrumental drifts are truly negligible (8 m/s per minute = 0.1 mm/s per millisecond). Drifts between two acquisitions will then be monitored by the calibration. Using a frequency comb could thus facilitate the monitoring of drifts on the sub-m/s scale when taking acquisitions at a rate of several Hertz.

4.3 Absolute calibration

To perform an absolute calibration of the spectrograph, a relation between the frequency of the light and the CCD pixel it is illuminating must be established, the calibration curve. To first order, the number of the pixel on which a comb's mode is imaged, will be proportional to the mode's frequency. Projections, aberrations and other effects, however, will lead to a nonlinear frequency-to-pixel map. With a comb mode spacing of 3 GHz the calibration curve of the VTT spectrograph was derived in a single acquisition using 57 lines (see figure 4.4). A quadratic model is appropriate, as higher order polynomials do not reduce the scatter of the residuals further. The standard deviation of the quadratic residuals is 9 m/s, which is already better than any calibration one could hope to achieve with spectral lamps (see section 5.6). Comparing the residuals of the calibration curve with the photon noise limit of 0.8 m/s for this acquisition, it is obvious that a quadratic model is too simple
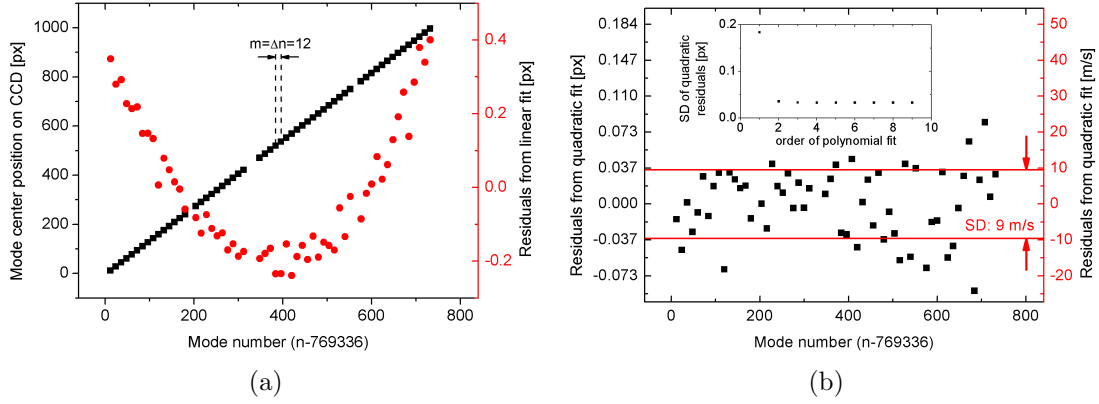
(a)   (b)

Figure 4.4: *(a) Fitted line center positions of 57 comb modes (black) and residuals from a linear fit (red) versus the mode number of the unfiltered comb. The filter ratio is $m = 12$, leading to a 3 GHz mode spacing. Some modes could not be considered as they coincided with large detector artifacts and/or the cw laser. The average slope is 172 MHz per pixel and the linear residuals still show a strong quadratic dependency. (b) Residuals from a quadratic fit to the line center versus position distribution. The standard deviation (SD) of the residuals is 9 cm/s and the quadratic fit largely reduces the residuals with respect to the linear fit. A higher order fit, however, will not improve the SD of the residuals, which is shown in the inset.*

for the frequency-to-pixel map. There is probably an unmodelled, fine structure on the calibration curve that derives from pixel-to-pixel or even intrapixel sensitivity variations. With a frequency comb, this could be mapped by tuning the comb modes and thereby scanning over each pixel, but this was not done in this first test.

In cosmic astronomy, it is usually unnecessary to determine the absolute redshift of an object on the m/s scale or better. This is different when observing the Sun. For example, in helioseismology, it is interesting to measure the absolute velocity of the solar surface, i.e. whether it is moving up- or downwards. A calibration of the spectrograph with a frequency comb will be able to provide this information on the sub-m/s scale.

The results presented in this chapter have been published in Science [44].

Chapter 5

Calibration of a high precision, astronomical spectrograph

5.1 The HARPS spectrograph

For many years, being able to detect changes in radial velocity below one m/s seemed an impossible task. For typical high resolution spectrographs, this variation in redshift corresponds to a change of the stellar line's position on the CCD approximately 1/1000 of a pixel or about 10 nm! A temperature variation by 1 K or the change of atmospheric pressure by 1 mbar would already produce effects on the order of 100 m/s [87]. Nevertheless, in 1998, ESO decided to develop a spectrograph dedicated to the search for extrasolar planets with a resolution of 1 m/s or better. This resulted in the "High Accuracy Radial velocity Planet Searcher" (HARPS) being constructed by a consortium led by the Geneva Observatory and installed in 2003 at ESO's 3.6 m telescope at La Silla Observatory in Chile. It is a fiber-fed, cross-dispersed echelle spectrograph with a resolution of $R = 115000$. It covers the wavelength range from 380 to 690 nm in 73 echelle orders from order 89 to 161. The fiber output facet is imaged on the detector, a mosaic of two 2k × 4k CCDs. Each extracted pixel (i.e. after summing up ~ 9 pixels in the cross-dispersed direction) can linearly accumulate more than 250000 counts, allowing for a S/N of 500. The CCDs are arranged with a gap between them, such that one echelle order (number 115, containing 530 to 534 nm) cannot be observed.

To be able to realize the ambitious sensitivity for radial velocity variations, several measures were taken to reduce both systematic and statistic uncertainties. An optimal resolution was chosen according to a carefully determined trade-off between the size of the instrument and telescope, the slit coupling efficiency (i.e. photon noise) and spectral resolution [87]. Together with the wavelength range this determines the photon noise limited repeatability (see sections 2.3 and 2.5). According to equation (2.20), and considering a larger prefactor of ≈ 0.55 (accounting for the spectral range, see [21]), the optimum photon noise limited repeatabiltiy of HARPS

amounts to

$$\sigma_v^{total} \approx 0.55 \left(\frac{500}{500} \right) \left(\frac{1.5 \times 10^5}{1.15 \times 10^5} \right)^{1.5} \text{cm/s} = 0.8 \, \text{cm/s}, \tag{5.1}$$

when calibrating the instrument with a frequency comb that has a mode spacing of 15 GHz. Although being designed for sub-m/s repeatability only, HARPS has the potential of detecting shifts on the cm/s scale, provided that instrumental drifts can be tracked reliably.

Obtaining photon noise limited uncertainty of the stellar spectra requires the elimination of all systematic effects of the detection on that level. The spectrograph is put in a vacuum vessel, evacuated to below 0.01 mbar and temperature stabilized with a long term stability on the order of 0.01 K and day-to-day variations of about 0.001 K [166]. The detector is operated at liquid nitrogen temperature with a resulting stability of ± 0.02 K. However, not only must the instrument be as stable as possible, but the beam entering the spectrograph also must not vary. Therefore the light is fiber coupled and the position of the star's image at the telescope's focal plane is servo-controlled to always be centered with the fiber's input facet. Additionally, a passive fiber scrambler is installed which exchanges the fiber's near and far field to reduce the residual preservation of an asymmetric illumination of the input facet.

With these measures and a generally very stable and robust mechanical design, HARPS has a passive stability of better than 1 m/s over a month [16]. To be able to measure the residual drifts of the spectrograph and to further improve its performance, it is fed by two fibers whose images are separated on the CCD by ≈ 15 pixels in the cross-dispersed direction. In normal operation, one fiber delivers the starlight while the second fiber is continuously fed with calibration light. Any global drift of the instrument is monitored and can be subtracted from the data. With this simultaneous calibration scheme it could be shown that the spectrograph's average drift is on the order of 10 cm/s during approximately an hour and a repeatability of 20 cm/s is feasible, using a Th-Ar lamp for calibration [16].

With HARPS being the most stable spectrograph to date, it is naturally the optimum choice for testing a frequency comb as a calibration source. Twice during the period of this work, in January 2009 and March 2010, we had the chance to be granted highly sought-after observation time at this instrument. The time that we had already spent at the VTT, helped us tremendously in being well prepared for a successful campaign in La Silla. In this chapter, the detailed analysis of the performance of a frequency comb as calibrator for an astronomical spectrograph is presented.
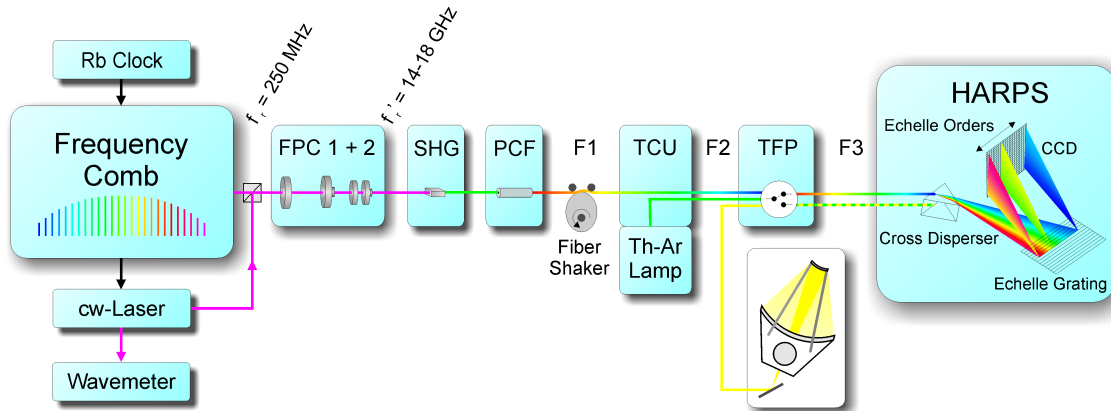
Figure 5.1: *Sketch of the experimental setup of the calibration tests at HARPS. A Yb-fiber based laser frequency comb is filtered with two Fabry-Pérot cavities (FPC 1+2), which results in a mode spacing of f'_r = 14-18 GHz. In the following second harmonic generation stage (SHG) the comb spectrum is frequency doubled to $\approx$ 520 nm. In a photonic crystal fiber (PCF) the spectrum is broadened to more than 100 nm bandwidth and then the light is coupled to a multimode fiber via a fiber collimator. Traversing a fiber shaker, the comb light is fed together with light from a conventional ThAr calibration lamp via the telescope's calibration unit (TCU) through the telescope's focal plane (TFP) to the HARPS spectrograph. F1, F2 and F3 refer to the fibers between the different units, which have a core diameter of 1 mm, 300 μm and 70 μm, respectively. At the TFP, apertures can be set, such that light coming from any of the F2 fibers or the telescope can be coupled to any of the F3 fibers. Fiber amplifiers situated before, between and directly after the FPCs are not illustrated. They compensate for the power losses due to the rejected modes of the filter stages.*

5.2 Calibrating HARPS with a frequency comb

The individual components of the frequency comb that we used in La Silla were described in chapter 3. An overview of the complete system is depicted in figure 5.1. The general concept of the comb system employed in 2009 and 2010 is identical, but of course it was refined in between the two campaigns. The spectral broadening after the SHG stage was only implemented in 2010. Both systems are described in detail, since different measurements were performed in the two campaigns.

5.2.1 The frequency comb system of the 2009 campaign

The frequency comb is based on a Yb-fiber oscillator with a fundamental repetition rate of f_r = 250 MHz (for details see section 3.3). The laser is operated in the dispersion-managed regime, giving a spectral bandwidth of $\approx$ 50 nm. The fourth harmonic of the repetition rate is phase-locked at 1 GHz to a low noise RF synthesizer, which is referenced to a Rb clock. The atomic clock is the same one that we
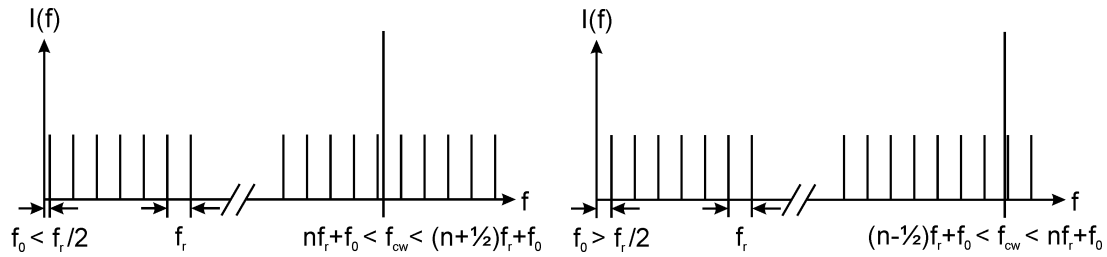
Figure 5.2: *Two (of four) possible states of the offset frequency relative to the repetition rate and the position of the cw laser (at frequency f_{cw}) relative to the comb. The state of the cw laser can be determined by increasing f_r and observing in which direction the beat between the cw laser and the comb moves. When the state of the cw laser is known, the modulus of the offset beat can be increased, and observing the change of the beat with the cw laser will reveal the state of the offset frequency.*

used at the VTT and has an accuracy of 5×10^{-11} (1.5 cm/s). The offset frequency, detected with the f-$2f$ interferometer (described in section 3.4), is locked at 20 MHz to another synthesizer which is referenced to the Rb clock as well.

In the 2009 campaign, the oscillator was a breadboard setup without pre-installed long-term stabilization. Any drift of the oscillator length due to changes in temperature, air pressure or humidity causes the servo of the repetition rate to walk out of its locking range. A high power resistor is thus mounted on the breadboard as a heat source to allow for a long-term cancellation of oscillator length changes. To prevent the offset frequency from drifting out of its locking range, the position of a wedge in the oscillator can be tuned.

An external cavity diode laser (Toptica DL pro) is locked onto a mode of the comb with zero offset (see section 3.6). The servo signal is fed back to the pump current of the laser, while a piezo, acting on a grating angle inside the laser, is used to compensate for long-term drifts that exceed the locking range of the fast servo. The cw laser is used for several purposes. First, the mode number of the comb mode to which it is locked can in principle be determined. A wavemeter (HighFinesse WS/7) with a nominal absolute accuracy of 60 MHz is used to measure the wavelength of the cw laser, which should be sufficient to resolve the 250 MHz ambiguity given by the repetition rate. The specified accuracy, however, is only maintained when the wavemeter is calibrated regularly and hence it could not be trusted after being shipped half way around the world. The mode numbers of the filtered comb lines were thus determined from a comparison with a Th-Ar calibration of HARPS which is accurate at the 20 to 50 MHz level (see section 5.6). Still, monitoring the frequency of the cw laser with the wavemeter ensures that the same mode is always transmitted through the FPCs, as the wavemeter has a stability and resolution of 10 MHz.

The second application of the cw laser is determining the sign of the offset frequency f_0. More accurately, as f_0 is detected via a beat note, there is an ambiguity

between f_0 and $f_r - f_0$, which needs to be resolved. In figure 5.2, it is shown how this can be done by looking at the beat between the comb and an additional cw laser, which itself has the ambiguity of being closer to either the next lower or higher frequency comb mode.

The third purpose of the cw laser is that the length of the FPCs can be stabilized with the cw laser. In 2009, the cw laser was spatially overlapped with the comb light after the first and before the second amplifier with a polarizing beam cube. In this way, the cw laser was amplified together with the comb signal and, after passing through an isolator that followed, it could no longer be separated from the adjacent comb modes. Both FPCs were tilt-locked to the reflected higher order mode of the cw-laser (see section 3.6 for a discussion of this method and related issues). The cw laser is tuned to $\sim 1050\,\text{nm}$, to be at the edge of the amplified spectrum, which reduces the undesired influence of the reflected comb light on the error signal.

The first cavity was set to a filter ratio of $m_1 = 8$, and generated a $2\,\text{GHz}$ mode spacing, while the second cavity was set to $18\,\text{GHz}$ ($m_2 = 9$). This is slightly higher than the theoretical optimum spacing but it had the advantage of well-separated lines, which facilitated the analysis. The cavity mirrors have a reflectivity of $99.2\,\%$, giving a finesse of $\mathcal{F} \approx 390$ for both cavities. Long term drifts of the FPCs can be compensated with a second piezo actuator with a large travel range.

A total of four core-pumped amplifiers was used in series. The first amplifier was pumped by three pump diodes delivering up to a total of $1.5\,\text{W}$ at 974 and $980\,\text{nm}$. It amplified the output of the oscillator to more than $600\,\text{mW}$, of which $500\,\text{mW}$ were used for the f-$2f$ interferometer and $\sim 100\,\text{mW}$ were fed (together with the cw laser) into the second amplifier. This was pumped by two diodes and could deliver up to $500\,\text{mW}$. With a filter ratio of $m = 8$, $87.5\,\%$ of the light were reflected from the first FPC, and when including mode matching losses and the transmission of other elements (e.g. an isolator), only $30\,\text{mW}$ remained that were then fed into the third amplifier. This was pumped by only one diode and delivered $300\,\text{mW}$ to the second FPC, which had approximately the same loss as the first. Consequently, $15\,\text{mW}$ were coupled to the last amplifier, that was pumped again by one diode and finally reamplified the comb light to $\sim 300\,\text{mW}$. The first amplifier consisted of $\sim 30\,\text{cm}$ of highly doped, non-polarization maintaing gain fiber (Yb2000-4/125), two collimators with a $10\,\text{cm}$ fiber pigtail and $\sim 50\,\text{cm}$ of a specialty fiber from OFS, which had negative third order dispersion. This proved helpful to be able to compress the pulses to $< 60\,\text{fs}$ for the f-$2f$ interferometer. The other amplifiers consisted only of a short piece (15-20 cm) of the same gain fiber. The light was coupled in and out of the fiber via aspheric lenses and the pump light was spatially overlapped with the signal either via a dichroic mirror (first and second amplifier) or a polarizing cube (third and fourth amplifier).

After traveling through a total of about $1.5\,\text{m}$ of fiber and various optical components, the pulses were compressed before frequency doubling them. An identical compressor as in the f-$2f$ interferometer was used, consisting of two highly efficient

transmission gratings. Pulse durations of $\sim 200\,\mathrm{fs}$ were obtained with an average power of $200\,\mathrm{mW}$ at $18\,\mathrm{GHz}$ repetition rate. A periodically poled potassium titanyl phosphate (PPKTP) was employed as frequency doubling crystal. Less than $1\,\mathrm{mW}$ of light was generated with a central wavelength of $514.9\,\mathrm{nm}$ and a FWHM of $2.1\,\mathrm{nm}$, limited by the crystal's phase matching bandwidth. The conversion efficiency was low, mainly because there had been no time left for optimizing it before the observation period began. It would have been possible to still tune several parameters to increase the efficiency, including the pulse length, the focus size or the crystal temperature. On the other hand, there was no use for more light, as the light was subsequently coupled to the spectrograph, and with several microwatts of total power, the strongest comb lines could already saturate the detector during a typical $80\,\mathrm{s}$ exposure.

5.2.2   The frequency comb system of the 2010 campaign

In 2010, a commercial Yb-fiber laser (Menlosystems Orange 250) was employed, which was developed, based on the design of the home-built lasers. The repetition rate was again $250\,\mathrm{MHz}$ and the laser was operated in the dispersion-managed regime as well, producing comparable spectra. Locking the repetition rate and offset frequency was also done in the same manner and to the same Rb clock. Long term stability was ensured by a temperature stabilized oscillator and an additional stepper motor could be used to counteract residual length changes. The same wedge was used to counteract the long term drift of the offset frequency.

The cw laser was also the same as well, operated at $1059\,\mathrm{nm}$, i.e. in the center of the amplified spectra. It was split up and spatially overlapped with the comb light directly in front of both FPCs with a polarizing beamsplitter cube. In this way, the cw laser could be separated from the comb after the cavities with another polarizing cube. This was important, because the cavities were locked on the transmission signal via the transmission-PDH scheme, as the tilt-lock to the cw laser suffered from the rejected comb modes. Furthermore, by coupling the laser to both filter cavities individually, they could both be stabilized independently from each other and also independently from the comb.

The mechanical setup of the FPCs was refined, leading to more robustness versus environmental distortions. The cavity mirrors, however, were the same, and the first cavity was again set to a $2\,\mathrm{GHz}$ spacing, while the second cavity was set to various spacings between 14 and $18\,\mathrm{GHz}$ during the tests.

One major difference between the setups in 2009 and 2010 were the fiber amplifiers. In the system of 2010, the output of $\sim 200\,\mathrm{mW}$ of the oscillator was directly split up into two parts. The smaller fraction of about $30\,\%$ was used for the f-$2f$ interferometer and was amplified separately with a non-polarization maintaining, core-pumped amplifier to approximately $500\,\mathrm{mW}$. The larger part of about $70\,\%$ was coupled to a double-clad amplifier, which was pumped by two multimode pump

diodes emitting up to 8 W at 974 nm. The comb light was amplified to 2 W with the pumps at half their maximum power. After the first cavity, 20 mW were coupled to the second amplifier, which was identical to the first one. Thus, 2 W were also coupled to the second FPC and the same 20 mW to the third amplifier, which was the power amplifier. It was pumped by up to six multimode pump diodes and delivered at maximum a power of 12 W. In the first and second amplifier a gain fiber with 10 μm core diameter was used, while in the power amplifier optionally a 10 μm or a 6 μm fiber was employed. All fibers in the amplifier system are polarization maintaining. To prevent pulse break-up due to nonlinearities, 20 m of passive fiber were inserted in front of the first amplifier. Further details of the amplifiers are described in section 3.5.

In total, the pulses traveled through roughly 50 m of fiber and a specially designed compressor had to be be used to obtain transform-limited pulses. In a simple grating compressor, the ratio of GDD to TOD is always negative. Unfortunately, the same is also true for standard silica fibers and thus a pulse will accumulate a third order chirp. For the re-compression of pulses after traveling through long fiber sections, combinations of prims and gratings have been proposed [129, 167]. By tuning the distance and angle of the prism sequence inside the grating pair, the value of the GDD to TOD ratio and even its sign can be changed. Further details are described in appendix B. Using only a simple grating compressor, pulses with an autocorrelation width of ~ 400 fs were obtained. By compensating also the TOD, the pulses could be compressed to a FWHM pulse width of 100 fs which is close to the transform-limit of 90 fs. The coupling efficiency of about 80 % was achieved by the use of transmission gratings and Brewster-cut prisms to minimize losses.

In contrast to 2009, different SHG crystals were tried and the coupling optimized. PPKTP was no longer considered because it was limiting the spectral bandwidth. Potassium niobate (KNbO$_3$) had to be dismissed for the same reason, although a maximal conversion efficiency of about 15 % could be obtained. The phase-matching bandwidth of lithium triborate (LBO) and beta barium borate (BBO) can be > 5 nm for the frequency doubled light for reasonable crystal lengths < 5 mm and will thus not limit the spectral bandwidth. Conversion efficiencies of 7.5 % (BBO) and 4 % (LBO) could be achieved, but a trade-off had to be made between intensity and beam profile, as the light was coupled to a single-mode PCF afterwards. BBO crystals leads to a strongly astigmatic beam, while LBO maintains a good beam profile. This effect outweighs the conversion efficency and thus LBO was used although only a power of 300 mW could be generated with the available crystal. The FWHM spectral bandwidth was 6 nm at a central wavelength of ≈ 526 nm. By detuning the compressor and driving the SHG with chirped pulses, a FWHM of up to 11 nm could be achieved at the prize of a largely reduced efficiency. This has been important for calibrating the spectrograph with maximally broad spectra without using a nonlinear fiber.

In a final step, which was not yet developed in 2009, the pulses were coupled into

a tapered, microstructured fiber to broaden the spectrum. Up to 100 nm bandwidth at 20 dB below the peak could be achieved with pulse energies of only 2.7 pJ. Further details of the spectral broadening are described in section 3.7.

5.2.3 Coupling the frequency comb to HARPS

The light of our frequency comb system was coupled to HARPS via those fibers, which in normal operation are used to deliver the calibration light of the Th-Ar lamp to the spectrograph. After the SHG stage or alternatively after the PCF the comb light was coupled to one or two multimode fibers (F1) with 1 mm diameter, guiding it to the calibration unit of HARPS. This is a rack, in which several lamps are installed, e.g. Th-Ar lamps for calibration or white-light sources for taking pixel sensitivity maps (flat fields). At the calibration unit, optics are installed that are designed to focus the light of two lamps onto two fibers (F2), bringing the calibration light to the telescope. Both fibers F2 have a diameter of 300 μm and the optics have a demagnification of 10:1. The same optics were used to couple the comb light from F1 to F2, projecting the comb light onto a 100 μm spot on the input facet of the F2 fibers. Each of these then projects a spot of 750 μm diameter on the telescopes focal plane (TFP). The projected light is collected by one of the two fibers (F3) with a diameter of 70 μm, that bring the light to the spectrograph. At the TFP, light from each of the F2 fibers or starlight from the telescope can be coupled to any of the F3 fibers. The images of the two fibers on the CCD are termed channel A and B respectively. In the path to the spectrograph, a passive optical scrambler exchanges the F3 fiber near-field and far-field to reduce the effect of an inhomogeneous illumination of the input facet of F3. For our calibration tests, another scrambler was attached to F1 which actively shook the fiber to destroy the coherence (see section 5.4).

5.3 Data reduction

A plot of the raw data from part of the two CCD chips is shown in figure 5.3. These files must be processed to obtain a one-dimensional dependency of a count rate on the pixel number. First, the count rate originating from the readout electronics (termed "bias") and its noise is measured, so that it can be subtracted from the data. In a second step, the dark count rate during an exposure and the event rate of cosmic rays hitting the detector is calculated. Next, the geometric form of the orders on the CCD is determined by evaluating an illumination with a white light source. A fourth order polynomial is derived for each order to describe its center position along the chip. To determine pixel-to-pixel sensitivity variations (encoded in a "flat field") as well as the overall sensitivity curve of the individual orders (its "blaze"), the same white-light illumination is evaluated. The one-dimensional spectrum is
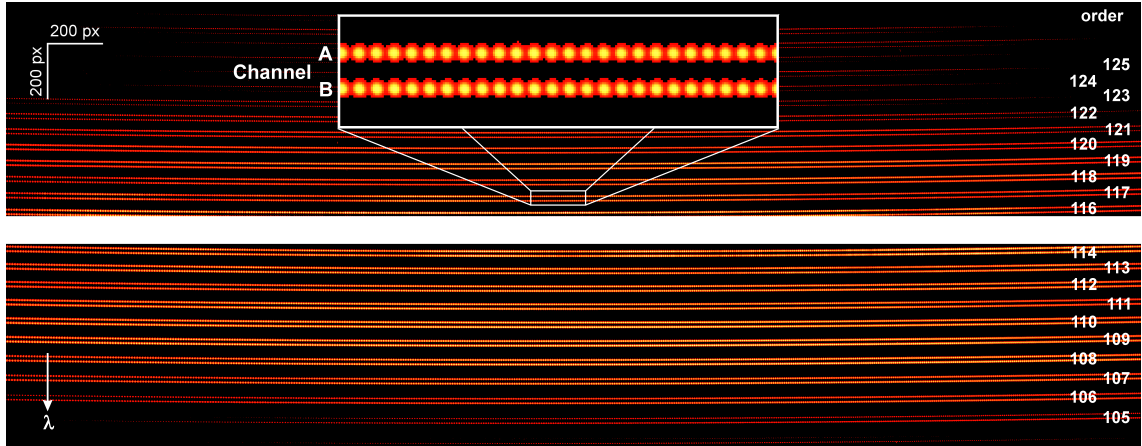
Figure 5.3: *Raw data of one acquisition with HARPS. Two 4096×750 pixel sections on both CCDs are shown, containing 13 echelle orders of the broadened comb on the upper, short wavelength CCD and 10 orders on the lower, long wavelength CCD in both channels A and B. In between the two CCDs, one order is lost completely and the longest wavelength order on the upper CCD is cut in channel B. The gap between the two channels is ∼ 17 pixel and between two orders ∼ 55 pixel. Throughout the two CCDs the gap between the orders varies between 35 pixels at the blue end of the spectrum and 100 pixel at the red end. The residual curvature of the orders on the CCD derives from the geometry of the cross-disperser. The inset shows a 200 × 50 pixel section of order 117. The mode spacing of the comb was set to $f_r = 12$ GHz in this acquisition.*
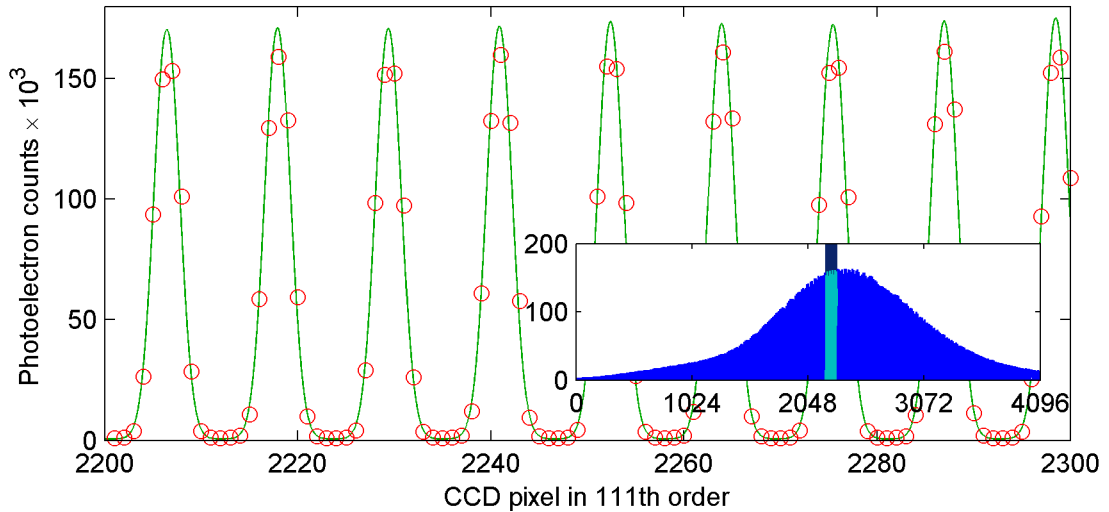

Figure 5.4: *Frequency comb calibration spectrum. A part of the extracted spectrum (red circles), containing nine comb modes with a spacing of $f_r = 18$ GHz, is shown together with a sum of Gaussians fitted to the data (green). A single, 80 s exposure was integrated to arrive at the given photoelectron count rates. The inset shows one full echelle order (out of 72) with the comb's spectral envelope. The range of the zoomed region is highlighted.*

then extracted, using the algorithm developed by Horne [168], but first the bias is subtracted and afterwards the spectrum is divided by the flat field. For each echelle order, a dataset of 4096 counts versus pixel pairs is saved in photoelectron units.

The dispersion of the CCD is roughly 1.6 GHz per pixel, corresponding to about one third of the resolution. A single comb mode is therefore projected onto ~ 8 pixels with a distribution given by the point-spread-function (PSF) of the spectrograph. The center of the line and an estimate of its uncertainty can be derived from a fit to the data. The fit function should ideally be the PSF, but this is unknown and also cannot be easily derived, as it is not constant throughout the whole spectrum. On the other hand, it is uncritical whether the proper PSF is fitted to the data or any other function, as long as it is the same function during the whole observation period for all related data. Should the fit give an incorrect value for the center of a calibration line, then it will make the same error when deriving the position of a signal. Determining the drift of the instrument is in any case independent from the absolute position of a calibration line. A Gaussian is a good approximation of the instrument's PSF and is thus chosen as the function to be fitted to each line. In figure 5.4, a 100-pixel section of the extracted spectrum is shown with nine comb modes. There is reasonable agreement between the count rate and a Gaussian fit, weighted with Poissonian noise and a small, additional contribution of readout noise. The peak value is about 7 % too high throughout the spectrum and the line center seems to be slightly off, as the PSF is not exactly a Gaussian.

Various parameters of the fit algorithm were varied to exclude their effect on the results. For example, different fit functions, such as Lorentzians or Gaussians with a non-quadratic exponent, were investigated. Both, individually fitted lines or a fit to the sum of all lines were tested. For the individually fitted lines, the size of the fit window was varied and the dependency on a non-zero offset as a parameter was studied. None of these tests showed significant shifts of the line position, i.e. they agreed within the statistical uncertainty.

5.4 Impact of multimode fiber coupling

A spectroscopic measurement with a grating spectrograph is essentially a geometric measurement, as already mentioned in section 2.1. The distribution of the signal spectrum on the detector is compared with a calibration spectrum via an interpolating function, i.e. the calibration curve. If only a drift between two identical spectra needs to be measured, the calibration curve does not need to be computed explicitly. Instead, its smoothness is implicitly assumed — which is not guaranteed as will be shown in the section 5.6. The accuracy of the measurement depends on the spatial overlap of the signal and calibration light. Any deformation of one wavefront with respect to the other will lead to a systematic error.

For the sake of efficiency, multimode fibers must be used to couple starlight from

the telescope to the spectrograph (see section 2.3). As its name implies, many spatial modes are guided by a multimode fiber. The number M depends on the fiber's numerical aperture NA (determined by the fiber geometry and the difference in refractive index between core and cladding), the wavelength λ and the core diameter a [120]

$$M \approx 16 \left(\frac{a}{\lambda} \text{NA} \right)^2 . \tag{5.2}$$

Typically, the NA of a fiber is $0.2 - 0.5$ and thus a fiber with a $70\,\mu$m core guides about $10^4 - 10^5$ modes at $500\,$nm. In an ideal fiber, the modes are orthogonal and there is no coupling between them. The initial occupation distribution of the fiber modes, defined by the incident electric field at the input facet, is preserved and there would be no hope of perfectly matching the modal profiles of signal and calibration light. In a real fiber, however, the modes are coupled due to variations in the fiber geometry or scattering at impurities. An initially asymmetric distribution of the modes is smoothened during propagation. Still, a residual sensitivity to the coupling at the input facet can remain.

This problem was recognized soon after the development of high-resolution, fiber-fed spectrographs [169]. Two solutions to this problem have been put forward. Either the occupancy of the modes can be homogenized inside the fiber by actively moving and bending it [86] or the input illumination can be stabilized and homogenized [170]. The latter is realized at the HARPS spectrograph. First, the input illumination of fiber F3 is stabilized by actively controlling the telescope's alignment to center the image of the star on the fiber core. Second, at the interface to the vacuum chamber of the spectrograph, an optics assembly is installed that interchanges the the fiber's near and far field when coupling the light into a short piece of the same fiber inside the chamber [87].

When sending first comb light to HARPS in 2009, the repeatability of the calibration was surprisingly bad. The measured uncertainty of the drift on a single acquisition was $1.1\,$m/s and therefore a factor of six above the photon noise limit (see next section). Only after continuously moving and bending the fiber during the exposure time did the repeatability improve (see figure 5.5). So, obviously, the calibration with a frequency comb is more sensitive to the mode occupancy in a fiber than traditional calibration methods or starlight.

The light of the frequency comb differs from that of spectral lamps or starlight in one key property: while the latter are incoherent sources, a frequency comb emits coherent light. In fact, as long as the servo loops for phase stabilization don't "lose" a cycle, a comb has an infinite coherence length. Due to the coherence of the comb light, different spatial modes in a fiber will interfere on the detector resulting in a complex pattern. The more modes contribute to the interference pattern, the finer its structure will be, and in any case, it is very sensitive to the exact occupancy distribution. Starting from a single Gaussian mode out of the PCF, the comb light will occupy only few modes when coupling it to the multimode fiber. The way
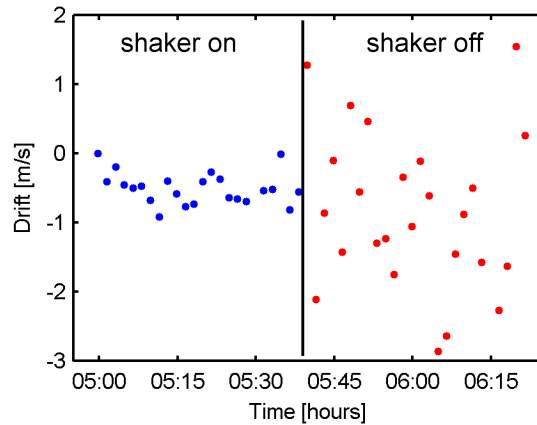
Figure 5.5: *Calibration repeatability with (blue) and without (red) an active fiber mode scrambler. A series of 48 acquisitions of a comb with $f_r = 12\,GHz$ is taken and after 23 acquisitions, the dynamic scrambler is switched off. The standard deviation of a single acquisition is 23.5 cm/s with scrambling and 114 cm/s without.*

the calibration light is delivered to the spectrograph even enhances the sensitivity to variations of the mode occupancy. At the telescope's focal plane, the image of the comb light coming out of fiber F2 is a $750\,\mu m$ spot on the surface of fiber F3 (having a diameter of only $70\,\mu m$). Hence, only a small fraction of the image is coupled to the next fiber. Since a small variation in the mode occupancy leads to a strong variation in the interference pattern, subsequent vignetting largely enhances the sensitivity to multimode noise.

No static scrambling of the fiber modes can solve this issue, because the coherence is maintained. On the other hand, dynamically redistributing the mode occupancy over time is destroying the temporal coherence and thus a time average of many interference patterns is recorded. Another way of looking at it is that the scrambling increases the mode occupancy of the comb light, at least on time average. The difference between the average wave fronts of subsequent acquisition is thus reduced. For this reason, an active scrambler with a time constant much smaller than the exposure time is employed in the setup. The best performance was obtained, when shaking the fiber with a low amplitude at high frequency (75 Hz). In this way, the systematic shifts can be reduced below detectability and all the data presented in this chapter are recorded with the scrambler in operation.

By the demonstration of a high repeatability, only variations of the mode occupancy between subsequent acquisitions can be excluded. There might still be a constant difference which would lead to an error in the absolute calibration. The inability to perfectly match the wave fronts of starlight and calibration light might ultimately limit the accuracy of the calibration. In a test series, the absolute calibration of one order of HARPS was subsequently determined with and without

coupling the comb through an integrating sphere in front of the multimode fiber. An integrating sphere is a device which destroys coherence very effectively at the cost of a very low transmission. Both calibrations agreed with each other within the statistical uncertainty of $\approx 3\,\mathrm{m/s}$. Improving on the uncertainty of this measurement is mandatory to check, whether differences in the absolute calibration are detectable on the cm/s-level.

5.5 Calibration repeatability

5.5.1 Repeatability of the unbroadened comb calibration

The repeatability of the calibration is determined by taking a long series of subsequent acquisitions and computing the standard deviation of the average drift of the acquisitions with respect to a reference acquisition. With the comb of the 2009 campaign ($f_r = 18\,\mathrm{GHz}$, 2.1 nm FWHM at 515 nm), 362 lines were observed in the order 111. The wider but still unbroadened spectrum of 2010 fully covered order 113 (the reddest on the short wavelength chip), as well as the two orders 114 and 115 which are (partially) lost in the CCD gap. Wings of the spectrum were detected in order 112 an 116 (the later being the bluest order on the long wavelength chip).

A reference acquisition is arbitrarily chosen and the difference between each line in the acquisition of interest and the reference is computed in pixel units. According to the known frequency of each line, the pixel difference is converted into a shift in units of radial velocity. The average line shift of the acquisition of interest is then computed, weighted with the uncertainties of the fitted line positions. The scatter of these average drifts during a series of acquisitions, measured by the standard deviation, gives the calibration repeatability of one acquisition.

When observing cosmic objects, channel A is fed with starlight, while channel B is fed with the calibration light to eliminate instrumental drifts. In a calibration test, both channels contain calibration light, i.e. either comb light or light from a Th-Ar lamp. A shift of the spectral lines of the Th-Ar lamp is determined by a different method than fitting each line individually. Instead, an algorithm described by Bouchy et al. [171] is used. For small shifts in radial velocity, the dependency of the change in intensity at a given pixel on the line shift can be linearized. No fit procedure is necessary, not even a well defined line. For each echelle order, one value for the average drift of the spectrum is derived directly and the repeatability is again computed from the scatter of a series of acquisitions. While this method works nicely for Th-Ar calibration spectra, it fails for the comb light. The reason is that it cannot tolerate relative intensity fluctuations within a spectrum, that are not related to line shifts. Such spectral deformations can be excluded for spectral lamps or star spectra, but the spectral envelope of a laser can very well vary with environmental changes (without inducing a frequency shift of the individual modes, of course).

Fluctuations of instrumental origin or in the fiber coupling will lead to an additional scatter of the average drift which is, a priori indistinguishable from photon noise when looking only at one channel. Computing the difference between the two channels, however, removes drifts of the spectrograph because they are common mode, as long as there is no drift of one channel with respect to the other. At some unknown level, however, the repeatability will be limited, because drifts can no longer be faithfully monitored by the second channel either due to relative drifts between the two channels or variations in the mode matching in the fiber. In this case, a difference between the best achievable repeatability and the photon noise limit will be detectable. For the next generation spectrographs, this level must be proven to be below $1\,cm/s$. The main purpose of the calibration tests performed with the HARPS spectrograph is thus to determine at which level the repeatability fails to be photon noise limited, if this limit is even detectable.

The photon noise limited repeatability of the comb calibration is derived with the help of equation (2.19), which gives the minimum uncertainty of a single line. For each line, the FWHM, S/N and sampling rate $1/n$ can be computed individually from the fit. The S/N, related to the number of detected photons, can be calculated by knowing the quantum efficiency (QE) of the detector at the corresponding wavelength. In general, $QE > 70\,\%$ for the spectral range between 390 and $700\,nm$. To give an example, at $515\,nm$, the spectrograph's resolution leads to a FWHM of $\sim 2.5\,km/s$ of a single line which is sampled with $3.1\,pixels$. In a single exposure, a S/N of 500 can be achieved without saturating the detector. With 450 lines (i.e. $f_r = 14\,GHz$) at full intensity, the photon noise limited repeatability is $5.5\,cm/s$ when averaging over the whole echelle order. For the measured spectrum, the S/N is computed for each line individually and the photon noise limited uncertainty when averaging over N lines in the calibration is given by

$$\sigma_{total} = \sqrt{\frac{1}{\sum_{i=1}^{N} \frac{1}{\sigma_i^2}}}, \tag{5.3}$$

Figure 5.6 shows that the repeatability of a single line is indeed close to the photon noise limit. Instrumental drifts can still be neglected at this level.

In the first tests after setting up the comb system in 2009, the repeatability was only about $120\,cm/s$ per exposure, which is far above the photon noise. Subtracting the instrumental drift, derived from the simultaneous calibration with Th-Ar light, did not improve the situation and some systematic effect was limiting the calibration with the comb. The solution was to employ the active scrambler at the fiber, that guides the comb light to the calibration unit, as discussed in the previous section. By using the scrambler, this dominating, systematic effect can be reduced below detectability, i.e. photon noise.

To determine the repeatability of HARPS with the comb calibration, a series of 50 acquisitions with an integration time of $80\,s$ is recorded with comb light in channel
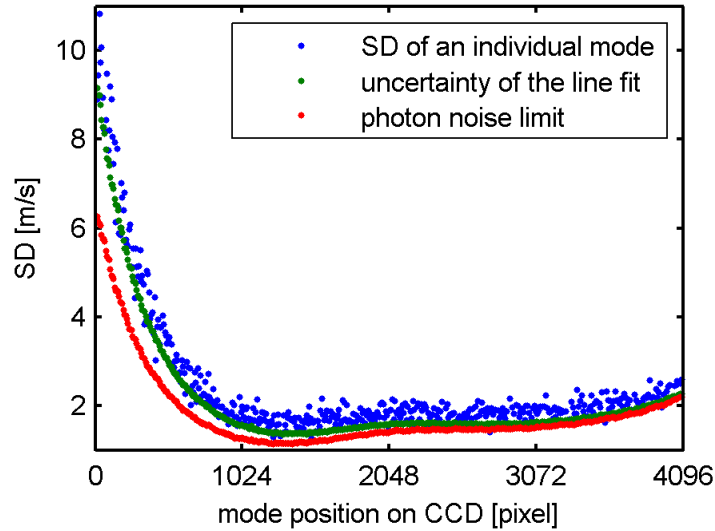
Figure 5.6: *Repeatability of a single comb line. 76 acquisitions of the comb are averaged and the standard deviation (SD) of the measurement of each mode's position is depicted. It agrees well with the uncertainty of the Gaussian line fit, given by the diagonal element of the covariance matrix. The repeatability is close to the photon noise, which is calculated from the accumulated photoelectron counts of each line.*

B and Th-Ar light as a reference calibration in channel A. The photon noise for the whole spectrum that is used for the calibration amounts to 15 cm/s for the comb light and 9 cm/s for the Th-Ar light. It is important to note that the comb only illuminates one echelle order (with the FWHM of the spectrum covering only half of the order), while all lines detectable with the 72 orders of HARPS are employed to derive the Th-Ar calibration. In figure 5.7, the average line shift of the comb and Th-Ar calibration are plotted over the time of acquisition. The repeatability of each channel individually is above the photon noise, indicating instrumental drifts. Calculating the difference of both channels results in a reduced standard deviation (instead of an increased value if the measurements were independent), compatible with the estimated photon noise (which adds up quadratically). This presents clear evidence that common, instrumental drifts are eliminated and no systematic effect is limiting the calibration at this level. The photon noise limited repeatability of this calibration is 15 cm/s, which matches the calibration with Th-Ar lamps [16], but using only one instead of 72 echelle orders.

In 2010, the calibration tests were repeated with a wider spectrum and denser mode spacing ($f_r = 14\,\mathrm{GHz}$, 11 nm FWHM at 526 nm), which results in 456 usable lines in order 113 and 114 and ~ 200 lines in order 112. With these values, the photon noise limit on the repeatability is 9.2 cm/s after taking the difference of both channels. Obviously, in this case a calibration with a Th-Ar lamp would limit the test
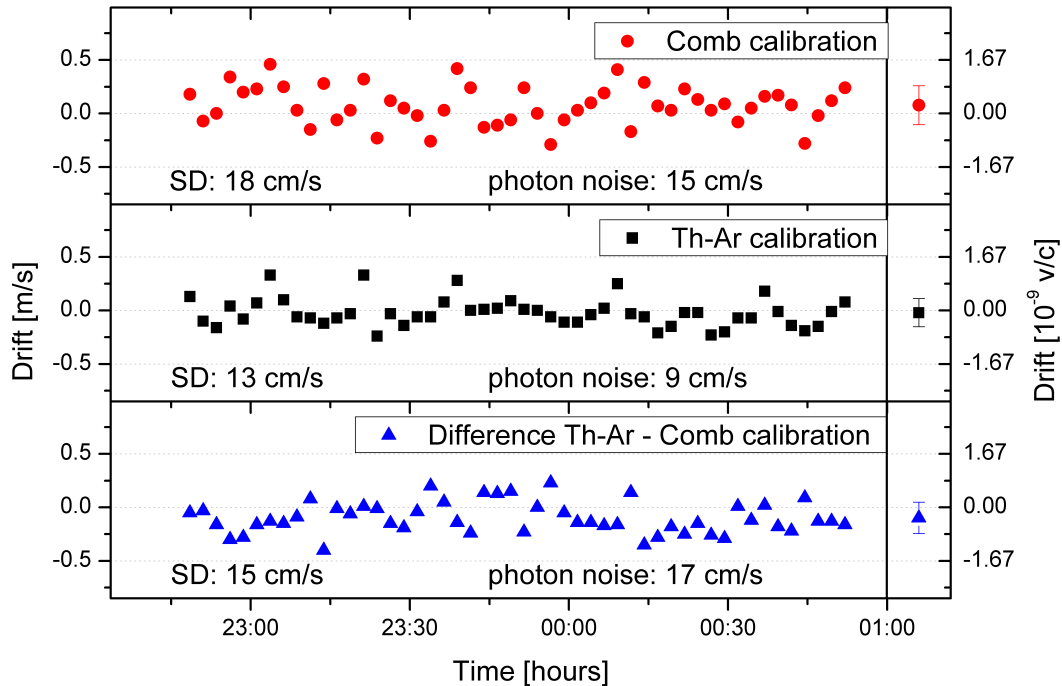
Figure 5.7: *HARPS calibration repeatability of a calibration with an unbroadened comb versus a Th-Ar calibration. Top panel: average line shift data for the comb calibration as a function of time. The drift is measured with respect to an arbitrarily selected reference acquisition (recorded at time 23:54). Mean and standard deviation (SD) are shown separately on the right-hand side. Middle panel: the same for the simultaneous Th-Ar calibration. Bottom panel: the difference of both calibrations. This results in a cancellation of common fluctuations of instrumental origin, which leads to a slightly reduced SD of these data as compared to the comb data. For the comb calibration, only order 111 was used, whereas for the Th-Ar calibration all 72 orders have been averaged. Still, the repeatability of a calibration with a frequency comb reaches the Th-Ar based value.*

for systematic effects with its higher photon noise limit. The reference calibration is therefore performed with the frequency comb too and the results of this calibration test are depicted in figure 5.8. The instrumental drift is as strong as in 2009, since the repeatability per order is again $\sim 18\,\mathrm{cm/s}$. Removing it by calculating the difference between the two channels leads to a photon noise limited repeatability of $10.2\,\mathrm{cm/s}$, which is a factor of about two better than any previous calibration of an astronomical spectrograph. At this level, there are still no systematic effects evident.

The statistic uncertainty can always be reduced by increasing the amount of data until, at some level, systematic effects are again limiting the repeatability. Computing, for example, the average drift of two or more subsequent acquisitions lowers the photon noise of the combined acquisition at the cost of increased detector noise and increased susceptibility to relative drifts between the channels. As long as
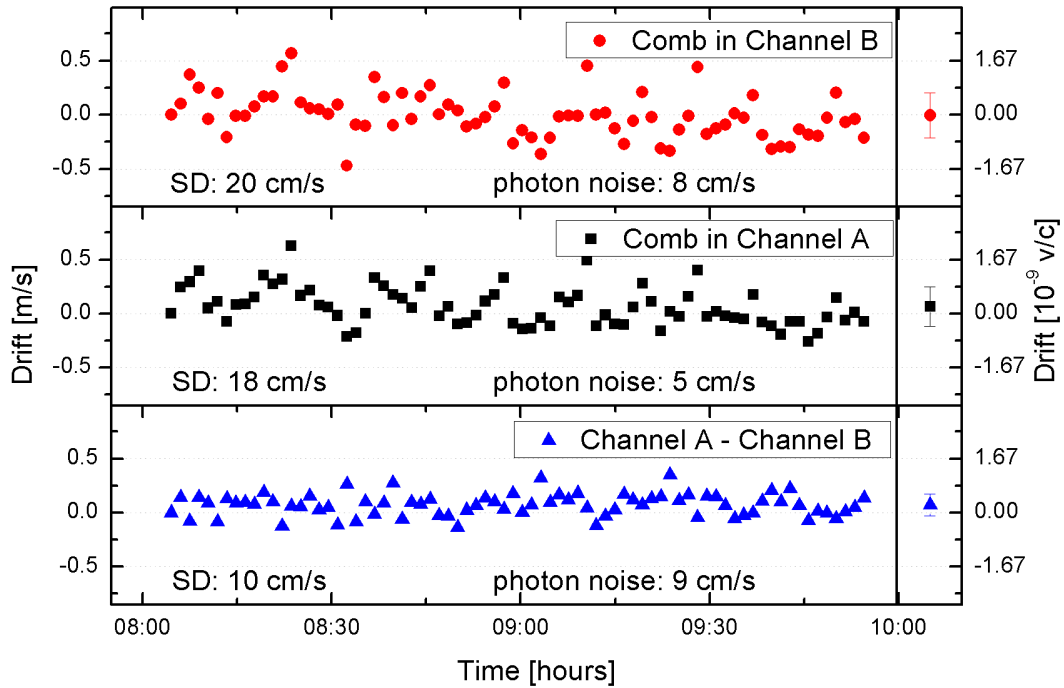
Figure 5.8: *Same as figure 5.7 but with two comb calibrations. A series of 76 acquisitions with 80 s integration time is recorded with unbroadened comb light in both channels. In channel A, orders 112 to 114 are evaluated and in channel B only order 112 and 113 as order 114 is lost in the CCD gap. Top panel: average line shift data for comb calibration in channel B as a function of time. The drift is measured with respect to an arbitrarily selected reference acquisition (recorded at time 08:04). Mean and SD are shown separately on the right-hand side. Middle panel: the same for fiber channel A. Bottom panel: The difference of both calibrations, which demonstrates that the instrumental drift is eliminated and the calibration is at the photon noise limit of 9 cm/s.*

the photon noise is dominating, however, the standard deviation over all acquisitions should decrease with the square root of the number of averaged acquisitions. As shown in figure 5.9, no systematic effects seem to be limiting the calibration of the HARPS spectrograph down to the 2 cm/s level. Averaging over all 76 acquisitions of the series results in a photon noise limit of 1.0 cm/s.

This measurement is an indication that the simultaneous calibration scheme does not suffer from systematic effects on the 2 cm/s level. For astronomical observations, however, it must be emphasized that in practice it is not always easily possible to average over several acquisitions to reduce the uncertainty. Observation time is precious and for a project such as mapping the expansion history of the universe, many quasars must be observed to reduce the sensitivity to systematic shifts of one particular object.
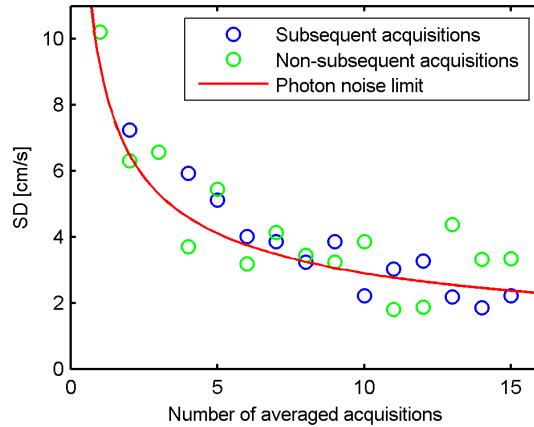
Figure 5.9: *Increasing the repeatability by combining several acquisitions to one larger dataset. The average drift of subsequent and non-subsequent acquisitions of the series from figure 5.8 is computed. The standard deviation (SD) of the average drifts is plotted against the number of acquisitions that are averaged. Note that as the number of averaged acquisitions increases, the statistics for computing the standard deviation becomes worse. For example, averaging over 15 acquisitions leaves only five samples to compute the SD.*

5.6   Absolute calibration

There are a few applications where it is insufficient to just determine the variation of an object's redshift. The most prominent example (besides solar physics as discussed in chapter 4) is the search for a variation of the fundamental constants. In section 2.2 it was argued that an absolute frequency calibration on the MHz-level would be beneficial to obtain significant results. Moreover, an absolute calibration would enable the comparability of data taken with different instruments or at different epochs. At the end of this section the best absolute calibration of HARPS is presented, but first there are two less demanding yet still very important applications of the absolute calibration, the determination of the comb's mode numbers and the calibration curve.

5.6.1   Identifying the comb modes

According to equation (2.18), the frequency of a comb mode is only determined uniquely if its mode number is known. As described earlier, the frequency of the cw-laser, which is locked on a comb mode, can be measured with a wavemeter to resolve the 250 MHz ambiguity of the fundamental mode spacing. However, the absolute calibration of the wavemeter was insufficient, and besides, it would only serve to determine which of the fundamental modes are transmitted through the FPCs. Since the cw laser is indistinguishable from the comb modes after the SHG stage, it cannot serve to identify the relation between the comb modes' positions
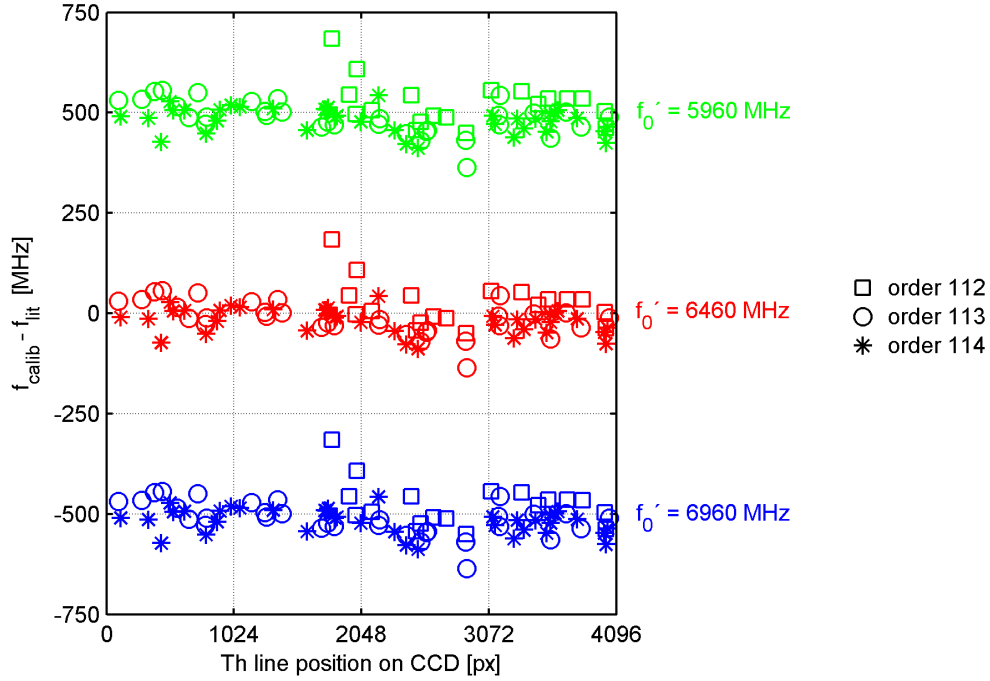
Figure 5.10: *Determination of the mode numbers. Selected thorium lines of high intensity are fitted with a Gaussian and their line centers are compared with the neighboring comb modes, assuming a linear pixel-to-frequency relation between the modes. The differences between the derived thorium frequencies f_{calib} and the literature values f_{lit} of lines in three different echelle orders are plotted for various comb offsets f'_0 under test (in different colors). The uncertainty of all thorium lines is smaller than 100 MHz and thus the fundamental mode numbers can be determined uniquely. The offset frequency of the fundamental comb is locked at $f_0 = -20\,MHz$. Since the comb is doubled in frequency, the ambiguity of the fundamental modes has a 500 MHz spacing and the filtered offset frequency fulfills the relation $f'_0 = 2(nf_r + f_0) = n \times 500\,MHz - 40\,MHz$. The large scatter of the derived thorium frequencies in order 112 is due to the comb having only low intensity.*

on the detector and their corresponding frequencies without further information. Another frequency reference is necessary anyway to perform this task. The Th-Ar spectrum comes in very handy at this point, as it provides calibration lines throughout the whole spectrum with absolute uncertainties of 100 MHz or smaller [99]. It is thus suited not only to resolve the 14-18 GHz ambiguity of the filtered comb lines on the detector but also to determine, which of the fundamental modes are transmitted through the FPCs. In figure 5.10 it is demonstrated that the mode numbers in all three orders, covered by the unbroadened comb in 2010, can be determined uniquely by comparing the positions of the thorium and comb lines on the CCD.
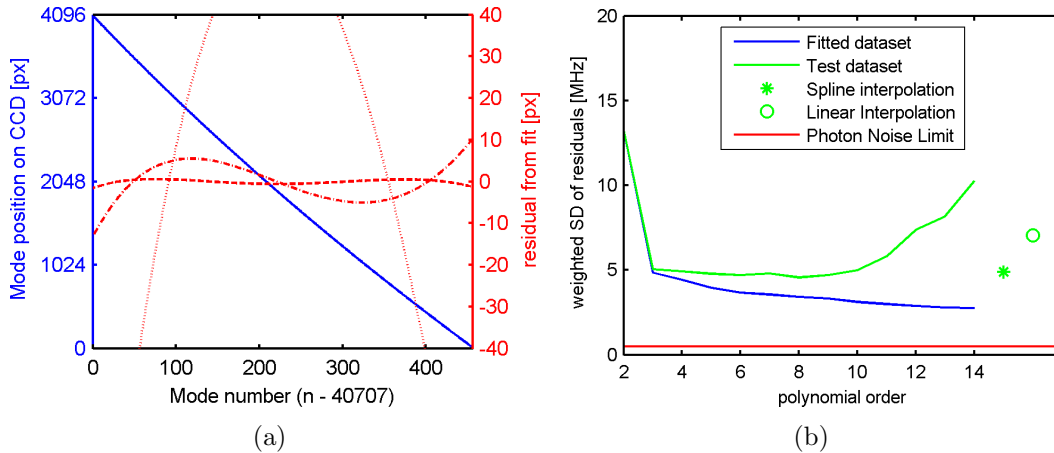
Figure 5.11: *(a) Pixel-to-frequency distribution (blue) and the residuals of a linear ($\cdots$), quadratic ($-\cdot$) and cubic ($--$) polynomial fit (red). 456 modes with a spacing of 14 GHz are detected in order 113. One pixel corresponds on average to a frequency difference of 1.6 GHz. For each of the low order polynomial fits, the distribution of the residuals approximate the next higher order polynomial. (b) Determination of the optimum polynomial order. The mode positions of 76 acquisitions of a calibration with the comb are averaged and every second mode is chosen as a fit dataset and the complementary modes compose a test dataset. Eight piecewise polynomials (one for each 512-pixel section) are fitted to the first dataset and the standard deviation (SD) of the residuals of both datasets is plotted as a function of the polynomial order. Additionally, a linear and a spline interpolation of the fit dataset is evaluated on the test dataset (the residuals on the fit dataset are zero). The photon noise limit is 490 kHz.*

5.6.2 Calibration curve

To derive the variation of an object's radial velocity, a shift of the spectrum needs to be determined. With the spectrograph, only lateral shifts in units of the CCD's pixel size are measured at first. These need to be converted into spectral units, for which the calibration curve — or better yet: its slope — must be known. The same principle which was used to evaluate the VTT data is applied, namely fitting polynomials of increasing order to the pixel-to-frequency distribution. In this way, the calibration curve is modelled by its Taylor series. The expansion can be truncated when the residuals are at the level of the limiting uncertainty of either the line frequencies or positions. In the case of a calibration with a Th-Ar lamp, the uncertainty of the frequencies at the $50 - 100$ MHz level is limiting, while for the frequency comb it is the photon noise on a single line of about 2 MHz (when using only one acquisition).

In contrast to the calibration curve of the VTT spectrograph, the pixel-to-frequency map of HARPS cannot be modelled by a simple, quadratic polynomial. The residuals resemble the next higher order polynomial up until a fourth-order fit,

as depicted in figure 5.11. A fifth-order fit, however, reveals discontinuities that are not compatible with a sixth-order polynomial distribution of the residuals (see figure 5.12). When plotting the residuals over the position of the mode on the CCD, the discontinuities appear at exactly every 512 pixels. Their origin can be attributed to the structure of the CCD, which is written with a 512-pixel mask during manufacturing. At the edges of the mask the size or sensitivity of the pixels can vary. The presence of these imperfections is well known from flat field exposures. Only the frequency comb, however, reveals their impact on the calibration curve. The density of the Th-Ar lines is so low and their frequency uncertainty so large that it only makes sense to use a forth-order fit as a model for the calibration curve. With such a rough calibration, the discontinuities at the edges of the pixel mask remained hidden until now.

With the frequency comb, a much better calibration curve can be derived by including the discontinuities and fitting independent polynomials for every 512-pixel section. The optimum order is determined by choosing a subset of modes and excluding them from the fit. This subset is subsequently used as a test set and the standard deviation of the residuals on the test set is computed with the polynomial under test. The scatter of the residuals on the data set, which is used for fitting, will continuously decrease with increasing polynomial order until all residuals are exactly zero — which occurs when the number of parameters matches the number of modes. On the test set, however, the scatter of the residuals will eventually start to increase again with increasing polynomial order. This is known as "overfitting", i.e. when noise on the fitted data enters the model and its prediction capability deteriorates. The result of this test is depicted in figure 5.11(b). An eighth-order polynomial per CCD section gives the lowest standard deviation of the residuals of the test dataset. The minimum standard deviation is 4.7 MHz, which is an order of magnitude above the photon noise of 490 kHz for the 76 acquisitions, which were averaged to compose the test dataset.

When comparing the comb and Th-Ar calibration curves, local deviations of up to 100 MHz can be found. These systematic errors in the Th-Ar calibration can now be detected with the frequency comb, leading to a significant improvement of the absolute calibration of HARPS. In principle, the spectrograph can now be used to deduce an improved Th-Ar line catalog. However, this measurement would be of little significance, since on this level the exact line positions are dependent on the spectral lamp and its operating conditions [172]. Nevertheless, a highly stable spectrograph in combination with a frequency comb as calibration source can outperform traditional Fourier transform spectrometers and might be a future alternative.

For the calibration curve, derived with a Th-Ar lamp, a low-order polynomial model is a good approximation, as only few lines are available for the fit and each of them has a large uncertainty in its absolute frequency. When using a frequency comb to derive the calibration curve, this situation changes completely. Hundreds
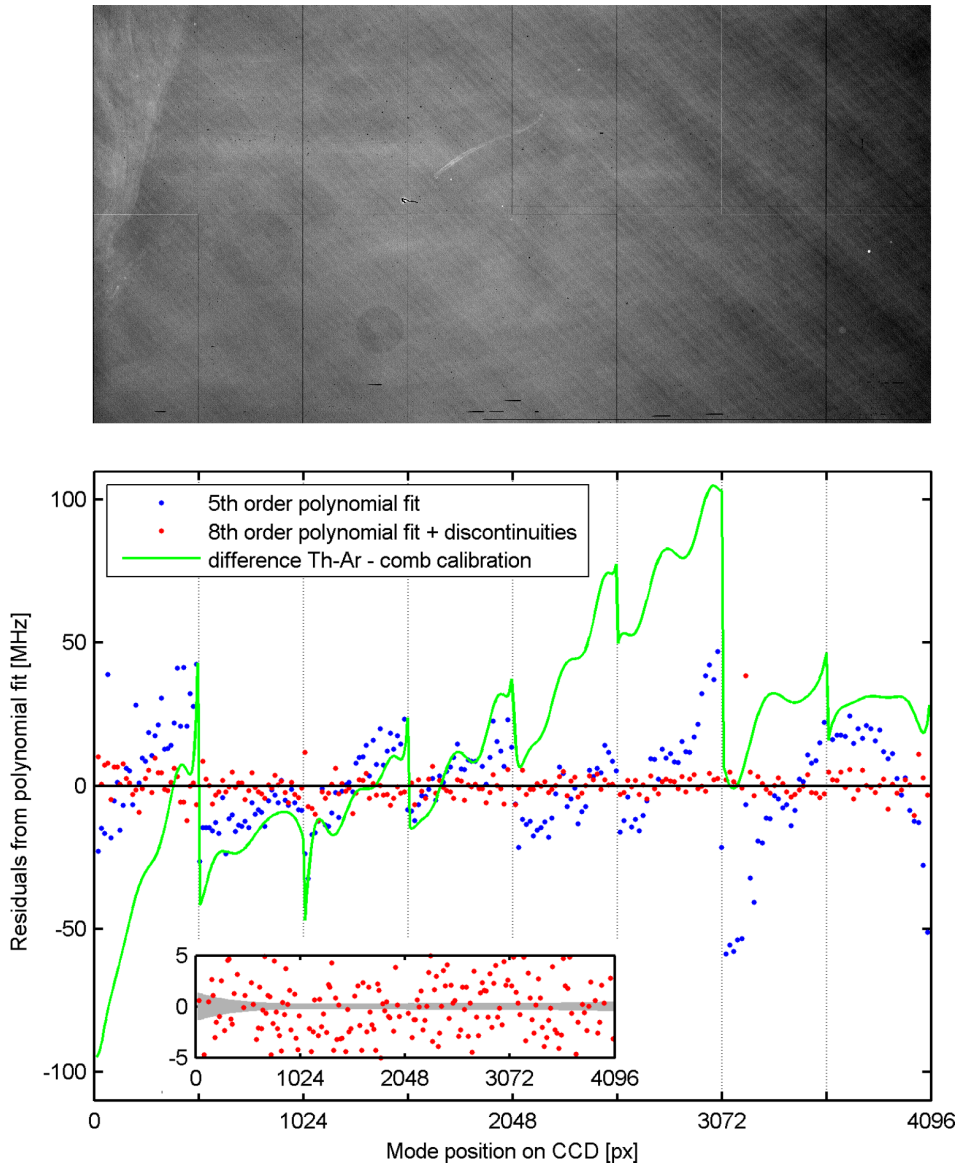
Figure 5.12*: Detector inhomogeneities unveiled by residuals of the calibration curve. Polynomials are fitted to the pixel versus frequency distribution of a fit dataset, containing every second available mode of the data, used in figure 5.11. Fit functions are a global fifth-order polynomial (blue) and eight piecewise eighth-order polynomials (red) that cover 512 pixels each (72 parameters). The residuals of the test dataset, containing the complementary modes of the complete dataset, are plotted. Variations in pixel size, shape, position etc. originating from the manufacturing process lead to the pattern with this period which can also be seen in a flat field exposure of the CCD, shown above. The inset demonstrates that even the piecewise polynomials are an insufficient model, as the scatter of the residuals is far above the photon noise limit (shaded area). The solid green line shows the difference between the usual Th-Ar calibration curve (global fourth-order polynomial) and the piecewise eighth-order comb calibration curve.*

of lines are available in every echelle order, each of them being photon noise limited in its uncertainty. A polynomial model that is not overfitted, however, still leads to residuals far above the photon noise as shown above. The reason is an unmodelled fine-structure of the calibration curve, which derives from pixel-to-pixel or even intra-pixel sensitivity variations. This fine-structure needs to be considered to correctly predict the position of a line that was not used for fitting.

5.6.3 Tuning the comb for improved absolute calibration

An alternative to a polynomial model is interpolating between the individual modes. In the dataset used for fitting, two lines are 15 to 22 pixels apart on the CCD (depending on their position on the CCD), so interpolating between them will not resolve the fine-structure of the calibration curve either. Consequently, the residuals scatter as much as when using the polynomial model (see figure 5.11). An interpolation with a cubic spline performs slightly better than a linear interpolation in this case.

Even with the maximum dense spacing of calibration lines, provided by the frequency comb, the absolute calibration still suffers from small-scale variations of the calibration curve. A big advantage of the frequency comb over traditional calibration methods is the possibility that the modes can be shifted intentionally and in a deterministic way. Changing the comb's offset frequency shifts all comb modes by the same amount (in frequency) while changing the repetition rate induces a shift proportional to the mode's frequency. Without some technical effort, the offset frequency cannot be shifted by more than one fundamental mode spacing since it is detected as a beat note of the comb at the fundamental repetition rate ($0 < f_0 < f_r$). Scanning the comb over several pixels is achieved easily by tuning the repetition rate, as the mode spacing is multiplied by the fundamental mode number. Since this is on the order of 10^6, a tiny variation of the repetition rate suffices to shift the optical frequencies by a large amount.

In a test series, the offset frequency is intentionally detuned in several steps and the line shift is measured with the spectrograph by employing the calibration curve derived in the previous section. For each detuning, a series of 10 acquisitions is recorded and the results are summarized in table 5.1. Shifts as low as 200 kHz that correspond to 10 cm/s can be traced, which is limited by photon noise.

Using these data, it is possible to take two datasets with different shifts of the offset frequency to create a combined dataset which is then interpolated. In this way, the distance between two neighboring lines that are used for interpolation is alternatingly large (~ 10 pixels) and very small ($0.001 - 0.01$ pixels). The remaining datasets are used as before to test the performance of the model. Depending on the choice of the two fit datasets, the lines in the test dataset are either contained in the large or the small interval between the interpolated lines. In the small interval, the interpolation corresponds well with the measured line positions, independent of the

Δf_0 [MHz]	measured shift [MHz]	σ [MHz]
-0.4	-0.48	0.24
-0.2	-0.33	0.32
0.4	0.22	0.29
2.0	2.09	0.39
4.0	4.19	0.17
8.0	7.93	0.21
16.0	16.08	0.26
120.0	119.97	0.22

Table 5.1*: Calibration tunability. The offset frequency f_0 of the comb can be varied and a constant shift of all lines will be measured. The measured shifts agree with the set values Δf_0 within the statistical uncertainty σ of a single acquisition, which itself is close to the photon noise of 0.22 MHz (11 cm/s), averaged over 10 exposures of 80 s each.*
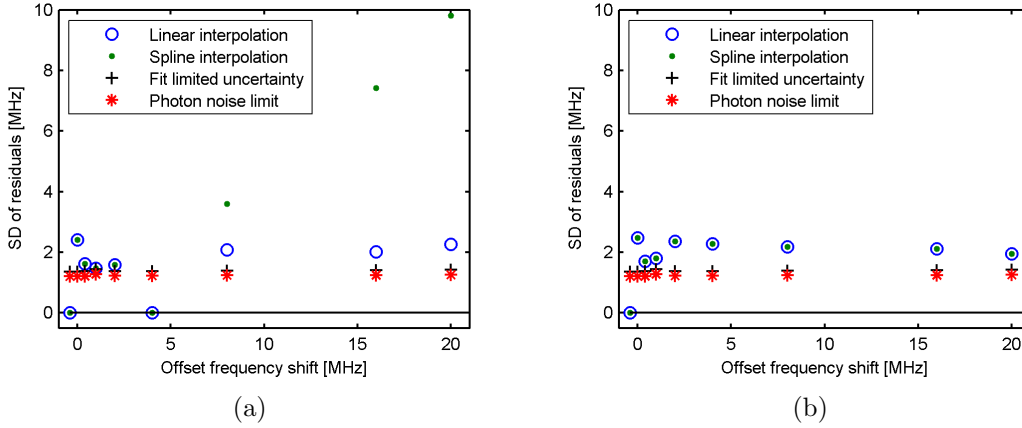

Figure 5.13*: Interpolated calibration curve derived from the datasets with shifted offset frequencies (section 5.5). Two datasets are combined and the measured pixel-to-frequency distribution is interpolated linearly or with a cubic spline. The residuals of these datasets are zero. The photon noise limit and the limit due to the uncertainty of the fitted line position are plotted for comparison. (a) A densely spaced fit dataset leads to deviations of the spline interpolation outside the smaller interval of 4 MHz. (b) For the smaller interval being as large as 120 MHz, the calibration accuracy is not independent of the choice of the interpolating function.*

interpolation method. Spline interpolations tend to overshoot, however, and thus predict lines in the large interval only poorly, while a linear interpolation still shows a good predictive efficiency (see figure 5.13).

Since each dataset consists of only 10 acquisitions with 361 modes, the photon noise limit of 1.3 MHz is higher than in the dataset of the previous section. The

standard deviation of the residuals, however, is much closer at the photon noise limit. By finely scanning the comb over the pixels, a very accurate calibration curve can thus be obtained. The maximum tolerable stepsize which is small enough to reliably track the fine-structure of the calibration curve must be determined in a further study with a larger range of frequency shifts. For shifts, larger than half the fundamental mode spacing of the oscillator, it is easier to tune the repetition rate, though. The only difference is that in this case every mode experiences a different shift, proportional to its frequency. The origin of the remaining difference between the model and the measured mode positions might be due to still unresolved intra-pixel sensitivity variations the and must be studied in more detail.

5.7   Impact of spectral broadening

After succeeding in matching the state-of-the art calibration of the spectrograph by using only one of its 72 echelle orders, a major effort was launched in 2009 to broaden the spectrum to cover more orders. Shortly before the 2010 campaign, a 100 nm-wide spectrum could be obtained by sending the light after the SHG stage into a highly nonlinear, microstructured fiber. When sending the light to the spectrograph, the first impression was very promising. In figure 5.3 the raw data from the two CCDs is depicted, showing a spectrum which covers more than 20 echelle orders. Since the mode spacing in this acquisition was too narrow, a similar spectrum with a mode spacing of 14 GHz was evaluated and the photon noise limit on a single acquisition is 4.5 cm/s. No spectral flattening was applied and so the wings of the spectrum were only weak. To improve the photon noise limit of this spectrum, it would have been possible to reduce the high intensity in the central part of the spectrum by an adaptive spectral filter and increase the overall flux by removing neutral density filters, which were inserted to prevent saturation of the detector. The minimum photon noise limit of this spectrum would then be 1.2 cm/s, assuming a S/N of 500 in every available line.

At second glance, however, analyzing the repeatability of a series of 48 acquisitions reveals dramatic systematic shifts on the detected line positions. The uncertainty of the drift on a single acquisition amounts to several m/s (see figure 5.14(a)). Individual lines apparently deviate from their theoretical frequency by up to 500 m/s (1 GHz) while the photon noise on a single line is only 1.0 m/s. Additionally, unidentified external parameters influence the position of the modes and can cause drifts up to 400 m/s, although the comb is phase-stabilized at all times. This effect can undoubtedly be attributed to the broadening process in the microstructured fiber. To prove this statement, the light is split up directly in front of the fiber and a part is coupled directly to the second channel of the spectrograph. No systematic deviation from the photon noise is observed in this case.

To exclude that interferences between the modes in the multimode fibers are
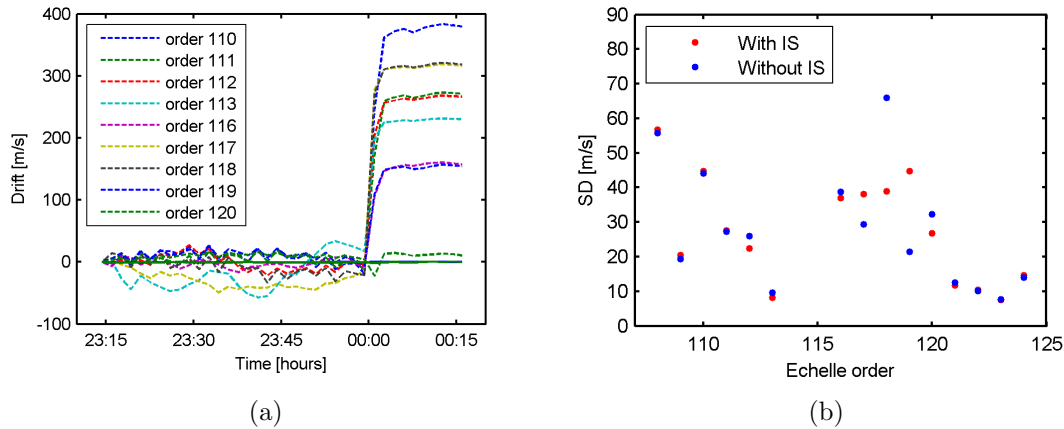
(a)   (b)

Figure 5.14: *(a) Calibration repeatability after broadening the comb in a microstructured fiber (dotted lines). Not only are large differences between acquisitions observable but also a sensitivity to unidentified external parameters. It might be that the coupling to the PCF was optimized after acquisition 28, leading to the subsequent step-like drift. For comparison, the drift of a part of the light that was not sent through the PCF is measured with the second channel (solid lines, showing order 113 and 116). (b) Invariance of the magnitude of line shifts when using an integrating sphere (IS) for coupling the light to the multimode fibers. The standard deviation (SD) of the line shifts of 9 acquisitions with a broadened spectrum with respect to a reference acquisition is plotted for every illuminated order. The photon noise limit in each order is below 50 cm/s. The differences in SD are probably caused by polarization effects (see figure 5.15).*

again a problem when using a PCF, a test series with an integrating sphere is performed. This ensures that a potential variation of the mode profile after the PCF will not affect the coupling to the multimode fiber as discussed in section 5.4. Part of the output of the PCF is coupled to channel B via the sphere while channel A is fed with the other part. Figure 5.14(b) shows that large drifts are still observed in both channels. Since the integrating sphere certainly improves the scrambling of the spatial modes before coupling to the multimode fiber, the line shifts must indeed have their origin in the PCF.

A strong dependence on the power coupled through the PCF and a correlation with the onset of spectral broadening is observed as well. When only low power levels are coupled to the fiber and no spectral broadening occurs, the line positions are stable and photon noise limited repeatability is obtained. With the onset of spectral broadening, the stability of the modes vanishes. This is another strong indication that the nonlinear processes in the fiber are the cause for the observed line shifts.

Provided that the shifts are generated in the PCF, the drift in channel A and B should be perfectly correlated for every individual line. Taking a closer look
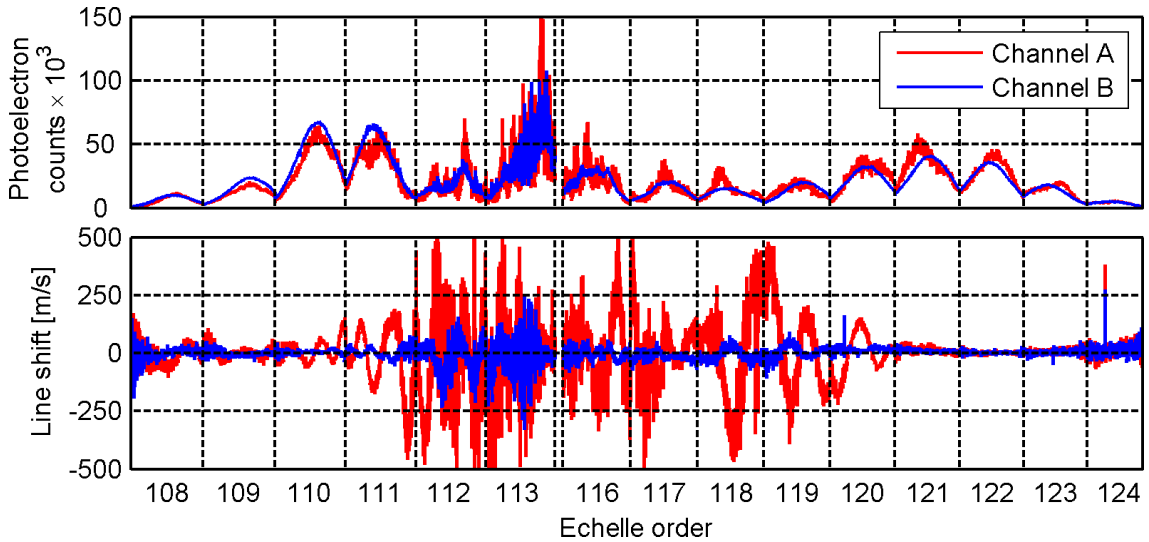
Figure 5.15*: Correlation of line shifts in channel A and B after spectral broadening. The difference of the line positions of a single acquisition with respect to a reference acquisition is plotted for all illuminated orders (lower panel). The light was split after the FPC with an uncoated wedge and the reflected light is thus partially polarized. An anti-correlation in line shift between both channels is evident. The maximum photoelectron count rate of every line is plotted for comparison (upper panel). The spectrum is in general smoother in channel B and no correlation between strong line shifts and especially high or low intensity can be concluded. Channel B is fed by an integrating sphere but probably the partial polarization of channel A is responsible for the larger shifts and structured spectrum (see text).*

at the data series with the integrating sphere, however, both correlation and anti-correlation can be observed (see figure 5.15). A plausible explanation for this discrepancy is a polarization dependency of the line shifts. After the PCF, the part which was not coupled to the integrating sphere was separated with an uncoated wedge. Depending on the incident angle, the wedge is thus partially polarizing. Assuming that the line shifts have a polarization dependency, the strongly polarized, reflected light thus shows larger shifts while in the transmitted light the contributions of both polarizations largely cancel each other. Nonlinear effects in the PCF — being the origin of the shifts — are sensitive to the polarization and, due to the complexity of the interactions in the fiber, can also explain why both correlated and anti-correlated line shifts are induced in both polarizations. Analyzing in detail, which parts of the spectrum acquire polarization-dependent line shifts, might be useful in the future to identify the exact mechanisms in the PCFs that are responsible for the shifts.

The analysis of all data, obtained in the 2010 calibration campaign, indicates that the nonlinear processes in the PCF affect the repeatability of the mode positions. As spectral broadening after the SHG stage was first observed shortly before the equipment needed to be shipped to Chile in February 2010, there was no opportunity
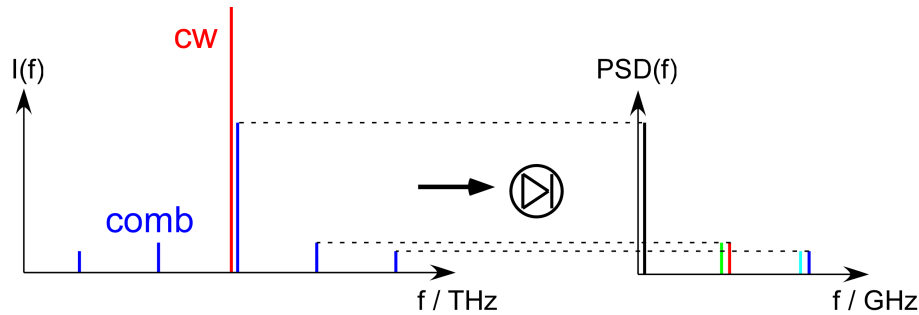
Figure 5.16: *Heterodyne measurement of the comb mode suppression after spectral broadening. A Nd:YAG cw laser is locked to the unbroadened comb 40 MHz below a transmitted mode (at 532.2 nm) and both the comb after the PCF and the cw laser are superimposed on a photodiode. The power in the RF modes then corresponds to the intensities of the comb modes.*

to study the fiber's effect on the filtered comb at that time. Only after returning to the laboratory at MPQ was a thorough investigation carried out which confirmed the origin of the poor repeatability.

5.7.1   Analysis of the excess calibration drifts

As described in section 3.8, a temporally varying, asymmetric reamplification of the suppressed modes in the PCF can be responsible for the observed drifts. To verify this hypothesis, a heterodyne measurement between the filtered and broadened comb and a stable cw laser was performed. The cw laser was a Diode laser, emitting a narrow line (~ 100 kHz FWHM) at around 1050 nm which was frequency doubled to 525 nm. It was locked to the comb at 20 MHz below a transmitted comb mode in the infrared, resulting in a 40 MHz separation after the SHG stage. The higher (lower) frequency, suppressed modes at 2 and 4 GHz were thus detected at 2.04 (1.96) GHz and 4.04 (3.96) GHz. Variations in the sensitivity of the photodiode between the corresponding higher and lower frequency modes could be neglected in this way. The measurement principle is depicted in figure 5.16.

After the SHG crystal, the suppression of the neighboring 2 and 4 GHz modes is 28 and 32 GHz, respectively. Any intensity variation of the beatnote is within the systematic uncertainty of the spectrum analyzer of ± 0.5 dB. By convolving the transmitted and suppressed modes with the PSF of HARPS (a Gaussian with a 5 GHz FWHM), the corresponding repeatability can be simulated. The variation is not larger than 20 cm/s, which corresponds to the instrument limit. Since the repeatability obtained with this light at HARPS is photon noise limited, no other result is expected. Figure 5.17 shows the suppression of the modes before and after the PCF for different power levels as well as the simulated calibration repeatability. With the onset of nonlinearities in the PCF (indicated by spectral broadening),
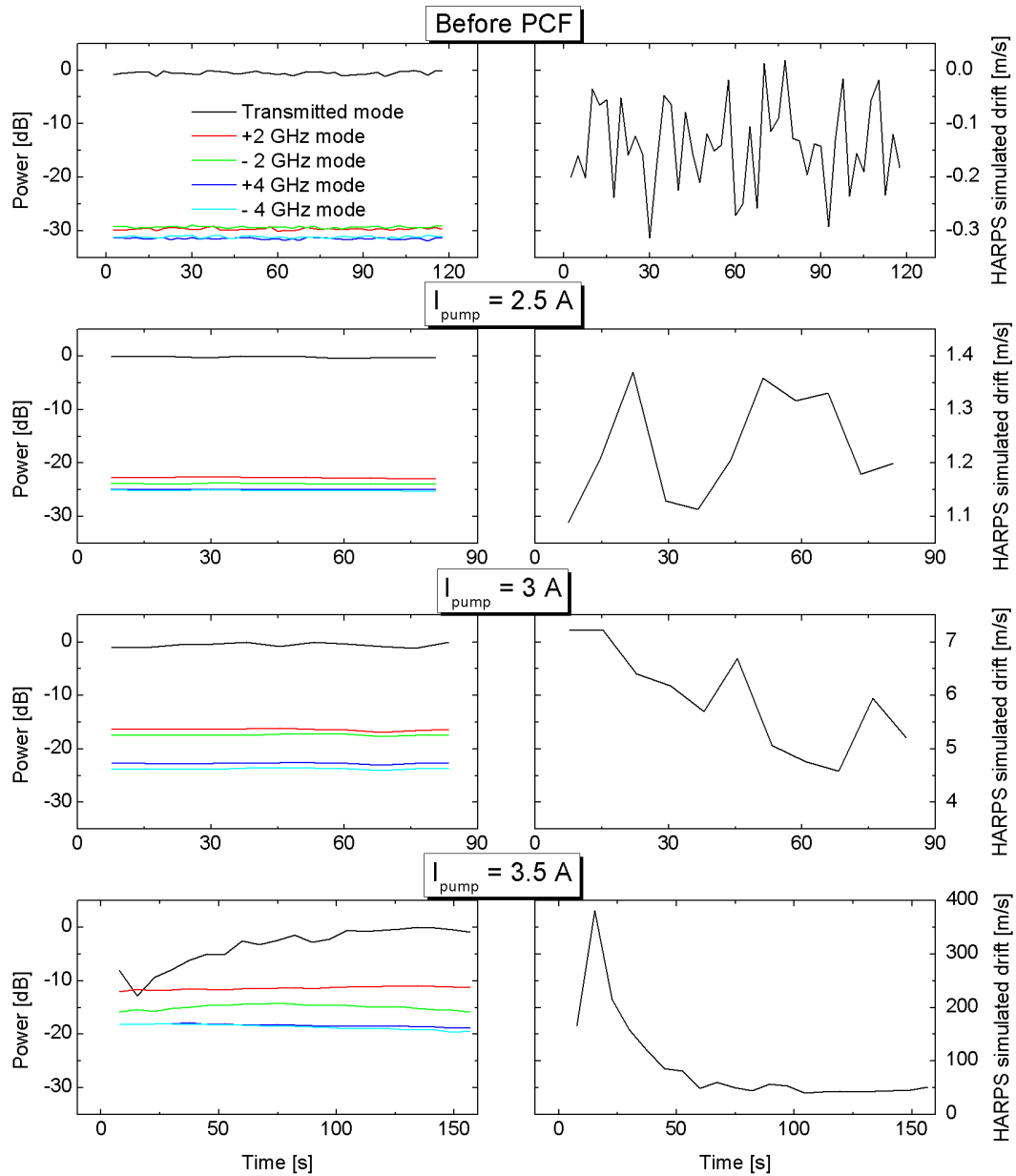
Figure 5.17: *Recovery of the suppressed modes in the PCF at different power levels (left column) and corresponding simulated calibration drift (right column). The power level of the RF beatnotes of a cw laser with the broadened comb was monitored over time. During a series nothing was changed or touched in the system and the pump power of the last amplifier is increased from one series to the next. For comparison, the beatnotes with the unbroadened comb before the PCF were also recorded. For every series, the drift of a calibration of HARPS with these five modes is simulated by convolving the modes with the PSF of HARPS, fitting one Gaussian to the resulting intensity distribution and plotting a time series of the line center. Note the different ordinate scale for the simulated drifts.*
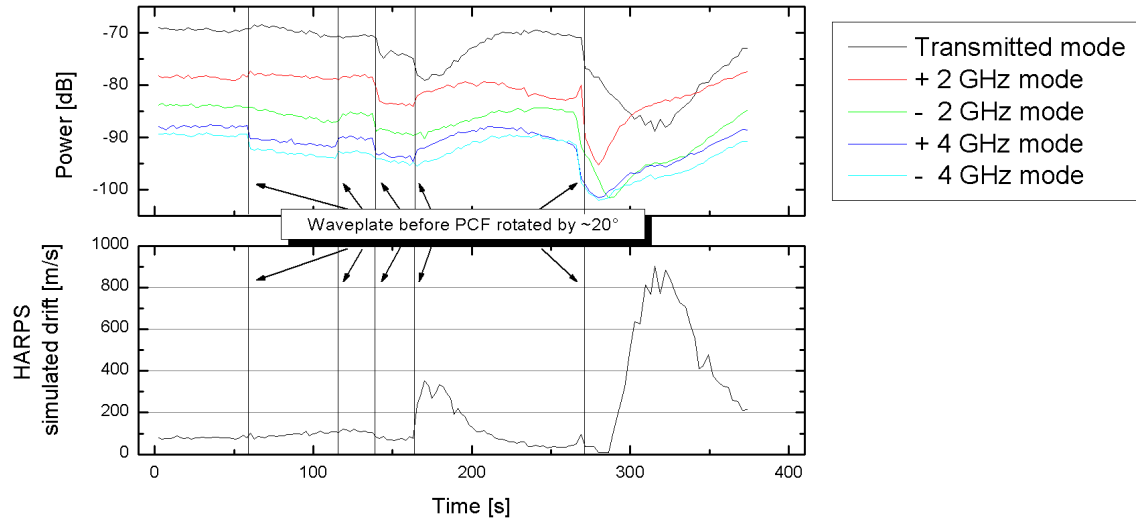
Figure 5.18: *Polarization dependence of the recovery of the suppressed modes. The same heterodyne measurement as above is performed with the last amplifier pumped at 4 A. At several times the half-wave plate in front of the PCF is rotated but nothing at the system is changed or touched in between. Note that the initial simulated shift is already $\approx 80\,m/s$ with respect to the case of symmetrically suppressed modes.*

the suppression of the intermediate modes decreases and an asymmetry between the higher and lower frequency modes arises. This first leads to a stable offset in the detected line position, which then becomes temporally instable with increasing power. At the highest pump powers, the suppressed modes can be reamplified to even exceed the transmitted mode's intensity. The simulated drift of the detected line position on HARPS corresponds very well with the actually measured data at HARPS, both in amplitude and timescale. A second analysis, shown in figure 5.18, demonstrates that the recovery of the suppressed modes is very sensitive to the input polarization as well.

Work is still ongoing to find a solution to this issue. Intensity variations of the light inside the PCF and an intensity-dependent phase can serve as an explanation for the temporal variation of the reamplification. The intensity variations themselves might be the result of amplitude noise. A possible solution could then be to implement a noise-eater to actively stabilize the intensity. Another reason might be a mechanical instability in the coupling to the PCF. Starting with a larger core of the PCF and drawing a stronger taper could provide a solution to relax the coupling sensitivity. The straight-forward solution, however, is to simply increase the suppression of the intermediate modes and thereby avoid the nonlinearities from the beginning. For example, no recovery of the suppressed modes at 250 MHz is observed, and their suppression is $\approx 15\,$dB better than the 2 GHz modes. Provided that the nonlinear reamplification is no resonant process (e.g. in contrast to forward Brillouin scattering), this is an indication that an increased suppression of the modes

indeed prevents their recovery. A third FPC with $m = 1$ is thus implemented in front of the high-power amplifier. Additionally, another intermediate amplifier is inserted between the second and third cavities.

Depending on the success of these measures and the related effort, the presented system, which includes a prevention of the reamplification of the intermediate modes, might or might not be the best way to achieve a comb calibration with a repeatability below 1 cm/s. Should the spectral broadening after filtering the comb to the final mode spacing prove to be too problematic, alternative approaches need to be investigated. It might be advantageous to first broaden the comb before filtering it with multiple FPCs for different spectral regions. Since it has already been proven that setting up a very robust lock of a cavity is feasible by use of an appropriate design, there is no counter-argument against employing even a larger number of FPCs .

Part of the results presented in this chapter have been published in Monthly Notices of the Royal Astronomical Society [45] and in the Proceedings of the SPIE Conference 2010 [46].

Chapter 6

Conclusion and outlook

With this work, a specifically designed frequency comb is shown to be a suitable calibration source for high precision spectrographs. Already in the first calibration tests at the VTT and HARPS, the performance of state-of-the-art calibration sources (especially Th-Ar spectral lamps) has been significantly exceeded both in repeatability and in absolute frequency accuracy. Although using only one and a half echelle order out of the total of 72 orders of HARPS, a photon noise limited repeatability of about 2 cm/s could be obtained when averaging over several acquisitions. This is one order of magnitude better than the repeatability that can be obtained with Th-Ar lamps. The result demonstrates that the simultaneous calibration scheme reliably tracks instrumental drifts on the cm/s-level which is very important for future astronomical observations.

The maximally high density of the comb's calibration lines allowed for the first time to detect pixel-to-pixel variations in the calibration curve. A 512 pixel pattern is observed that derives from the CCD being a mosaic of sixteen subarrays of 512×1024 pixels. Including the variations in size and sensitivity at the borders of the subarrays in the calibration curve resulted in an absolute calibration uncertainty of 2.4 m/s which is also one order of magnitude better than previously obtainable with Th-Ar calibrations. First tests have been performed, in which the comb was tuned to resolve even the intra-pixel structure of the calibration curve. The absolute calibration of the CCD could be further improved with this technique and is only a factor of two above the photon noise limit.

Unfortunately, in the 2010 calibration campaign the attempt failed to achieve an even higher repeatability by employing a spectrally broadened comb that covered more than 100 nm. When broadening the comb in a highly nonlinear fiber after the mode spacing had been increased with Fabry-Pérot cavities, the suppressed modes were reamplified. This effect degraded the calibration performance since the initially suppressed modes cannot be resolved with the spectrograph and vary in intensity over time. This effect however, is not of fundamental nature but can probably be reduced below detectability. Preliminary results with a third FPC in the setup

indicate that an increased suppression of the intermediate modes indeed prevents their reamplification. If this proves to be true, there should be no further obstacle to obtain a repeatability of the calibration on the sub-cm/s level.

Impact on the astrophysics community   Over the past few years the interest in frequency combs for applications in astronomy has grown steadily. Two competing groups have started developing "astrocombs" on their own [178, 155], and several astrophysics institutes have shown their interest in this new technique. A cooperation with the Kiepenheuer Institute for Solar Physics has been started to permanently install a frequency comb at the VTT spectrograph — the same spectrograph where the first proof-of-principle test was carried out (see chapter 4). The absolute frequency calibration to measure the direction of the particle flow in the solar photosphere is of particular interest to this project. Furthermore, a cooperation with the observatory of the Ludwig-Maximilians-University in Munich has been initiated to install a frequency comb at the FOCES spectrograph, which will be set up at the Wendelstein observatory in the Bavarian Alps.

In this work, the focus has been on developing a frequency comb for calibrating spectrographs with the highest possible sensitivity to redshift variations. As discussed in section 2.3, these spectrographs are built for the visible wavelength range, and the comb has been designed accordingly. Observations in different spectral regions, however, might benefit from an improved calibration as well. Especially in the near-to-mid-infrared range the best repeatability achieved so far is above the m/s-level and partially limited by the calibration source [176]. Although our first tests have been performed in this wavelength range, we have since changed our focus to the visible range. Our colleagues at NIST, however, have recently demonstrated a comb system, based on an Er-fiber laser that is very similar to ours but includes spectral broadening [177].

Future developments   It was mentioned in chapter 3 that the strong spectral modulations after the PCF need to be smoothened in order to have an optimum S/N for every line on the detector. This can done with an adaptive spectral filter, e.g. by employing a spatial light modulator (SLM) as depicted in figure 6.1. A SLM (Jenoptik SLM-S640) was purchased before the 2010 calibration campaign, and precursor tests have been performed successfully. Since the problems with the repeatability of the broadened spectrum could not be overcome during the campaign, the SLM has not been not put to use since. The resolution of the filter is given by the number of pixels (640) and the spectral bandwidth ($380 - 680\,\mathrm{nm}$ for HARPS). At a mode spacing of $18\,\mathrm{GHz}$, $\sim 20,000$ modes are contained in this bandwidth. One pixel is thus covered by approximately 30 modes. Consequently, mode-to-mode intensity variations cannot be compensated with this approach and must either be tolerated or leveled out with another technique (e.g. using a VIPA [173]). Small-scale modulations, however, have only been observed at the seed wavelength range
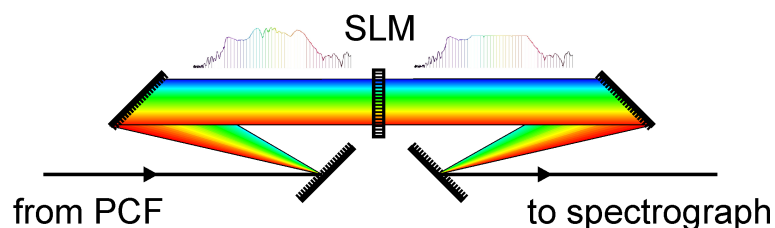
Figure 6.1: *Schematics of an adaptive spectral filter, consisting of a spatial light modulator (SLM).*

after broadening (see figure 5.15). If these modulations appear exclusively in this range, then only one or two orders would be affected (or none if directly broadening from the fundamental spectrum). This minor side effect could simply be tolerated.

Shortly after this project was initiated, a new type of frequency comb generator was developed: a micro-cavity with an ultra-high optical quality factor [102]. When such toroidal resonators are pumped with a sufficiently-powerful cw laser, cascaded side bands are produced that are phase-coherent to each other, since they are generated via non-degenerate four-wave mixing. The mode spacing of these combs is determined by the cavity's FSR, given by the diameter of the toroids. Typical sizes on the sub-$100\,\mu$m scale lead to spacings from several hundred GHz to THz, but larger toroids can already be manufactured with a minimum mode spacing of $80\,$GHz. Currently, resonators from different materials (e.g. CaF_2, MgF_2) are being investigated to enable the generation of frequency combs in the visible and near-to-mid-infrared spectrum. These toroids or similar micro-cavities have the potential of being simple, reliable and cost-effective comb generators. At present, however, some development is still necessary for them to meet the requirements for a calibrator of astronomical spectrographs.

A glimpse into the far future suggests the prospect of heterodyne spectroscopy of starlight with a frequency comb. With the help of adaptive optics, a significant amount of light could be coupled into single-mode fiber. In principle, spectrographs would no longer be necessary for the heterodyne detection scheme. To resolve the ambiguity of the mode spacing, however, a spectral filter with a resolution corresponding to the bandwidth of the photodetector would be beneficial. The requirements for the monochromator would be much more relaxed, however, since no position stability on the detector pixels would be needed. Unfortunately, adaptive optics is at present only available in the infrared regime, but there are efforts to enable this technique also in the visible range [175]. Alternatively, a space telescope could be employed with a frequency comb attached to it.

In summary, with the calibration of astronomical spectrographs, an exiting new field has been established that builds on the invention of frequency combs. The first results described in this work prove the enormous potential of this symbiosis between astronomy and quantum optics. Soon, the first calibration lamps will be replaced

by combs and in the near future, observations with unprecedented sensitivity to redshift variations might then answer some of the fundamental questions about our universe as well as our galactic neighborhood.

Appendix A

Fabry-Pérot cavities and dispersion

A.1 Cavity mirror dispersion

According to the manufacturer, the mirrors used for the FPCs in this work have a dispersion curve as shown in figure A.1.
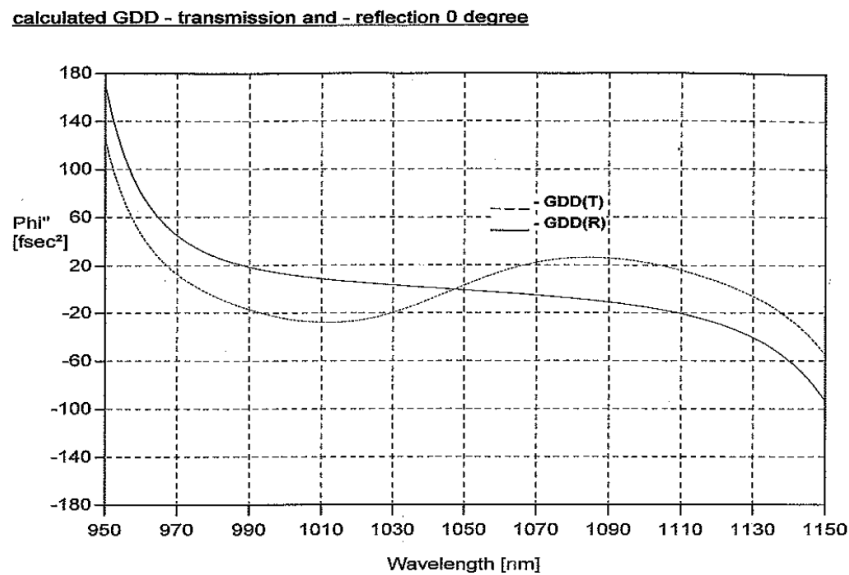

Figure A.1: *GDD curve of the mirrors used in this work. The GDD was calculated by the manufacturer (Layertec GmbH) based on a fit to the measured transmission curve of the mirrors.*

The maximum bandwidth that the Yb-fiber oscillator can deliver, ranges from 1000 to 1100 nm. In this range, the group delay dispersion of the mirror can be

linearly approximated as

$$\frac{\mathrm{d}^2\phi}{\mathrm{d}f^2} \approx \frac{20\,\mathrm{fs}^2}{15\,\mathrm{THz}}\,(f - f_0), \tag{A.1}$$

with $f_0 \approx 285\,\mathrm{THz}$ (1052 nm) being the reference frequency at which the FPC is locked with the cw-laser. Integrating this equation and assigning a zero linear and constant phase to f_0 yields

$$\phi \approx \frac{20\,\mathrm{fs}^2}{15\,\mathrm{THz}}\left(\frac{1}{6}f^3 - \frac{f_0}{2}f^2 + \frac{f_0^2}{2}f - \frac{f_0^3}{6}\right). \tag{A.2}$$

At 1000 nm and 1100 nm the additional phase relative to the reference frequency amounts to $2.2 \times 10^{-4}\,\mathrm{rad}$ and $1.6 \times 10^{-4}\,\mathrm{rad}$ respectively.

A.2   Dispersion of the intracavity medium

If the dispersion of the mirrors is not limiting the transmitted bandwidth of the cavity, the dominating effect is the dispersion of the medium inside the resonator, typically air. Neglecting the Guoy-phase, the round-trip phase δ of the cavity is according to equation (3.7) given by

$$\delta = 4\pi f \frac{n(f)L}{c} \tag{A.3}$$

$$= 4\pi(f_c + \Delta f)\frac{n(f)L}{c}. \tag{A.4}$$

The cavity is locked to the frequency comb at the frequency f_c. At this frequency, δ is an exact multiple of 2π since the transmission peak is stabilized on that mode. For any other comb mode, separated from f_c by Δf, the round-trip phase is thus given by

$$\delta = 4\pi\Delta f \frac{n_c + \Delta n L}{c}, \tag{A.5}$$

with $\Delta n = n(f) - n_c$ and $n_c = n(f_c)$. For a dispersion-free cavity with $\Delta n = 0$, cavity length and center frequency are tuned such, that all comb modes are transmitted and hence

$$\delta = 4\pi\Delta f \frac{\Delta n L}{c} \tag{A.6}$$

$$= 2\pi \frac{c\,\Delta\lambda}{\lambda_c^2}\frac{\Delta n}{n\,m\,f_r}, \tag{A.7}$$

with $\Delta f = c\,\Delta\lambda/\lambda_c^2$ and $L = c/(2\,n\,m\,f_r)$. λ_c is the central wavelength, m the filter ratio of the FPC and f_r the comb's fundamental repetition rate.

According to equation (3.9) the phase shift at which the transmission drops by 50 % requires

$$\frac{1}{1 + F \sin^2(\delta/2)} \geq \frac{1}{2} \tag{A.8}$$

and thus

$$\sin(\delta/2) \leq \frac{1}{\sqrt{F}}. \tag{A.9}$$

Assuming that $\delta \ll 1$ and inserting equation (A.7) gives

$$2\pi \frac{c\,\Delta\lambda}{\lambda_c^2} \frac{\Delta n}{n\,m\,f_r} \leq \frac{1}{\sqrt{F}} \tag{A.10}$$

and

$$\Delta\lambda \leq \frac{\lambda_c^2\,m\,f_r}{\pi\,c\sqrt{F}} \frac{n}{\Delta n}. \tag{A.11}$$

In the wavelength range under consideration it is justified to assume $n \propto \lambda$. Since the calculation above determines only half of the usable wavelength range (to one side of the center wavelength), the corresponding index variation is only half of the true value as well. The total wavelength range in which the transmission is above 50 % is thus given by

$$\Delta\lambda \leq \frac{4}{\pi} \frac{\lambda^2 m f_r}{c\sqrt{F}} \frac{n}{\Delta n}. \tag{A.12}$$

Appendix B

GVD compensating pulse compressors

B.1 Grating compressor

A pair of two gratings can be arranged in such a manner that a transversing pulse experiences a negative chirp, i.e. the grating pair has an anomalous GDD. This was first described by Treacy in 1969 [127] and the principle is described in many textbooks (e.g. [118, 119]). It is presented here to motivate the combined grating/prism compressor.

Each frequency component ω has a different path length $l(\omega)$ when traveling through the compressor due to the angular dispersion of the gratings. For first order diffraction, the grating law relates the diffraction angle θ_o to the angle of incidence θ_i via

$$\sin \theta_o = \frac{2\pi c}{g\omega} - \sin \theta_i, \tag{B.1}$$

with g being the groove density of the grating. Looking at the optical path, depicted
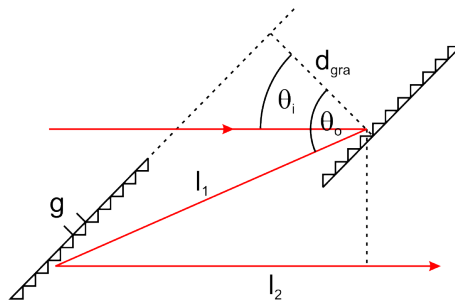

Figure B.1: *Sketch of a grating pair compressor with notations.*

in Figure B.1, the path length can be expressed as

$$l(\omega) = l_1 + l_2 = d_{gra} \frac{1 + \cos(\theta_0 - \theta_i)}{\cos \theta_o}. \tag{B.2}$$

For two wavelengths, hitting an adjacent groove, an additional phase of 2π must be considered, which leads to the result that the optical path length of each frequency component is related to the phase delay τ_p by [127]

$$l(\omega) = c \frac{\mathrm{d}\phi}{\mathrm{d}\omega} = c\tau_p. \tag{B.3}$$

The GDD is then calculated as the second derivative of the phase at the central frequency ω_c

$$\left(\frac{\mathrm{d}^2\phi}{\mathrm{d}\omega^2} \right)_{\omega_c} = -\frac{4\pi^2 d_{gra} c}{\omega_c^3 g^2 \cos^3 \theta_{oc}} \tag{B.4}$$

and the TOD is given by

$$\left(\frac{\mathrm{d}^3\phi}{\mathrm{d}\omega^3} \right)_{\omega_c} = -\frac{3}{\omega_c} \left[1 + \frac{2\pi c}{\omega_c d_{gra}} \frac{\sin \theta_{oc}}{\cos^2 \theta_{oc}} \right] \left(\frac{\mathrm{d}^2\phi}{\mathrm{d}\omega^2} \right)_{\omega_c}, \tag{B.5}$$

with θ_{oc} being the angle of diffraction of ω_c.

It can be seen directly from equations (B.4) and (B.5) that a grating compressor has always negative GDD and positive TOD. To recombine the spatially dispersed spectrum, typically a mirror or retro-reflector is put after the grating pair. In this double-pass configuration, the compressor has twice the GDD and TOD.

B.2 Hybrid grating/prism compressor

While a grating compressor can compensate the positive second order chirp, accumulated in a fiber, unfortunately the TOD of the compressor has the same sign as fibers. After propagating through a long fiber section, the pulse cannot be recompressed to its bandwidth limit with a simple grating pair but the third order chirp adds up. Inserting a prism pair between the two gratings has been shown to modify the dispersion, such that the TOD can change its sign and become negative [129].

A ray-tracing program has been developed during this work to simulate the dispersion of the hybrid compressor. For each frequency component, the beam is characterized by its origin and a propagation angle (in the plane of propagation). The surfaces of the components are defined in the same way. At the surfaces of the grating and the prisms, the propagation angle is recalculated according to the grating law (equation (B.1)) or Snell's law ($n_1 \sin \theta_1 = n_2 \sin \theta_2$), respectively. The crossing of the beam with the next surface is computed by solving the two linear equations.
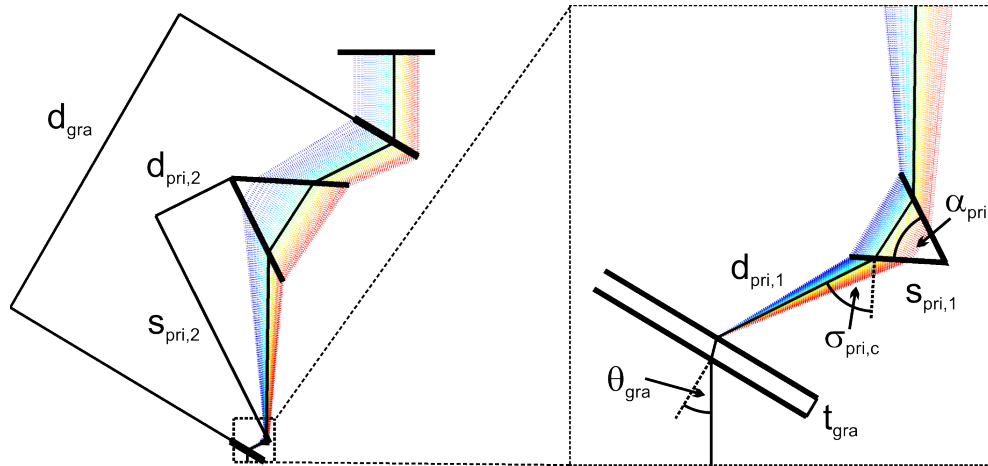
Figure B.2*: Sketch of the hybrid grating/prism compressor with notations. The distances and angles correspond to the values, given in table B.1. The color-coded spectrum ranges from 980 to 1120 nm with the short wavelength egde colored in blue.*

Central wavelength of the spectrum	λ_c	1050 nm
Groove density of the grating	g	1000 lines/mm
Incidence angle on the grating	θ_{gra}	31 °
Apex angle of the prisms	α_{pri}	60 °
Incidence angle on the prisms	$\sigma_{pri,c}$	60 °
Distance between grating and 1st prism at λ_c	$d_{pri,1}$	5 mm
Insertion of the 1st prism at λ_c	$s_{pri,1}$	2 mm
Parallel distance between the prisms	$d_{pri,2}$	25 mm
Insertion of the 2nd prism (from apex to apex)	$s_{pri,2}$	75 mm
Distance between the gratings	d_{gra}	100 mm
Thickness of the gratings	t_{gra}	600 μm

Table B.1*: Exemplary settings of the hybrid grating/prism compressor.*

In this way, the optical path length for each frequency component is calculated. The phase shift at the grooves of the grating must be considered just as for the simple grating pair. The calculation does not differ from the case without a prism pair, if the inner surfaces of the two prisms are parallel, as the input and output beam are parallel in this case too. Consequently, the optical path length corresponds again to the phase delay, $l(\omega) = c\tau_p$, and the GDD and TOD can be derived by numerically computing the first and second derivative of l/c with respect to ω.

In figure B.2, a sketch of the hybrid grating/prism compressor is depicted with its defining lengths and angles. Transmission gratings are assumed instead of reflection
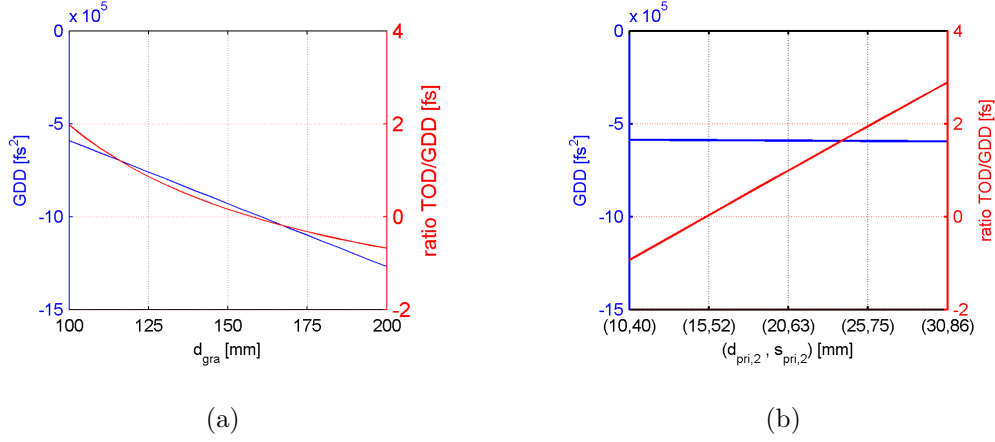
(a)

(b)

Figure B.3: *GDD and TOD in dependence on the hybrid compressor geometry. (a) The distance d_{gra} between the gratings is varied with the remaining parameters as given in table B.1. Both, GDD and TOD, are affected. (b) The position of the second prism $(d_{pri,2}, s_{pri,2})$ is varied. In this way, the TOD/GDD-ratio can be set nearly independently of the GDD.*

gratings because of their superior efficiency and the compressor is set up in double-pass configuration. With the values, given as an example in table B.1, the GDD of the compressor amounts to -590,000 fs^2, the TOD to -1,164,000 fs^3 and their ratio to +1.97 fs. In this configuration, the hybrid grating/prism compressor can indeed compensate both the GDD and TOD of the fiber.

Varying the geometry of the compressor enables tuning its dispersion (see figure B.3). While the distance between the two gratings affects both GDD and TOD, the position of the second prism only affects the TOD. Exploiting this behavior, a simple recipe can be deduced to align the compressor. After ensuring that the gratings and the prisms are parallel to each other, first the desired GDD is set by tuning the grating distance. The position of the second prism is then tuned to compensate the TOD.

Bibliography

[1] "Wstrzymał Słonce, ruszył Ziemię", famous polish saying in reference to Copernicus.

[2] E. Hubble, "A relation between distance and radial velocity among extra galactic nebulae", *Proceedings of the National Academy of Science* **15**, 169, (1929).

[3] A. Einstein, "Kosmologische Betrachtungen zur allgemeinen Relativitätstheorie", *Sitzungsberichte der Königlich Preußischen Akademie der Wissenschaften (Berlin)* 142, (1917).

[4] A. G. Riess *et al.*, "Observational Evidence from Supernovae for an Accelerating Universe and a Cosmological Constant", *Astronomical Journal* **116**, 1009 (1998).

[5] S. Perlmutter *et al.*, "Measurements of Ω and Λ from 42 High-Redshift Supernovae", *Astrophysical Journal* **517**, 565 (1999).

[6] D. N. Spergel *et al.*, "First-Year Wilkinson Microwave Anisotropy Probe (WMAP) Observations: Determination of Cosmological Parameters", *Astrophysical Journal Supplement Series* **148**, 175 (2003).

[7] J. A. Peacock *et al.*, "A measurement of the cosmological mass density from clustering in the 2dF Galaxy Redshift Survey", *Nature* **410**, 169 (2001).

[8] A. Sandage, "The Change of Redshift and Apparent Luminosity of Galaxies due to the Deceleration of Selected Expanding Universes.", *Astrophysical Journal* **136**, 319 (1962).

[9] According to the "Position statement on the definition of a 'Planet' " of the Working Group on Extrasolar Planets of the International Astronomical Union (IAU).

[10] A. Wolszczan and D. A. Frail, "A planetary system around the millisecond pulsar PSR1257 + 12", *Nature* **355**, 145 (1992).

[11] M. Mayor and D. Queloz, "A Jupiter-mass companion to a solar-type star", *Nature* **378**, 355 (1995).

[12] M. A. C. Perryman, "Extra-solar planets", *Reports on Progress in Physics* **63**, 1209 (2000).

[13] G. Chauvin *et al.*, "A giant planet candidate near a young brown dwarf", *Astronomy and Astrophysics* **425**, L29 (2004).

[14] S. Udry and M. Mayor, "Exoplanets: The Golden Age of Radial Velocities", *Extreme Solar Systems* in *Astronomical Society of the Pacific Conference Series* **398**, 13 (2008).

[15] F. Bouchy *et al.*, "The HARPS search for southern extra-solar planets: XVII. Super-Earth and Neptune-mass planets in multiple planet systems HD47 186 and HD181 433", *Astronomy and Astrophysics* **496**, 527 (2009).

[16] C. Lovis, and F. Pepe, "A new list of thorium and argon spectral lines in the visible", *Astrononmy and Astrophysics* **468,** 1115 (2007).

[17] J. J. Lissauer, "How common are habitable planets?", *Nature* **402**, C11 (1999).

[18] G. Rousset *et al.*, "First diffraction-limited astronomical images with adaptive optics", *Astronomy and Astrophysics* **230**, 2 (1990).

[19] C. A. Primmerman *et al.*, "Compensation of atmospheric optical distortion using a synthetic beacon", *Nature* **353**, 141 (1991).

[20] L. Pasquini, *et al.* "CODEX: measuring the expansion of the Universe (and beyond)", *The Messenger* **122**, 10 (2005).

[21] M. T. Murphy, *et al.*, "High-precision wavelength calibration of astronomical spectrographs with laser frequency combs", *Monthly Notices of the Royal Astronomical Society* **380,** 839 (2007).

[22] J. N. Eckstein, A. I. Ferguson, and T. W. Hänsch, "High-Resolution Two-Photon Spectroscopy with Picosecond Light Pulses", *Physical Review Letters* **40**, 847 (1978).

[23] D. E. Spence, P. N. Kean, and W. Sibbett, "60-fs Pulse Generation from a Self-Mode-Locked Ti-Sapphire Laser", *Optics Letters* **16**, 42 (1991).

[24] J. K. Ranka, R. S. Windeler, and A. J. Stentz, "Visible continuum generation in airsilica microstructure optical fibers with anomalous dispersion at 800 nm", *Optics Letters* **25**, 25 (2000).

[25] J. L. Hall and T. W. Hänsch, "History of optical comb development" in Femtosecond Optical Frequency Comb: Principle, Operation, and Applications, J. Ye, S. T. Cundiff (ed.), Springer (2004)

[26] S. A. Diddams *et al.*, "Direct Link between Microwave and Optical Frequencies with a 300 THz Femtosecond Laser Comb", *Physical Review Letters* **84**, 5102 (2000).

[27] R. Holzwarth *et al.*, "Optical Frequency Synthesizer for Precision Spectroscopy", *Physical Review Letters* **85**, 2264, (2000).

[28] M. Niering *et al.*, "Measurement of the Hydrogen 1S-2S Transition Frequency by Phase Coherent Comparison with a Microwave Cesium Fountain Clock", *Physical Review Letters* **84**, 5496 (2000).

[29] J. Stenger *et al.*, "Absolute frequency measurement of the 435.5-nm ^{171}Yb$^+$-clock transition with a Kerr-lens mode-locked femtosecond laser", *Optics Letters* **26**, 1589 (2001).

[30] Th. Udem *et al.*, "Absolute Frequency Measurements of the Hg$^+$ and Ca Optical Clock Transitions with a Femtosecond Laser", *Physical Review Letters* **86**, 4996, (2001).

[31] J. Stenger *et al.*, "Phase-coherent frequency measurement of the Ca intercombination line at 657 nm with a Kerr-lens mode-locked femtosecond laser", *Physical Review A* **63**, 021802 (2001).

[32] S. A. Diddams *et al.*, "An Optical Clock Based on a Single Trapped 199Hg+ Ion", *Science* **293**, 825 (2001).

[33] J. Ye, L. Ma, and J. Hall "Molecular Iodine Clock", *Physical Review Letters* **87**, 270801 (2001).

[34] A. Baltuška *et al.*, "Attosecond control of electronic processes by intense light fields", *Nature* **421**, 611 (2003).

[35] A. Bartels *et al.*, "Femtosecond-laser-based synthesis of ultrastable microwave signals from optical frequency references", *Optics Letters* **30**, 667 (2005).

[36] J. Ye, "Absolute measurement of a long, arbitrary distance to less than an optical fringe", *Optics Letters* **29**, 10, 1153 (2004).

[37] C. Gohle *et al.*, "A frequency comb in the extreme ultraviolet", *Nature* **436**, 234 (2005).

[38] C. Daussy *et al.*, "Long-Distance Frequency Dissemination with a Resolution of 10^{-17}", *Physical Review Letters* **94**, 203904 (2005).

[39] J. Kim, *et al.*, "Long-term femtosecond timing link stabilization using a single-crystal balanced cross correlator", *Optics Letters* **32**, 1044 (2007).

[40] A. Bartels *et al.*, "Ultrafast time-domain spectroscopy based on high-speed asynchronous optical sampling", *Review of Scientific Instrumentation* **78**, 035107 (2007).

[41] M. C. Stowe *et al.*, "Direct frequency comb spectroscopy", *Advances in Atomic, Molecular, and Optical Physics* **55**, 1 (2008).

[42] B. Bernhardt *et al.*, "Cavity-enhanced dual-comb spectroscopy", *Nature Photonics* **4**, 55 (2010).

[43] D. Höfling, diploma thesis (2008).

[44] T. Steinmetz, *et al.* "Laser Frequency Combs for Astronomical Observations" *Science* **321,** 1335 (2008).

[45] T. Wilken *et al.*, "High-precision calibration of spectrographs", *Monthly Notices of the Royal Astronomical Society* **405**, L16 (2010).

[46] T. Wilken *et al.*, "High-precision calibration of spectrographs using laser frequency combs", in *Proceedings of the SPIE conference* , **7735**, 77350T (2010)

[47] P. Vilar-Welter, diploma thesis (2009).

[48] S. Herr, diploma thesis (2010).

[49] B. N. Taylor and C. E. Kuyatt, "Guidelines for Evaluating and Expressing the Uncertainty of NIST Measurement Results", *NIST Technical Note* 1297 (1994)

[50] H. Fritzsch, "The fundamental constants in physics and their time dependence", *Progress in Particle and Nuclear Physics* **61**, 329 (2008).

[51] E. Witten, "Some properties of 0(32) superstrings", *Physics Letters B* **149**, 351 (1984).

[52] T. R. Taylor and G. Veneziano, "Dilaton couplings at large distances", *Physics Letters B* **213**, 450 (1988).

[53] P. A. M. Dirac, "The cosmological constants", *Nature* **139**, 323 (1937).

[54] T. Damour and J. H. Taylor, "On the orbital period change of the binary pulsar PSR 1913 + 16", *Astrophysical Journal* **366**, 501 (1991).

[55] M. P. Savedoff, "Physical Constants in Extra-Galactic Nebulae", *Nature* **178**, 689 (1956).

[56] R. Minkowski and O. C. Wilson, "Proportionality of Nebular Red Shifts to Wave Length", *Astrophysical Journal* **123**, 373 (1956).

[57] J. K. Webb, *et al.*, "Search for Time Variation of the Fine Structure Constant", *Physical Review Letters* **82**, 884 (1999).

[58] S. Bize, *et al.*, "Testing the Stability of Fundamental Constants with the ^{199}Hg$^+$ Single-Ion Optical Clock", *Physical Review Letters* **90**, 150802 (2003).

[59] E.Peik, *et al.*, "Limit on the Present Temporal Variation of the Fine Structure Constant", *Physical Review Letters* **93**, 170801 (2004).

[60] M. Fischer, *et al.*, "New Limits on the Drift of Fundamental Constants from Laboratory Measurements", *Physical Review Letters* **92**, 230802 (2004).

[61] T. Rosenband, *et al.*, "Frequency Ratio of Al$^+$ and Hg$^+$ Single-Ion Optical Clocks; Metrology at the 17th Decimal Place", *Science* **319**, 1808 (2008).

[62] Y. Fujii, "A possible new interpretation of the results of $\Delta\alpha/\alpha$ from QSO absorption lines", *Physics Letters B* **616**, 141 (2005).

[63] N. Kanekar, "Do the fundamental constants change with time?", *Modern Physics Letters* **23**, 2711 (2008).

[64] J.-P. Uzan, "The fundamental constants and their variation: observational and theoretical status", *Review of Modern Physics* **75**, 403 (2003).

[65] J. N. Bahcall, C. L. Steinhardt and D. Schlegel, "Does the Fine-Structure Constant Vary with Cosmological Epoch?", *Astrophysical Journal* **600**, 520 (2004).

[66] V. Batteiger, *et al.*, "Precision spectroscopy of the 3s-3p fine-structure doublet in Mg$^+$", *Physical Review A* **80**, 022503 (2009).

[67] A. V. Ivanchik *et al.*, "The fine-structure constant: a new observational limit on its cosmological variation and some theoretical consequences" *Astronomy and Astrophysics* **343**, 439 (1999).

[68] V. A. Dzuba *et al.*, "Space-Time Variation of Physical Constants and Relativistic Corrections in Atoms", *Physical Review Letters* **82**, 888 (1999).

[69] G. Lo Curto, private communication.

[70] H. Chand, *et al.*, "Probing the cosmological variation of the fine-structure constant: Results based on VLT-UVES sample", *Astronomy and Astrophysics* **417**, 853 (2004).

[71] M. T. Murphy, J. K. Webb and V. V. Flambaum, "Revision of VLT/UVES constraints on a varying fine-structure constant", *Monthly Notices of the Astronomical Society* **384**, 1053 (2008).

[72] P. Molaro, *et al.*, "Bounds on the fine structure constant variability from FeII absorption lines in QSO spectra", *European Physical Journal – Special Topics* **163**, 173 (2008).

[73] P. Molaro, "Science with a 16m VLT: the case for variability of fundamental constants", arXiv:0712.4390 (2007).

[74] http://exoplanet.eu/

[75] D. Charbonneau, *et al.*, "Detection of planetary transits across a sun-like star", *Astrophysical Journal* **529**, L45, (2000).

[76] I. A. Bond, *et al.*, "OGLE 2003-BLG-235/MOA 2003-BLG-53: A planetary microlensing event", *Astrophysical Journal* **606**, L155 (2004).

[77] S. Weinberg, "Gravitation and Cosmology", Wiley, New York (1972).

[78] G. C. McVittie, "Appendix to The Change of Redshift and Apparent Luminosity of Galaxies due to the Deceleration of Selected Expanding Universes", *Astrophysical Journal* **136**, 334 (1962).

[79] A. Friedman, "Über die Krümmung des Raumes", *Zeitschrift für Physik* **10**, 377 (1922).

[80] M. S. Turner, "Dark Energy: Just What Theorists Ordered", *Physics Today* **4**, 10 (2003).

[81] A. Loeb, "Direct Measurement of Cosmological Parameters from the Cosmic Deceleration of Extragalactic Objects", *Astrophysical Journal* **499**, L111 (1998).

[82] J. Liske, *et al.*, "Cosmic dynamics in the era of Extremely Large Telescopes", *Monthly Notices of the Astronomical Society* **386**, 1192 (2008).

[83] M. Rauch, "The Lyman alpha forest in the spectra of quasistellar objects", *Annual Review of Astronomy and Astrophysics* **36**, 267 (1998).

[84] R. Racine, "Atmospheric and facility seeing on Mauna Kea, Hawaii", *Publications of the Astronomical Society of the Pacific* **101**, 436 (1989).

[85] J. S. Lawrence, "Exceptional astronomical seeing conditions above Dome C in Antarctica", *Nature* **431**, 278 (2004).

[86] J. Baudrand and G.A.H. Walker, "Modal Noise in High-Resolution, Fiber-fed Spectra: A Study and Simple Cure" *Publications of the Astronomical Society of the Pacific*, **113**, 851 (2001).

[87] F. Pepe, M. Mayor, and G. Rupprech, "HARPS: ESO's Coming Planet Searcher", *The Messenger* **110**, 9 (2002).

[88] F. Grupp, "The nature of the fiber noise with the FOCES spectrograph — Nature, modeling and a way to achieve S/N ¿ 400", *Astron. Astrophys.* **412**, 897 (2003).

[89] Pepe, F. *et al.*, "HARPS: a new high-resolution spectrograph for the search of extrasolar planets", in *Proceedings of the SPIE Conference* 4008, 582 (2000).

[90] A. P. Hatzes and W. D. Cochran, in *Proceedings of the ESO Workshop on High-Resolution Spectroscopy with the VLT*, ESO, Garching (1992).

[91] M. T. Murphy, Swinburne University of Technology, Melbourne, Australia.

[92] C. J. Willott *et al.*, "Four Quasars above Redshift 6 Discovered by the Canada-France High-z Quasar Survey", *Astronomical Journal* **134**, 2435 (2007).

[93] A. Baranne *et al.*, "ELODIE: A spectrograph for accurate radial velocity measurements", *Astronomy and Astrophysics Supplement Series* **119**, 373 (1996).

[94] R. P. Butler, *et al.*, "Attaining doppler precision of 3 m/s,", *Publications of the Astronomical Society of the Pacific* **108**, 500 (1996).

[95] A. W. Howard, "The NASA-UC ETA-EARTH program: I. A super-earth orbiting HD79241", *Astrophysical Journal* **696**, 75 (2009).

[96] P. Figueira, F. Pepe, C. Lovis and M. Mayor "Evaluating the stability of atmospheric lines with HARPS" *Astronomy and Astrophysics* **515**, A106 (2010).

[97] F. Wildi, "Calibration of high accuracy radial velocity spectrographs: beyond the Th-Ar lamps", in *Proceedings of the SPIE Conference* 7440, 74400M-1 (2009).

[98] J. Alnis *et al.*, "Stable diode lasers for hydrogen precision spectroscopy", *European Physical Journal — Special Topics* **163**, 89 (2008).

[99] B. A. Palmer and R. Engleman, "Atlas of the thorium spectrum" *Los Alamos National Laboratory Report* **LA-9615**, (1983).

[100] L.-S. Ma, *et al.*, "Optical Frequency Synthesis and Comparison with Uncertainty at the 10^{-19} Level" *Science* **303**, 1843 (2004).

[101] M. Zimmermann, *et al.*, "Optical clockwork with an offset-free difference-frequency comb: accuracy of sum- and difference-frequency generation", *Optics Letters* **29**, 310 (2004).

[102] P. Del'Haye, *et al.*, "Optical frequency comb generation from a monolithic microresonator", *Nature* **450**, 1214 (2007).

[103] J. S. Levy, *et al.*, "CMOS-compatible multiple-wavelength oscillator for on-chip optical interconnects", *Nature Photonics* **4**, 37 (2009).

[104] Th. Udem, R. Holzwarth, and T. W. Hänsch, "Optical frequency metrology", *Nature* **416,** 233 (2002).

[105] M. Kourogi *et al.*, "Wide-span optical frequency comb generator for accurate optical frequency difference measurement", *IEEE Journal Quantum Electronics* **29**, 2693 (1993).

[106] Arismar Cerqueira S. Jr *et al.*, "Highly efficient generation of broadband cascaded four-wave mixing products", *Optics Express* **16**, 2816 (2008).

[107] Brault J. W., "High-Precision Fourier-Transform Spectrometry — The Critical Role of Phase Correction", *Mikrochimica Acta* **3**, 215 (1987).

[108] A. Bartels, D. Heinecke and S. A. Diddams, "10-GHz Self-Referenced Optical Frequency Comb", *Science* **326**, 681 (2009).

[109] I. Hartl, *et al.*, "Yb-femtosecond-fiber laser frequency comb", in *Conference on Lasers and Electro-Optics*, 582 (2009).

[110] D. Chao, *et al.*, "Octave-Spanning Supercontinuum Generation for an Er-doped Fiber Laser Frequency Comb at a 1 GHz Repetition Rate", in *Conference on Lasers and Electro-Optics*, CMN6 (2010).

[111] T. Wilken, et. al, "High Repetition Rate, Tunable Femtosecond Yb-Fiber Laser", in *Conference on Lasers and Electro-Optics*, CFK2 (2010).

[112] M. Born and E. Wolf, "Principles of Optics", Cambridge University Press, Cambridge (1999).

[113] A. Bartels, "Gigahertz Femtosecond Lasers" in *Femtosecond Optical Frequency Comb: Principle, Operation, and Applications*, J. Ye, S. T. Cundiff (ed.), Springer (2004).

[114] E. Snitzer, "Proposed Fiber Cavities for Optical Masers", *Journal of Applied Physics* **32**, 36 (1961).

[115] M. J. F. Digonnet (ed.), "Rare-Earth-Doped Fiber Lasers and Amplifiers", Marcell Dekker, Inc., New York (2001).

[116] F. Tauser, A. Leitenstorfer, and W. Zinth, "Amplified femtosecond pulses from an Er:fiber system: Nonlinear pulse shortening and selfreferencing detection of the carrier-envelope phase evolution" *Optics Express* **11**, 594 (2003).

[117] B. R. Washburn, *et al.*, "Phase-locked, erbium-fiber-laser-based frequency comb in the near infrared", *Optics Letters* **29**, 250 (2004).

[118] J. C. Diels, W. Rudolph, "Ultrashort Laser Pulse Phenomena", Academic Press, Burlington (2006).

[119] G. P. Agrawal, "Nonlinear Fiber Optics", Academic Press, San Diego (2001).

[120] B. E. A. Saleh and M. C. Teich, "Fundamentals of Photonics", Wiley, Hoboken (2007).

[121] U. Morgner, *et al.*, "Sub-two-cycle pulses from a Kerr-lens mode-locked Ti:sapphire laser", *Optics Letters* **24**, 411 (1999).

[122] M. Hofer, *et al.*, "Mode locking with cross-phase and self-phase modulation", *Optics Letters* **16**, 502 (1991).

[123] X. Zhou, *et al.*, "Generation of 28-fs pulses from a mode-locked ytterbium fiber oscillator", *Optics Express* **16**, 7055 (2008).

[124] M. E. Fermann, *et al.*, "Nonlinear amplifying loop mirror", *Optics Letters* **15**, 752 (1990).

[125] M. Nakazawa, E. Yoshida, and Y. Kimura, "Low threshold, 290 fs erbium-doped fiber laser with a nonlinear amplifying loop mirror pumped by InGaAsP laser diodes", *Applied Physics Letters* **59**, 2073 (1991).

[126] available from http://www.schott.com

[127] E. B. Treacy, "Optical Pulse Compression with Diffraction Gratings", *IEEE Journal of Quantum Electronics* **5**, 454 (1969).

[128] R. L. Fork, 0. E. Martinez, and J. P. Gordon, "Negative dispersion using pairs of prisms", *Optics Letters* **9**, 150 (1984).

[129] S. Kane, *et al.*, "Hybrid grating-prism stretcher-compressor system with cubic phase and wavelength tunability and decreased alignment sensitivity", *Optics Letters* **19**, 201 (1994).

[130] Robert Szipöcs, *et al.*, "Chirped multilayer coatings for broadband dispersion control in femtosecond lasers", *Optics Letters* **19**, 201 (1994).

[131] T. A. Birks, *et al.*, "Dispersion compensation using single-material fibers", *IEEE Photonics Technology Letters* **11**, 674 (1999).

[132] C. D. Poole, *et al.*, "Broadband dispersion compensation by using the higher-order spatial mode in a two-mode fiber", *Optics Letters* **17**, 985 (1992).

[133] F. Ouellette, "Dispersion Cancellation Using Linearly Chirped Bragg Grating Filters in Optical Waveguides" *Optics Letters* **12**, 847 (1987).

[134] Siegman, "Lasers", University Science Books, Sausalito (1986).

[135] C.-J. Chen, P. K. A. Wai, and C. R. Menyuk, "Soliton fiber ring laser", *Optics Letters* **17**, 417 (1992).

[136] S. M. J. Kelly, "Characteristic sideband instability of periodically amplified average soliton", *Electronics Letters* **28**, 806 (1992).

[137] K. Tamura, E. P. Ippen and H. A. Haus, "Pulse dynamics in stretched-pulse fiber lasers", *Astrophysical Journal* **67**, 158 (1995).

[138] A. Chong, W. H. Renninger and F. W. Wise, "Properties of normal-dispersion femtosecond fiber lasers", *Journal of the Optical Society of America B* **25**, 140 (2008).

[139] F. Ö. Ilday *et al.*, "Self-similar evolution of parabolic pulses in a laser", *Physical Review Letters* **92**, 213902 (2004).

[140] T. Wilken et. al, "Low Phase Noise 250 MHz Repetition Rate Fiber fs Laser for Frequency Comb Applications", in *Conference on Lasers and Electro-Optics*, CMR3, (2007).

[141] A. Chong, *et al.*, "All-normal-dispersion femtosecond fiber laser", *Optics Express* **14**, 10095 (2006).

[142] M. Schultz, *et al.*, "Ytterbium femtosecond fiber laser without dispersion compensation tunable from 1015 nm to 1050 nm", *Optics Communications* **282**, 2567 (2009).

[143] P. Rußbüldt, *et al.*, "400 W Yb:YAG Innoslab fs-amplifier", *Optics Express* 17, 12230 (2009).

[144] H. R. Telle, B. Lipphardt, and J. Stenger, "Kerr-lens, mode-locked lasers as transfer oscillators for optical frequency measurements", *Applied Physics B* **74**, 1 (2002).

[145] L. Hollberg, *et al.*, "Optical Frequency Standards and Measurements," *IEEE Journal of Quantum Electronics* **37**, 1502 (2001).

[146] H. R. Telle. "Frequency Control of Semiconductor Lasers", in *Microwave and Optical Engineering*, chapter 5, 137172. Wiley & Sons, Inc. (1996).

[147] R. Ell, *et al.*, "Generation of 5-fs pulses and octave-spanning spectra directly from a Ti:sapphire laser", *Optics Letters* **26**, 373 (2001).

[148] N. R. Newbury and B. R. Washburn, "Theory of the Frequency Comb Output from a Femtosecond Fiber Laser", *IEEE Journal of Quantum Electronics* **41**, 1388 (2005).

[149] A. Apolonski, *et al.*, "Controlling the Phase Evolution of Few-Cycle Light Pulses", *Physical Review Letters* **85**, 740 (2000).

[150] M. Prevedelli, T. Freegarde, and T. W. Hänsch, "Phase locking of grating-tuned diode lasers", *Applied Physics B* 60, S241 (1995).

[151] O. Mücke, private communication.

[152] H. Hundertmark *et al.*, "Octave-spanning supercontinuum generated in SF6-glass PCF by a 1060 nm mode-locked fibre laser delivering 20 pJ per pulse", *Optics Express* **17** , 1919 (2009).

[153] T. Steinmetz, *et al.*, "Fabry-Pérot filter cavities for wide-spaced frequency combs with large spectral bandwidth." *Appl. Phys. B* **96**, 251 (2009).

[154] available from http://www.newport.com

[155] D. A. Braje, *et al.*, "Astronomical spectrograph calibration with broad-spectrum frequency combs." *Eur. Phys. J. D* **48**, 57 (2008).

[156] T. W. Hänsch and B. Couillaud, "Laser frequency stabilization by polarization spectroscopy of a reflecting reference cavity", *Optics Communications* **35**, 441(1980).

[157] D. A. Shaddock, M. B. Gray, and D. E. McClelland, "Frequency locking a laser to an optical cavity by use of spatial mode interference", *Opt. Lett.* **24**, 1499 (1999).

[158] R. W. P. Drever, *et al.*, "Laser phase and frequency stabilization using an optical resonator", *Applied Physics B* **31**, 97 (1983).

[159] Th. Udem, *et al.*, "Absolute Optical Frequency Measurement of the Cesium D_1 Line with a Mode-Locked Laser", *Physical Review Letters* **82**, 3568 (1999).

[160] J. Chen *et al.*, "Generation of low-timing-jitter femtosecond pulse trains with 2 GHz repetition rate via external repetition rate multiplication", *Optics Letters* **33**, 959 (2008).

[161] L. Fu, *et al.*, "Efficient supercontinuum generations in silica suspended core fibers", *Optics Express* **16**, 19629 (2008).

[162] R. W. Boyd, "Nonlinear Optics", Academic Press, San Diego (2003).

[163] G. Chang, *et al.*, "Toward a broadband astro-comb: effects of nonlinear spectral broadening in optical fibers", *Optics Express* **18**, 12736 (2010).

[164] J. Hansryd, *et al.*, "Fiber-Based Optical Parametric Amplifiers and Their Applications", *IEEE Journal of Selected Topics in Quantum Electronics* **8**, 506 (2002).

[165] M. S. Kang, *et al.*, "Tightly trapped acoustic phonons in photonic crystal fibres as highly nonlinear artificial Raman oscillators", *Nature Photonics* **5**, 276 (2009).

[166] Mayor, M. *et al.* Setting New Standards with HARPS. *The Messenger* **114,** 20 (2003).

[167] S. Kane and J. Squier, "Grism-pair stretchercompressor system for simultaneous second- and third-order dispersion compensation in chirped-pulse amplification", *Journal of the Optical Society of America B* **14**, 661 (1997).

[168] K. Horne, "An optimal extraction algorithm for CCD spectroscopy", *Publications of the Astronomical Society of the Pacific* **98**, 609 (1986).

[169] P. Connes, "Absolute astronomical accelerometry", *Astrophysics and Space Science* **110**, 211 (1985).

[170] M. Casse and F. Vieira, "Comparison of the scrambling properties of bare optical fibers with microlens coupled fibers", in *Proceedings of the SPIE conference* 2871, 1187 (1997).

[171] F. Bouchy, F. Pepe, and D. Queloz, "Fundamental photon noise limit to radial velocity measurements" *Astronomy and Astrophysics* **374**, 377 (2001).

[172] R. Engleman Jr., K. H. Hinkle and L. Wallace, "The near-infrared spectrum of a Th/Ar hollow cathode lamp", *Journal of Quantitative Spectroscopy & Radiative Transfer* **78**, 1 (2003).

[173] S. A. Diddams, *et al.*, "Molecular fingerprinting with the resolved modes of a femtosecond laser frequency comb", *Nature* **445**, 627 (2007).

[174] N. G. Usechak, *et al.*, "Tunable, high-repetition-rate, harmonically mode-locked ytterbium fiber laser", *Optics Letters* **29**, 1360 (2004).

[175] D. Kopon, *et al.*, "Enabling Technologies for Visible Adaptive Optics: The Magellan Adaptive Secondary VisAO Camera", in *Proceedings of the SPIE conference* 7439, 74390Y (2009).

[176] L. W. Ramsey, *et al.*, "A Pathfinder Instrument for Precision Radial Velocities in the Near-Infrared", *Publications of the Astronomical Society of the Pacific* **120**, 887 (2008).

[177] F. Quinlan, *et al.*, "A 12.5 GHz-spaced optical frequency comb spanning > 400 nm for near-infrared astronomical spectrograph calibration", *Review of Scientific Instruments* **81**, 063105 (2010).

[178] C. H. Li, *et al.*, "A laser frequency comb that enables radial velocity measurements with a precision of 1 cm s^{-1}", *Nature* **452**, 610 (2008).

Coauthored Publications

High-precision calibration of spectrographs using laser frequency combs
T. Wilken, C. Lovis, A. Manescau, T. Steinmetz, L. Pasquini, G. Lo Curto, T. W. Hänsch, R. Holzwarth, and Th. Udem,
in *Proceedings of the SPIE conference* **7735**, 77350T (2010).

High-precision calibration of spectrographs
T. Wilken, C. Lovis, A. Manescau, T. Steinmetz, L. Pasquini, G. Lo Curto, T. W. Hänsch, R. Holzwarth, and Th. Udem,
Monthly Notices of the Royal Astronomical Society: Letters **405**, L16 - L20 (2010).

Testing the Stability of the Fine Structure Constant in the Laboratory
N. Kolachevsky, A. Matveev, J. Alnis, C. G. Parthey, T. Steinmetz, T. Wilken, R. Holzwarth, T. Udem and T. W. Hänsch,
Space Science Reviews **148**, 267 – 288 (2009).

Fabry-Perot filter cavities for wide-spaced frequency combs with large spectral bandwidth
T. Steinmetz, T. Wilken, C. Araujo-Hauck, R. Holzwarth, T. W. Hänsch and Th. Udem,
Applied Physics B, **96**, 251 – 256 (2009).

Precision spectroscopy of the 3s-3p fine-structure doublet in Mg$^+$
V. Batteiger, S. Knünz, M. Herrmann, G. Saathoff, H. A. Schüssler, B. Bernhardt, T. Wilken, R. Holzwarth, T. W. Hänsch, and Th. Udem,
Physical Review A **80**, 022503 (2009).

Octave-spanning supercontinuum generated in SF6-glass PCF by a 1060 nm mode-locked fibre laser delivering 20 pJ per pulse
H. Hundertmark, S. Rammler, T. Wilken, R. Holzwarth, T. W. Hänsch, and P. S. Russell,
Optics Express **17**, 1919 – 1924 (2009).

Stable diode lasers for hydrogen precision spectroscopy
J. Alnis, A. Matveev, N. Kolachevsky, T. Wilken, R. Holzwarth, and T. W. Hänsch,
European Physical Journal — Special Topics **163**, 89 – 94 (2008).

Laser frequency combs for astronomical observations
T. Steinmetz, T. Wilken, C. Araujo-Hauck, R. Holzwarth, T. W. Hänsch, L. Pasquini, A. Manescau, S. D'Odorico, M. T. Murphy, T. Kentischer, W. Schmidt, and Th. Udem,
Science **321**, 1335 – 1337 (2008).

Generation of low-timing-jitter femtosecond pulse trains with 2 GHz repetition rate via external repetition rate multiplication
J. Chen, J. W. Sickler, P. Fendel, E. P. Ippen, F. X. Kärtner, T. Wilken, R. Holzwarth, and T. W. Hänsch,
Optics Letters **33**, 959 – 961 (2008).

Optical frequency comb generation from a monolithic microresonator
P. Del'Haye, A. Schliesser, O. Arcizet, T. Wilken, R. Holzwarth, and T. J. Kippenberg,
Nature **450**, 1214 – 1217 (2007).

Conference Contributions

High Repetition Rate, Tunable Femtosecond Yb-Fiber Laser
T. Wilken, P. Vilar-Welter, T. W. Hänsch, Th. Udem, T. Steinmetz, and R. Holzwarth,
in Conference on Lasers and Electro-Optics, paper CFK2, (Optical Society of America, 2010).

High Precision Calibration of Spectrographs in Astronomy
T. Wilken, T. W. Hänsch, T. Udem, T. Steinmetz, R. Holzwarth, A. Manescau, G. Lo Curto, L. Pasquini, and C. Lovis,
in Conference on Lasers and Electro-Optics, paper CMHH3, (Optical Society of America, 2010).

Frequency Combs for Astronomy
T. Wilken, T. W. Hänsch, T. Udem, T. Steinmetz, R. Holzwarth, C. Araujo-Hauck, L. Pasquini, S. D'Odorico, A. Manescau, M. T. Murphy, T. Kentischer, and W. Schmidt,
in Conference on Lasers and Electro-Optics, paper CPDB9, (Optical Society of America, 2008).

Low Phase Noise 250 MHz Repetition Rate Fiber fs Laser for Frequency Comb Applications
T. Wilken, T. W. Hänsch, R. Holzwarth, P. Adel, and M. Mei,
in Conference on Lasers and Electro-Optics, paper CMR3, (Optical Society of America, 2007).

Danksagung

Abschließend möchte ich mich bei allen bedanken, deren Unterstützung ich in den letzen Jahren erhalten habe und die dadurch zum Gelingen dieser Arbeit beigetragen haben.

Ich danke Prof. Theodor W. Hänsch dafür, dass er mich in seine Arbeitsgruppe aufgenommen hat und ich unter seiner Leitung für meine Dissertation am MPQ arbeiten konnte. Die Arbeit an diesem höchst spannenden und abwechslungsreichen Thema hat mir viel Spaß gemacht und die erstklassige Ausstattung sowie die gute Atmosphäre der Arbeitsgruppe haben meinen Erfolg erst ermöglicht.

Großer Dank gebührt auch Thomas Udem und Ronald Holzwarth, die sich immer Zeit für mein Projekt genommen und geduldig alle meine Fragen beantwortet haben. Die vielen gemeinsamen Ausflüge in die Bergwelt, sei es zu Fuß, am Seil, auf dem Sattel oder auf Skiern haben stark zu dem guten Teamgeist in der Gruppe beigetragen.

Insbesondere möchte ich mich aber bei denen bedanken, die in den vergangenen Jahren Frust und Freude immer am direktesten erfahren haben, nämlich Tilo Steinmetz, Katharina Predehl und Valentin Batteiger. Es war eine sehr schöne Zeit zusammen am Teleskop, im Labor und im Büro und ich denke gerne an unzählige gemeinsam durchlittene Momente sowie natürlich besonders Erfolgsmomente zurück.

Allgemein danke ich allen Mitgliedern der Arbeitsgruppe Laserspektroskopie am MPQ für die offene, freundschaftliche Atmosphäre die sich nicht nur auf das Institutsleben beschränkt. Die vielen Ausflüge in die Berge oder auch nur den nächsten Biergarten oder zum Lake Garching schafften immer wieder Abwechslung und gaben Motivation.

Ein großes Dankeschön geht an unsere Techniker Wolfgang Simon und Charly Linner sowie unseren Elektroniker Helmut Brückner. Wann immer etwas zu fräsen, drehen oder zu bohren war und bei jedem Problem mit Lockboxen, Interlock-Schaltungen etc., war schnelle Hilfe garantiert.

Auch außerhalb vom MPQ haben viele zum Erfolg meiner Arbeit beigetragen. Ich danke allen bei Menlosystems, insbesondere Michael Mei, Marc Fischer, Peter Adel, Martin Engelbrecht und Andy Thaller für ihre Unterstützung. Kompetente Hilfe zum Thema Frequenzkamm, Steuerelektronik und Faserlaser war hier immer zu finden. Auch möchte ich mich bei „den drei von der ESO", Luca Pasquini, Gaspare Lo Curto und Antonio Manescau, bedanken. Durch sie habe ich viel

über Astronomie gelernt und eine Faszination wiedergefunden, die während des Studiums eingeschlafen war. Die Aufenthalte an den Teleskopen waren dabei der krönende Höhepunkt. Schließlich danke ich auch Phillip St. J. Russel, Holger Hundermark und Sebastian Stark vom MPL, die uns buchstäblich in letzter Minute eine maßgeschneiderte PCF zur Verfügung gestellt haben, die den Durchbruch bei der Erzeugung des breiten Spektrums brachte.

Nicht vergessen seien auch alle Freunde aus meinem Leben vor der Doktorarbeit. Es ist schön zu wissen, dass man sich immer auf euch verlassen kann und auch große Entfernungen und seltene Treffen daran nichts ändern.

Mein besonderer Dank gilt aber meiner Familie. Ich danke meinen Eltern, die mich Zeit meines Lebens immer unterstützt und gefördert haben. Und natürlich gilt mein größter Dank meiner Frau Magdalena die stets Geduld und Verständnis hatte und mir mit Carina das schönste Geschenk bereitet hat.